CHEMICAL REVIEWS

pubs.acs.org/CR

Review

Electromagnetic Forces and Torques: From Dielectrophoresis to Optical Tweezers

Marco Riccardi and Olivier J. F. Martin*

Cite This: *Chem. Rev.* 2023, 123, 1680−1711

Read Online

ACCESS | Metrics & More | Article Recommendations

ABSTRACT: Electromagnetic forces and torques enable many key technologies, including optical tweezers or dielectrophoresis. Interestingly, both techniques rely on the same physical process: the interaction of an oscillating electric field with a particle of matter. This work provides a unified framework to understand this interaction both when considering fields oscillating at low frequencies—dielectrophoresis—and high frequencies—optical tweezers. We draw useful parallels between these two techniques, discuss the different and often unstated assumptions they are based upon, and illustrate key applications in the fields of physical and analytical chemistry, biosensing, and colloidal science.

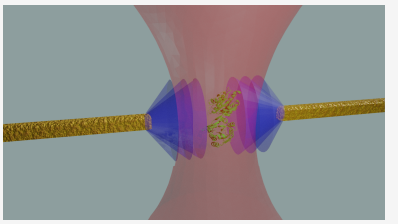

CONTENTS

1. INTRODUCTION

When an electric or magnetic field interacts with matter, be it a cell, biomolecule, or inorganic particle, it modifies the electric charges' distribution within, for example, by moving the electrons around or reorienting the molecule/particle. The collective motion of these microscopic charges or molecules has the net effect of generating a macroscopic force on the object, which can therefore effectively be manipulated using electromagnetic fields. For instance, proteins can interact with electrostatic fields to generate forces that are used to separate and distinguish biomolecules of different sizes within the same biological sample.[1,2] Similarly, the nebulous envelope of a comet is pushed away as it interacts with solar radiation, in a process that leads to the formation of comet tails.[3] These two simple examples already show what is arguably the greatest asset of electromagnetic forces: their ability to manipulate bodies of different kinds across a very broad length scale that ranges from a few ångström to a few hundred microns. Some of the objects that can be controlled with these forces and torques are shown in Figure 1 and include single atoms[4,5] and molecules,[6−8] nucleic acids,[9,10] nano- and microparticles,[11−14] and organelles[15] and cells.[16−18] As a consequence, applications

Received: August 16, 2022
Published: January 31, 2023

https://doi.org/10.1021/acs.chemrev.2c00576
Chem. Rev. 2023, 123, 1680−1711

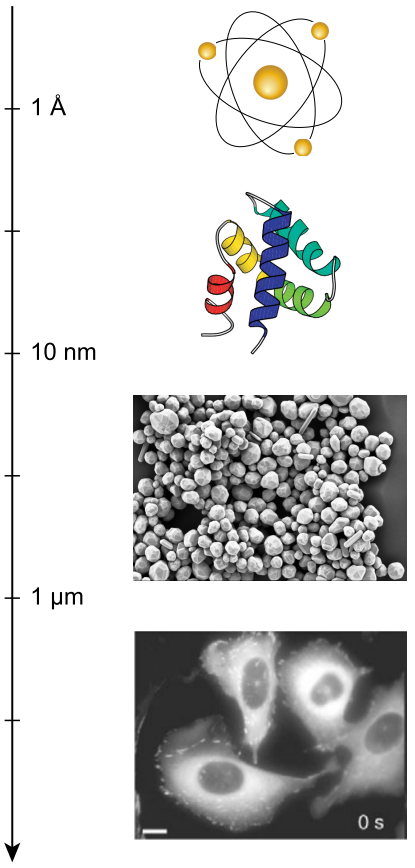

Figure 1. Examples of some of the objects that can be manipulated using electromagnetic forces and torques. From the smallest to the largest: atoms, biomolecules (Reprinted with permission from ref 26. Copyright 2001 American Association for the Advancement of Science), nanomaterials, and cells (Reprinted with permission from ref 27. Copyright 2009 The Company of Biologists).

of interest span the whole micro- and nanotechnology universe and include single-molecules studies,[8,19] biosensing,[20,21] molecular motors[22,23] realization ,and analyte manipulation for lab-on-a-chip and point-of-care applications.[18,24,25]

The understanding and control of electromagnetic interactions is therefore of paramount importance to fuel progresses in their technological applications at the crossroad between chemistry, physics, and biology. This work provides a unified framework to understand the main class of interactions occurring between fields and matter, namely, the dipolar interaction and its role to enable practical applications at the micro- and nanoscales. In particular, it will be clear from our treatment that two of the most used technologies in micro- and nanomanipulations, the optical tweezers and dielectrophoresis, rely on the same physical mechanism, of which we will highlight some important applications in the fields of physical and analytical chemistry, biosensing, and colloidal science. The review is organized as follows: after this first introductory paragraph, Section 1.1 introduces electric fields as the main source of electromagnetic forces and torques and classifies these fields according to their oscillation frequency. Section 1.2 introduces some important notations that will be used throughout the whole paper and illustrates the two principal techniques for electromagnetic forces and torques calculation, namely, the *equivalent multipole* method and the *Maxwell's stress tensor* formalism. The connections between these two methods are highlighted and will guide our treatment in the remainder of the review. Sections 2−3, respectively, provide a complete description of the generation of electromagnetic forces and torques, with emphasis on those interactions that can be described within the dipolar approximation, while higher-order corrections to this approximation are briefly touched upon in Sections 2.2 and 3.2. Sections 2.3 and 3.3 provide an overview of different experimental setups that have been used in the literature to generate electromagnetic forces and torques, while Section 4 presents the main applications of these forces for analyte manipulation, with a particular emphasis on their ability to trap, assemble, and transport micro- and nanosystems.

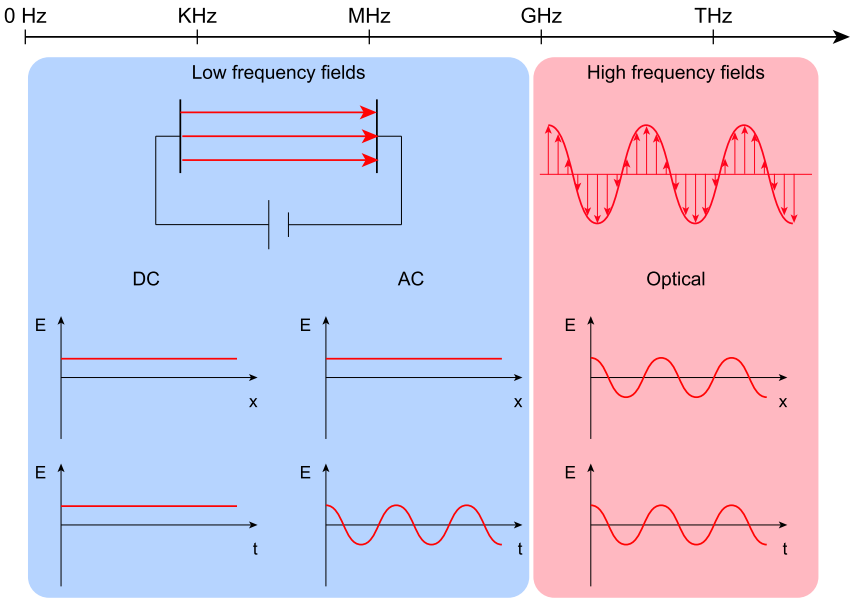

Figure 2. Comparison between low- and high-frequency fields.

https://doi.org/10.1021/acs.chemrev.2c00576
Chem. Rev. 2023, 123, 1680−1711

1.1. Electric Fields

We will consider, here, electric fields oscillating at a specific frequency ν that can take any value between 0 and a few hundred THz. This frequency is an important parameter that determines how the field couples with matter and notably dictates the main loss mechanism in the interaction. Generally, conductive losses dominate at frequencies below a few MHz, while dielectric losses stemming from absorption and relaxation processes become more important at higher frequencies.[28] Depending on the value of ν, we will broadly divide the fields in two different categories, low-frequency and high-frequency fields, as shown in Figure 2 where we indicate the former with a blue color and the latter with a pink one. The first are generated by batteries or function generators and are always confined between two electrodes, i.e., they do not indefinitely propagate in space. They are usually employed at radio frequencies (RF) ranging from 0 (DC) to a few tens of MHz and sometimes GHz (AC). In the high-frequency regime, the fields considered are part of self-sustained electromagnetic excitations, also comprising magnetic fields oscillating in phase with their electric counterpart, and have a more complex spatiotemporal distribution, as shown in Figure 2. We will mainly discuss monochromatic radiations in the visible/near-infrared part of the spectrum, i.e., oscillating at $\sim 10^2$ THz, and we will therefore call this the optical regime.

The MKSA units system is used throughout, and the response of a material to an applied field is described with the dielectric permittivity ϵ and the magnetic permeability μ. As a consequence, Maxwell's equations take the following form:

$$\nabla \cdot \mathbf{D} = \rho \tag{1}$$

$$\nabla \cdot \mathbf{B} = 0 \tag{2}$$

$$\nabla \times \mathbf{E} = -\frac{\partial \mathbf{B}}{\partial t} \tag{3}$$

$$\nabla \times \mathbf{H} = \mathbf{j} + \frac{\partial \mathbf{D}}{\partial t} \tag{4}$$

where $\mathbf{E}$ denotes the electric field, $\mathbf{D} = \epsilon\mathbf{E}$ is the electric displacement, $\mathbf{H}$ is the magnetic field, and $\mathbf{B} = \mu\mathbf{H}$ is the magnetic induction; ρ and $\mathbf{j}$ are, respectively, the volume charge and surface current densities. We will consider nonmagnetic isotropic materials for which $\mu = \mu_0$ (vacuum permeability), and therefore $\mathbf{B} = \mu_0\mathbf{H}$. Here and throughout the text, bold quantities represent vectors.

1.2. Electromagnetic Forces and Torques Calculation

The generation of electromagnetic forces and torques on a particle is a complex physical process resulting from field–matter interactions between the particle and the fields. Several methods have been developed to accurately describe these forces and torques, the two most important being the *equivalent multipole* approach and the *Maxwell's stress tensor* formalism. Each of these two methods provides a simplified description of either the field or the particle and, thus. significantly reduces the complexity of the problem and allows one to gain some valuable physical insights into the system and to quantitatively study it. In the equivalent multipole method, developed by Jones and Washizu,[29,30] the particle is treated as a collection of multipoles (i.e., charges) of increasing orders (i.e., with an increasing number of charges), and the force acting on each multipole is computed separately. An approximate value of the total force acting on the particle is then simply found by adding together the individual force contributions from each multipole, with the underlying idea being that if the number of multipoles considered is large enough, the calculation converges to the real value of the force. Unfortunately, as more multipoles are taken into account, the complexity of the computation increases so that only the first few multipoles, shown in Figure 3, are usually considered ([1]).

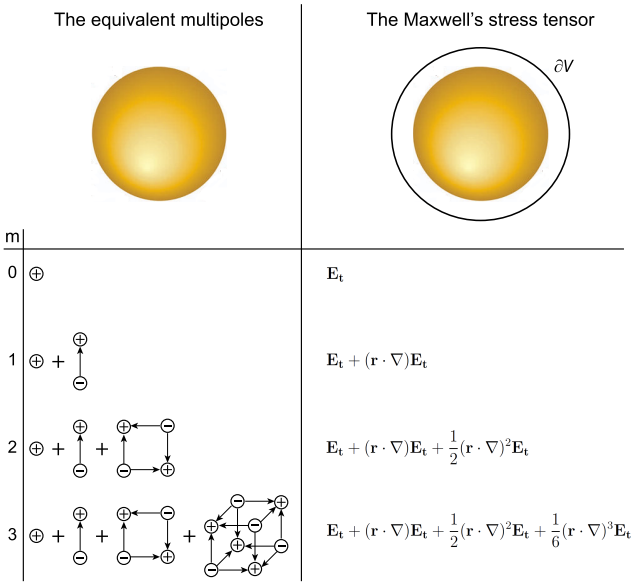

Figure 3. Comparison between the equivalent multipole method and the Maxwell's stress tensor approach. The different multipoles are indexed by their order n in such a way that the first order multipole is the dipole, the second order multipole is the quadrupole, followed by the octupole, and so on. Similarly, the first three field derivatives (calculated in $\mathbf{r}_0 = 0$) are $\nabla\mathbf{E}_t$, $\nabla^2\mathbf{E}_t = \nabla\nabla\mathbf{E}_t$, and $\nabla^3\mathbf{E}_t = \nabla\nabla\nabla\mathbf{E}_t$. Only the first three electrical multipoles and electric field derivatives are shown, but the comparison is easily extended to higher orders and to magnetic fields.

Nonetheless, these first multipoles are usually enough to provide a good description of the system because they collectively induce the same response produced by the particle. In this way, study of the collection of multipoles becomes *equivalent* to studying the full particle. Let us now consider an isotropic spherical particle of radius r described by a frequency-dependent complex permittivity $\epsilon_p(\omega) = \epsilon_p'(\omega) + i\epsilon_p''(\omega)$ immersed in a medium with permittivity $\epsilon_m(\omega) = \epsilon_m'(\omega) + i\epsilon_m''(\omega)$ under a harmonic excitation ([2]) $\mathbf{E}(\mathbf{r}, \omega) = \Re[\mathbf{E}(\mathbf{r})e^{-i\omega t}] = \Re[\mathbf{E_0}(\mathbf{r})e^{i\phi(\mathbf{r})}e^{-i\omega t}]$, where the angular frequency ω is defined as $\omega = 2\pi\nu$. The vector $\mathbf{E_0}$ represents the complex field amplitude, and ϕ is its phase ([3]). Here and throughout the rest of this work, we focus our attention mainly on the electric field, as it is more intense than its magnetic counterpart and interacts more strongly with matter, but similar results can also be derived by considering magnetic fields.[31,32] The n^{th} order electric multipole $\underset{\cdot\cdot n}{\mathbf{p}}$ induced in the spherical particle by the electric field is an n^{th} order dyadic tensor that can be expressed as[30]

$$\underset{\cdot\cdot n}{\mathbf{p}}(\mathbf{r}, \omega) = \alpha^{(n)}(\omega)\nabla^{n-1}\mathbf{E}(\mathbf{r}, \omega) \tag{5}$$

with

https://doi.org/10.1021/acs.chemrev.2c00576
Chem. Rev. 2023, 123, 1680−1711

$$\alpha^{(n)}(\omega) = \frac{4\pi\epsilon_m' r^{2n+1} n}{(2n-1)!!} K^{(n)}(\omega) \tag{6}$$

being the hyperpolarizability of the particle ([4]) and

$$K^{(n)}(\omega) = \frac{\epsilon_p - \epsilon_m}{n\epsilon_p + (n+1)\epsilon_m} \tag{7}$$

The term $\underset{\cdot\cdot n}{\mathbf{p}}$ can be thought of as a quantity expressing the material substance of the system. Through combination of it with suitable expressions for the field, the total field−matter interaction is then considered, and the resulting force and torque acting on the particle can be calculated. We point out, here, that eq 6 is exact only for static fields. It still yields correct results for low-frequency fields, but radiative corrections need to be included in the expression of $\alpha^{(n)}$ when considering high-frequency fields, such as optical fields. For $n = 1$, these corrections are included as[34]

$$\alpha^{(1)} = \frac{\alpha_0}{1 - \frac{ik^3\alpha_0}{6\pi\epsilon_m'}} \tag{8}$$

with α_0 being the DC polarizability defined in eq 6 for $n = 1$.

A different approach is taken when using the Maxwell's stress tensor method, which, rather than providing a simplified description of the particle, is instead concerned with the fields surrounding it. With this approach, the total electric and magnetic fields $\mathbf{E_t}$ and $\mathbf{H_t}$ that result from the sum of the incoming and scattered fields (the latter takes into account the perturbation induced by the particle), are first numerically computed on a surface ∂V surrounding the particle and then combined to generate Maxwell's stress tensor $\underline{\underline{\mathbf{T}}}$[35,36]

$$\underline{\underline{\mathbf{T}}} = \epsilon_m' \mathbf{E_t}\mathbf{E_t} + \mu_0 \mathbf{H_t}\mathbf{H_t} - \frac{1}{2}(\epsilon_m' |\mathbf{E_t}|^2 + \mu_0 |\mathbf{H_t}|^2)\underline{\underline{\mathbf{I}}} \tag{9}$$

which is then integrated over ∂V, as shown in Figure 3, to yield the desired force or torque (see eqs 11 and eq 37). Here and throughout the text, double-underlined quantities represent second rank tensors (matrices), and therefore $\underline{\underline{\mathbf{I}}}$ is the unit tensor. Similarly to what is done in the multipole method, it is possible to calculate an approximate value of the force by expanding the fields as a Taylor series about the center of the particle ([5])

$$\mathbf{E_t}(\mathbf{r}) = \sum_{n=0}^{\infty} \frac{1}{n!}(\mathbf{r}\cdot\nabla)^n \mathbf{E_t}(\mathbf{r}) = \mathbf{E_t}(0) + (\mathbf{r}\cdot\nabla)\mathbf{E_t}(0) + \ldots \tag{10}$$

and, in the expression for $\underline{\underline{\mathbf{T}}}$, consider only the first n terms. Again, the more terms (i.e., the more field derivatives) that are considered, the more accurate but complex the calculation becomes, and the number of terms required to provide an adequate description of the force is generally determined by the extent of the field nonuniformity. The advantage of Maxwell's stress tensor method over the equivalent multipoles technique is that, when the full expression of the fields is employed, this method allows the calculation of the *exact* force and torque acting on the particle (and indeed, this is how Maxwell's stress tensor is usually employed), even though the computation can become quite numerically expensive. However, this approach provides no real physical insights on the mechanisms of force generation, which is, conversely, fully captured by the multipole picture. In any case, both methods are equivalent and lead to the same expressions for the force and torque.[35] A connection between the two approaches can be found by noting how the n^{th} multipole is generated by the $(n-1)^{\text{th}}$ derivative of the field (see eq 5) but interacts only with its n^{th} derivative to yield the resulting force, eq 12. As a consequence, if one considers, for example, only the first two terms $\mathbf{E}$ and $\nabla\mathbf{E}$ in the field's expansion ($n = 1$), the field $\mathbf{E}$ will interact with the charges present in the particle (monopoles) to generate an electrical dipole, which in turn will interact with $\nabla\mathbf{E}$ to produce a force or torque. Furthermore, $\nabla\mathbf{E}$ will also induce an electrical quadrupole ($n = 2$) in the particle, which will not contribute to the total force since the $\nabla\nabla\mathbf{E}$ term was not retained.

Let us now separately study the cases of electric-field-generating forces or torques on a particle. Let us first remark that, while the two methods outlined above generally allow the calculation of the instantaneous force and torque, these vary on a time scale equal to the frequency of oscillation of the field. This corresponds to a few μs for RF fields and a few tens of fs for optical fields, which are time scales not usually accessible with standard laboratory equipment. One therefore usually calculates and measures a time-averaged force and torque whose value is the average of these quantities over a full field cycle and is indicated with the < > symbol.

2. FORCES

The time-averaged force exerted on a particle can be expressed as[32]

$$\begin{aligned} <\mathbf{F}> &= <\int_{\partial V} \underline{\underline{\mathbf{T}}}\cdot\mathbf{n}dA> = \int_{\partial V} <\underline{\underline{\mathbf{T_i}}} + \underline{\underline{\mathbf{T_{mix}}}} + \underline{\underline{\mathbf{T_s}}}>\cdot\mathbf{n}dA \\ &= <\mathbf{F_i}> + <\mathbf{F_{mix}}> + <\mathbf{F_s}> \end{aligned} \tag{11}$$

where $\underline{\underline{\mathbf{T}}}$ has been decomposed into a part depending on the incoming field $<\underline{\underline{\mathbf{T_i}}}>$, a part depending on the scattered field $<\underline{\underline{\mathbf{T_s}}}>$, and a part containing mixed field terms $<\underline{\underline{\mathbf{T_{mix}}}}>$. It can be shown that $<\mathbf{F_i}>$, i.e., the part of the force dependent on the incoming field, is equal to 0.[32] Moreover, after neglecting the influence of the magnetic field ([6]), we obtain[30]

$$<\mathbf{F}> = <\mathbf{F_{mix}}> + <\mathbf{F_s}> = \sum_{n=0}^{\infty} \frac{1}{2}\Re\left(\frac{\underset{\cdot\cdot n}{\mathbf{p}}[\cdot]^n \nabla^n \mathbf{E}^*}{n!}\right) + <\mathbf{F_s}> \tag{12}$$

where the * symbol represents the complex conjugate operation. In general, $<\mathbf{F_s}>$, which depends on the scattered field, may also be written as a series, with each term being proportional to the product of two multipole moments, and represents the force arising from the interference between two different multipoles.[32] This contribution begins to play a role only from the second order ($n = 2$) when several different moments are induced in the particle.[37] As for $<\mathbf{F_{mix}}>$, this force is expressed as the dyadic product of a term containing the perturbation induced by the particle ($\underset{\cdot\cdot n}{\mathbf{p}}$) and another one containing the incoming field ($\nabla^n\mathbf{E}^*$). One can readily see that, for $n = 0$, this force corresponds to the Coulomb force $q\mathbf{E}$, with $p = q$ being the 0th order multipole (the monopole) equal to the particle's electrical charge. Because of inertial constraints, this force can be neglected for frequencies higher than 200 Hz and is therefore not relevant for optical fields.[38] However, low-frequency and DC electric fields can be used to manipulate analytes and fluids, for example, using electro-

https://doi.org/10.1021/acs.chemrev.2c00576
Chem. Rev. 2023, 123, 1680−1711

phoresis.[39,40] Unfortunately, the application range of this force is restricted to charged objects, thus limiting its practical interest. Luckily, this restriction can be overcome when considering the next contribution to the force, arising at $n = 1$, on which we will focus in the next section.

2.1. First Order

For $n = 1$, the only multipole induced in the particle is the *dipole*, and hence when considering the forces arising at this order, one works in the dipolar approximation. As mentioned, the induced dipole is generated by the field $\mathbf{E}$, which is assumed to be constant across the particle in order for the $\nabla\mathbf{E}$ term to suffice for an accurate description of the system. Conversely, this means that one can safely use the dipolar approximation and neglect all higher order contributions to the force, albeit only when the particle radius is roughly 6 times smaller than the field wavelength.[41] Provided this condition is met, the force acting on a dipolar particle is then found by truncating the series in eq 12 at $n = 1$, thereby yielding[42]

$$\langle \mathbf{F} \rangle = \frac{1}{2}\Re(\mathbf{p}\cdot\nabla\mathbf{E}^*) = \frac{\alpha'}{4}\nabla|\mathbf{E_0}|^2 + \frac{\alpha''}{2}|\mathbf{E_0}|^2\nabla\phi - \frac{\alpha''}{2}\Im(\mathbf{E_0}\cdot\nabla\mathbf{E_0^*}) \tag{13}$$

where

$$\alpha(\omega) = \alpha' + i\alpha'' = \alpha^{(1)} \tag{14}$$

is the frequency-dependent particle's polarizability as defined in eq 8 with

$$\alpha_0 = 4\pi\epsilon'_m r^3 K(\omega) \tag{15}$$

and

$$K(\omega) = K^{(1)}(\omega) = \frac{\epsilon_p(\omega) - \epsilon_m(\omega)}{\epsilon_p(\omega) + 2\epsilon_m(\omega)} \tag{16}$$

This last equation defines the so-called Clausius−Mossotti factor, while

$$\mathbf{p} = \alpha(\omega)\mathbf{E}(\mathbf{r}, \omega) \tag{17}$$

is the dipole moment of the particle induced by the field $\mathbf{E}$. This induced polarization can be accounted for by considering two contributions: one from free conduction charges and another one from bound electrons (dielectric polarization) ([7]). To see how these two different types of charges contribute to the overall particle polarization, we can rewrite the dielectric function as $\epsilon_{p,m}(\omega) = \epsilon'_{p,m} + i(\epsilon^d_{p,m} + \sigma_{p,m}/\omega) = \epsilon^*_{p,m} + i\sigma_{p,m}/\omega$ and substitute it into eq 16, thereby yielding ([8])[29]

$$K(\omega) = \frac{\sigma_p - \sigma_m}{\sigma_p + 2\sigma_m}\frac{1 - i\omega\tau_0}{1 - i\omega\tau} \tag{18}$$

where

$$\tau_0 = \frac{\epsilon_p^* - \epsilon_m^*}{\sigma_p - \sigma_m} \tag{19}$$

is a time constant and

$$\tau = \frac{\epsilon_p^* + 2\epsilon_m^*}{\sigma_p + 2\sigma_m} \tag{20}$$

is the characteristic charge relaxation time at the particle/medium interface that quantifies the buildup or decay of interfacial charges. In the low-frequency (below ≃100 kHz), or DC, cases,

$$\lim_{\omega\tau\to 0} K = \frac{\sigma_p - \sigma_m}{\sigma_p + 2\sigma_m} = K_0 \tag{21}$$

and the particle response is purely dominated by conductive charges. Conversely, in the high-frequency limit,

$$\lim_{\omega\tau\to\infty} K = \frac{\epsilon_p^* - \epsilon_m^*}{\epsilon_p^* + 2\epsilon_m^*} = K_\infty \tag{22}$$

the response of conduction charges becomes negligible, and the bound electrons (viz. displacement currents) dominate the particles response. The frequency where this displacement current takes over from the conduction current can be estimated as $1/\tau$ and can be any value from 500 kHz to 1 GHz depending on the experimental conditions.[44] Therefore, in the case of optical excitations, dielectric polarization clearly dominates the system response, while low-frequency fields represent a somewhat middle case between these high-frequency and DC limits. It is interesting to also illustrate the transient response of the particle after the field is turned on at $t = 0$. Under these conditions, the Clausius−Mossotti factor takes the form[29,45]

$$K = K_0(1 - e^{-t/\tau}) + K_\infty e^{-t/\tau} \tag{23}$$

This expression clearly shows how polarization charges dominate the transient response to the field, while conduction charges dictate the steady-state properties of the system. We finally point out that, as long as polarization effects at the particle surface can be neglected, the value of K is limited between 1 (for $\epsilon_p \gg \epsilon_m$) and −0.5 (for $\epsilon_m \gg \epsilon_p$), and the polarization is fully described within the framework of the Maxwell−Wagner relaxation theory outlined above in eqs 18−22.

There are, however, cases where surface effects need to be considered to fully describe the polarization response of a particle. For example, when the analyte is not dispersed in a dielectric medium but rather in a highly conductive (>1 mS/m) electrolyte solution, an electric double layer (EDL) of ions forms at the interface between the particle and the liquid. In return, the charging of the EDL can greatly affect the polarizability response of the particle at frequencies smaller than $1/\tau_{EDL}$ (taking usual values in kHz−MHz), where $\tau_{EDL} = 2\epsilon'_m r/\lambda_D\sigma'_m$ is the characteristic time of charge build-up at the interface, and λ_D is the Debye length of the system,[46,47] and its effect needs to be taken into account. Great care is also advised when calculating K for very small bioanalytes, for which dielectric responses are dominated by interfacial phenomena.[48] In particular, proteins possess a strong permanent dipole moment that results in the formation of a highly polarized hydration shell when dispersed into a buffer solution, thus increasing their Clausius−Mossotti factor to values that can sometimes exceed 37 000.[49] Interestingly, all these effects are mostly negligible when working at optical frequencies, whose oscillations occur at shorter time scales than most interfacial phenomena. As a consequence at these frequencies, eq 8 can generally be assumed to properly describe the particle polarization.

For the forces, we see that for fields with a real valued amplitude, such as linearly polarized optical beams, eq 13 reduces to[50−52]

https://doi.org/10.1021/acs.chemrev.2c00576
Chem. Rev. 2023, 123, 1680−1711

$$\langle \mathbf{F} \rangle = \frac{\alpha'}{4} \nabla |\mathbf{E_0}|^2 + \frac{\alpha''}{2} |\mathbf{E_0}|^2 \nabla \phi \tag{24}$$

It is clear from this equation that, depending on the sign of α' and α'', the force can move the particle along $\nabla|\mathbf{E_0}|^2$ and $\nabla\phi$ and is therefore called a *gradient force*. In practice, this means that this force will push/repel the particle toward/from regions of higher electric field intensity or phase. We can further note that the first term of eq 24, proportional to $\nabla|\mathbf{E_0}|^2$, is an intensity gradient conservative force, while the term proportional to α'' is the nonconservative phase gradient force ([9]) (similarly, the last term in eq 13 is the nonconservative polarization force). As such, it is therefore possible and often instructive for the intensity gradient force to plot its potential as $-\alpha'|\mathbf{E_0}|^2/4$, which provides useful insights into how the particle will behave under the action of the field, as illustrated in Figure 4. In Figure 4a, the particle interacts with a Gaussian-shaped intensity field profile (red line). Provided that $\alpha' > 0$, the resulting force will push the particle toward the origin and trap it there at the bottom of the potential well (blue line). Conversely, a linearly increasing intensity profile generates a constant force that pushes the particle toward lower values of the potential, as shown in Figure 4b.

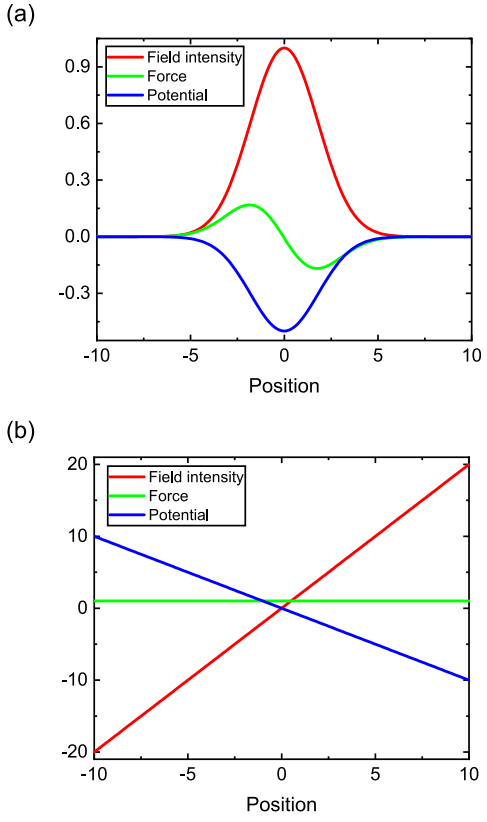

Figure 4. Intensity gradient force in different field distributions. (a) Gaussian field intensity profile producing a potential well. In this case, the particle will fall into the well and find a stable position where the force is equal to 0. (b) Linear field intensity profile. Here, the particle will experience a constant force along the positive direction. **p** has been set to 2 in both cases, and arbitrary units are employed on the x and y axis.

The sign of α' and α'' depends on K, which is, therefore, crucial to determine the direction (and, to a certain extent, the intensity) of the force. This can be intuitively explained by considering the relative phase between the induced polarization in the particle—which is always collinear with K—and the incoming field, as explained in Figure 5. Here, the force

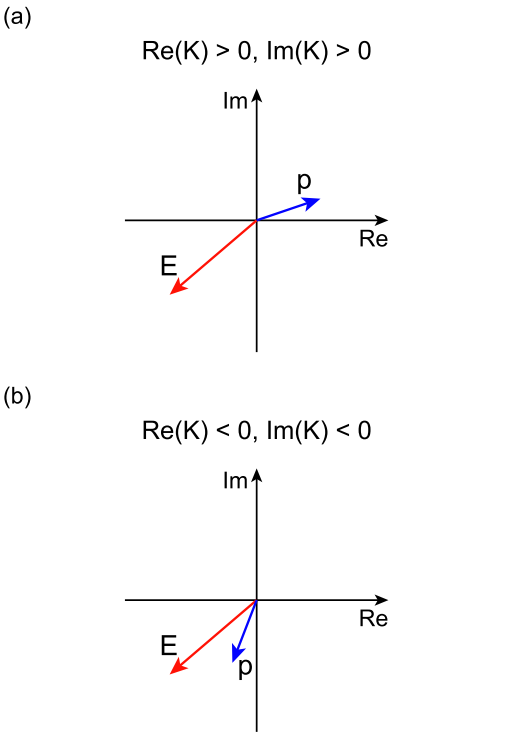

Figure 5. Generation of different intensity and phase gradient forces depending on the position of the polarization phasor in the complex plane. (a) Positive intensity and phase gradient forces for $\Re(K) > 0$ and $\Im(K) > 0$. (b) Negative intensity and phase gradient forces for $\Re(K) < 0$ and $\Im(K) < 0$.

can, depending on the phase shift between these two phasors (i.e., the sign of α' and α''), point toward regions of stronger field and phase (along $\nabla|\mathbf{E_0}|^2$ and $\nabla\phi$, Figure 5a) or toward regions of weaker field and phase (along $-\nabla|\mathbf{E_0}|^2$ and $-\nabla\phi$, Figure 5b). Other combinations are possible for **p** lying in the second or fourth quadrant of the complex plane. We can further infer from Figure 5 that, at the frequency where $\alpha' \simeq 0$ and the intensity gradient force goes to zero, the phase gradient component of the force takes its maximum (or minimum) value. We point out already here that the sign of α' and α'' can be controlled by tuning the frequency of the applied field in such a way that it is fairly straightforward to switch from an attractive to a repulsive force, as will be shown later.

Let us now treat in greater detail the two cases of low- and high-frequency excitations.

2.1.1. Low-Frequency Regime. We now consider fields oscillating at RF frequencies from a few kHz to a few GHz. In this regime, both the conductive and dielectric properties of the particle need to be taken into account to fully determine its response to the applied field. They are described by the particle conductivity

$$\sigma_p = \sigma_{bulk} + \frac{2S}{r} \tag{25}$$

which is the sum of a bulk term σ_{bulk} and a surface term expressed through the surface conductance S. In metals, we

https://doi.org/10.1021/acs.chemrev.2c00576
Chem. Rev. 2023, 123, 1680−1711

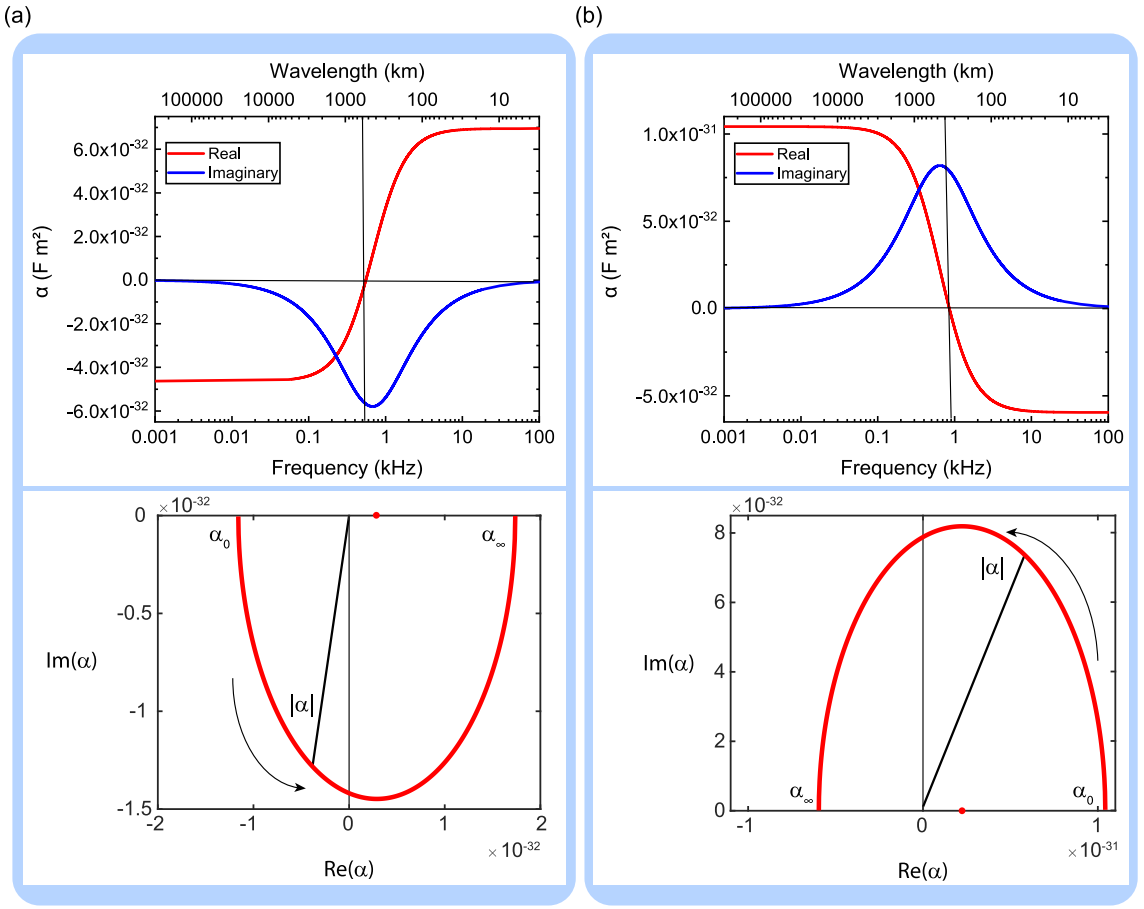

Figure 6. Real and imaginary parts of the polarizability (top) and the corresponding Argand plots (bottom) for a homogeneous sphere with a 100 nm diameter immersed in different media for the cases (a) $\epsilon'_p = 10\epsilon_0$, $\epsilon'_m = 2.5\epsilon_0$ and $\sigma'_p = 10^{-8}$ S/m, $\sigma'_m = 4 \times 10^{-8}$ S/m and (b) $\epsilon'_p = \epsilon_0$, $\epsilon'_m = 10\epsilon_0$ and $\sigma'_p = 10^{-7}$ S/m, $\sigma'_m = 10^{-8}$ S/m. In the Argand plots, the red dot represents the center of the locus of α, and the black line is its magnitude.

generally have $\sigma_{bulk} \gg 2S/r$, and the surface term can be safely neglected.[53] For dielectric objects, however, this term (of typical values 1 nS arising from charged chemical groups on the particle surface and/or counterions in the EDL) can have a significant influence on the overall electrical properties.[54] Furthermore, because of its $1/r$ dependence, this term also becomes dominant for metallic nanoparticles.[44,55] Surface conductance studies are therefore critical for the determination of the dielectric properties of the analyte of interest[54,56−59] and, more specifically, their general dependence on the frequency of the applied field (10). To this end, let us recall that, for a homogeneous dielectric sphere under the action of an RF field, its polarizability (11) can be rewritten as[61]

$$\alpha(\omega) = 4\pi\epsilon'_m r^3 \left[\frac{1}{2}(K_0 + K_\infty) + \frac{1}{2}(K_0 - K_\infty)e^{(2i \arctan \omega\tau)}\right] \tag{26}$$

which shows how, as the frequency is increased, the α phasor moves anticlockwise in the complex plane following a semicircle centered on the real axis in $4\pi\epsilon'_m r^3|(K_0 + K_\infty)/2|$ with radius $4\pi\epsilon'_m r^3|(K_0 - K_\infty)/2|$, as illustrated in Figure 6. This figure shows how at $\omega = 0$, $\alpha = 4\pi\epsilon'_m r^3 K_0 = \alpha_0$ and lies on the real axis. As the frequency increases, α acquires an imaginary component because of ohmic losses, and the phasor moves anticlockwise in the complex plane. At higher frequencies, ohmic losses are negligible, and the polarizability becomes real again, thereby meeting the real axis at $\alpha_\infty = 4\pi\epsilon'_m r^3 K_\infty$ (12). This behavior is depicted in Figure 6a for a particle with higher permittivity and lower conductivity than the surrounding medium, for which $K_\infty > K_0$, and the magnitude of α grows as the frequency increases. This can be understood by recalling that conduction charges dominate the system's response to the field at low frequencies. As a consequence, the condition $\sigma_m > \sigma_p$ implies a more polarized medium and therefore a relatively small $|\alpha|$. At higher frequencies, the larger value of ϵ_p will polarize the particle more than the surrounding medium, thereby leading to a polarizability increase. The opposite happens in Figure 6b, where the particle has a smaller permittivity than the surroundings, while other cases are possible for different ratios of the permittivities and conductivities.

At these low frequencies, the force gives rise to *dielectrophoresis* (DEP) and is usually expressed by inserting eq 15 into eq 24 to yield

$$\langle \mathbf{F_{DEP}} \rangle = 2\pi\epsilon'_m r^3 \left[\Re\left(\frac{\epsilon_p - \epsilon_m}{\epsilon_p + 2\epsilon_m}\right)\nabla |\mathbf{E_{rms}}|^2 + 2\Im\left(\frac{\epsilon_p - \epsilon_m}{\epsilon_p + 2\epsilon_m}\right)|\mathbf{E_{rms}}|^2 \nabla\phi\right] \tag{27}$$

where $|\mathbf{E_{rms}}| = |\mathbf{E_0}|/\sqrt{2}$. We point out that DC electrical fields can also be used for the generation of field gradients, in which case the dielectrophoretic force simply results from eq 27 by

https://doi.org/10.1021/acs.chemrev.2c00576
Chem. Rev. 2023, 123, 1680−1711

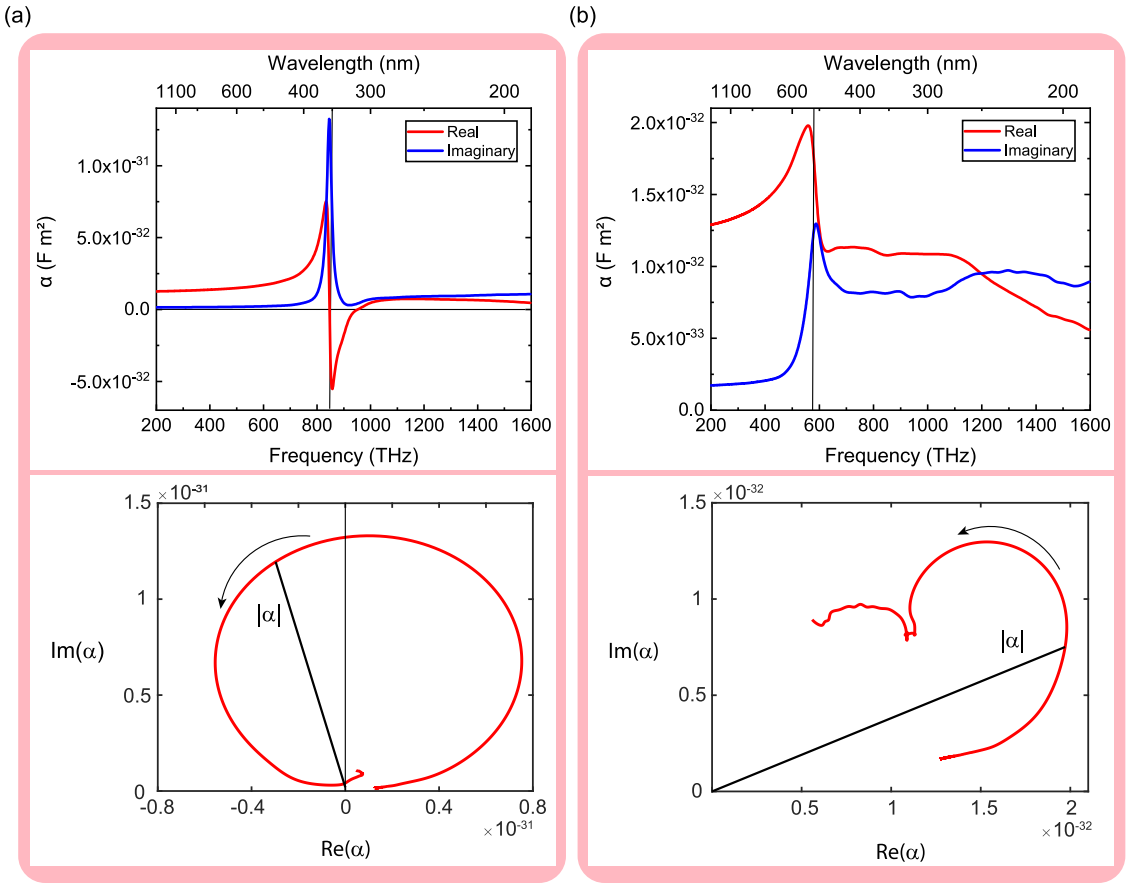

Figure 7. Real and imaginary parts of the polarizability (top) and the relative Argand plots (bottom) for a sphere with a 100 nm diameter made of (a) silver and (b) gold immersed in air. The phasor moves anticlockwise for increasing frequencies and, as clearly seen in (a), crosses the imaginary axis at the plasmon resonance condition. ϵ_p' and ϵ_p'' have been derived from ref 76, and the radiative corrections of eq 8 have been taken into account.

substituting $\langle \mathbf{F}_{DEP} \rangle \rightarrow \mathbf{F}_{DEP}$ and $|\mathbf{E}_{rms}| \rightarrow |\mathbf{E}_{DC}|$ ($|\mathbf{E}_{DC}| \in \mathbb{C}$). However, AC fields are generally employed because they provide no net electrophoretic effect when using conducting samples and allow exploitation of the frequency-dependent properties of the complex Clausius−Mossotti factor. When $\Re(K) > 0$, we conventionally speak of *positive* dielectrophoresis (pDEP), while *negative* dielectrophoresis (nDEP) occurs for $\Re(K) < 0$.

A complete review of the DEP force and its applications in lab-on-a-chip devices is outside the scope of this work, and we refer the interested reader to the corresponding literature.[44,55,62−65] In the following, we will address a few fundamental strategies for the generation of intensity and phase gradients and, in Section 4, highlight some applications of interest.

2.1.2. High-Frequency Regime. When considering optical fields, one usually introduces the total extinction cross section $\gamma = k\alpha''/\epsilon_m'$ and uses Faraday's law, eq 3, to rewrite eq 13 as[36,66]

$$\langle \mathbf{F} \rangle = \frac{\alpha'}{4} \nabla |\mathbf{E_0}|^2 + \frac{\gamma n}{2c} \Re(\mathbf{E_0} \times \mathbf{H_0^*}) + \frac{\gamma c \epsilon_m'}{4\omega i n} \nabla \times \mathbf{E_0} \times \mathbf{E_0^*} \tag{28}$$

The last two terms can now be identified with the nonconservative scattering and spin curl forces ([13]), with n representing, here, the refractive index of the background medium.

At optical frequencies, the bound electrons dominate the response of the particle to the applied electric field, and its dielectric function can then be inferred from transmission electron microscope or spectroscopy measurements.[67,68] Since dielectric particles are usually optically denser than the surrounding medium (i.e., $\epsilon_p' > \epsilon_m'$), they will always be attracted to regions of stronger field. However, the condition $\epsilon_p' < \epsilon_m'$ is verified for some metals in a narrow-frequency window (see Figure 7a) in such a way that it is possible to repel silver colloids from regions of high field intensity. Unfortunately, to the best of our knowledge, this effect has not been shown experimentally. However, trapping in $\epsilon_m' > 2$ media has been shown to yield a negative force on gold particles.[42,69,70] For what concerns ϵ_p'', absorption experiences a strong enhancement for metallic particles excited at their plasmon resonance, while it is generally negligible for dielectric spheres. Interestingly, under suitable illumination conditions, forward or lateral scattering of photons can be enhanced in systems exhibiting Fano resonances, thereby generating unusual negative or transverse scattering forces arising from out-of-phase polarizability oscillations.[71−73] This behavior has not been reported for the intensity gradient force but it could provide a straightforward way to sort different analytes, similar to what was proposed in ref 72. Polarization effects, together with substrate interactions, can also further affect the sign of the optical force.[69,74,75]

https://doi.org/10.1021/acs.chemrev.2c00576
Chem. Rev. 2023, 123, 1680−1711

It is instructive to also note an interesting relationship between the plasmon resonance condition of metallic nanoparticles and the sign and magnitude of the gradient force. At resonance, the complex polarizability phasor is dephased by 90° with respect to the incoming (real) electric field and is therefore purely imaginary. As a consequence, $\Re(\alpha) = 0$, and the plasmon resonance frequency acts as crossover frequency for the gradient force, which changes sign as the frequency of the incoming field is swept through the resonance (this holds for near field gradients, as well[77]). Figure 7a shows exactly how the polarizability phasor crosses the imaginary axis for excitation wavelengths close to the plasmon resonance frequency. Moreover, one can easily note how $\Re(\alpha) > 0$ before the resonance and $\Re(\alpha) < 0$ after, thereby showing this crossover behavior of the gradient force near the plasmon frequency. Since gold has larger losses than silver, this crossover behavior at the plasmon frequency is less pronounced. We further point out that, for the plasmon resonance condition $\epsilon_p' = -2\epsilon_m'$ ([14]), we have $\tau = 0$ and $K \to K_0$. The particle response at this frequency is therefore dominated by surface conduction charges, as is expected for a surface polariton.[80]

Contrary to metallic particles, whose polarizability shows a singularity at the plasmonic resonance frequency (i.e., $\alpha \to \infty$), resonant two-level systems, such as atoms, molecules, or quantum dots, exhibit a saturation behavior that limits the magnitude of their induced dipole moment. For near-resonance excitation, the polarizability of these systems can be written as[36,81]

$$\alpha(\omega) = \frac{\omega_R^2 \hbar}{|\mathbf{E_0}|^2} \frac{4(\omega_0 - \omega) + 2i\gamma}{4(\omega_0 - \omega)^2 + \gamma^2 + 2\omega_R^2} \tag{29}$$

which results in a force (see eq 24)

$$<\mathbf{F}> = \frac{\hbar p}{1 + p}\left[(\omega_0 - \omega)\frac{\nabla|\mathbf{E_0}|}{|\mathbf{E_0}|} + \frac{\gamma}{2}\nabla\phi\right] \tag{30}$$

with

$$p = \frac{2\omega_R^2}{4(\omega_0 - \omega)^2 + \gamma^2} \tag{31}$$

as the saturation parameter, γ as the spontaneous decay rate of the trapped object, and ω_R and ω_0 as its Rabi and transition frequency, respectively. Here again, for resonant excitation, the gradient force vanishes while the scattering component takes its maximum value.

After considering the optical forces acting on resonant analytes, we close this section by examining the forces generated in a resonant nanophotonic cavity.[82] In such a system, an interesting behavior has been observed when a particle interacts with the field inside the cavity. This effect, called self-induced back-action (SIBA), stems from the local refractive index change in the cavity environment brought about by the particle, which causes a spectral shift of the cavity modes. By Newton's third law, this shift is counterbalanced by an additional force acting on the particle, which can greatly affect its dynamics.[83] This force is position-dependent in such a way that, depending on the particle's position inside the cavity, different unconventional regimes can be achieved.[84] For example, it is possible, even for analytes having $\alpha' > 0$, to be attracted toward regions of lower field intensity.[84]

2.2. Higher Orders

Let us briefly extend the previous first-order treatment of electromagnetic forces to cases where the dipolar approximation is not anymore valid, i.e., when the field cannot be considered uniform across the particle. This occurs when the wavelength becomes comparable with, or smaller than, the particle size or in the presence of strong field inhomogeneities, as well as in stationary field points where $\nabla\mathbf{E} = 0$. In these cases, higher order multipolar contributions to $<\mathbf{F_{mix}}>$ are found by inserting $n > 1$ in eqs 12 and 5. Up to the octupolar ($n = 3$) contribution, these terms read[30,32]

$$<\mathbf{F_{mix}}> = \sum_{n=1}^{3} \frac{1}{2}\Re\left(\frac{\underline{\mathbf{p}}[\cdot]^n \nabla^n \mathbf{E}^*}{n!}\right) = \frac{1}{2}\Re(\mathbf{p}\cdot\nabla\mathbf{E}^*) + \frac{1}{4}\Re(\underline{\underline{\mathbf{Q}}}:\nabla\nabla\mathbf{E}^*) + \frac{1}{12}\Re(\underline{\underline{\underline{\mathbf{\Omega}}}}\vdots\nabla\nabla\nabla\mathbf{E}^*) \tag{32}$$

where $\mathbf{p}$ is the dipole moment defined in eq 17, and $\underline{\underline{\mathbf{Q}}}$ and $\underline{\underline{\underline{\mathbf{\Omega}}}}$ are the electric quadrupole and octupole, respectively, which are moments that can, for example, be calculated with the use of eq 5. Triple-underlined quantities represent third-rank tensors, and $\nabla\nabla\mathbf{E}^*$ and $\nabla\nabla\nabla\mathbf{E}^*$ represent the second and third derivative of $\mathbf{E}^*$, respectively.

When multipole moments are simultaneously excited in the particle, their mutual interactions also contribute to generating $<\mathbf{F_s}>$. Up to $n = 3$, this yields[32]

$$<\mathbf{F_s}> = -\frac{k^5}{40\pi\epsilon_m'}\mathfrak{I}(\underline{\underline{\mathbf{Q}}}\cdot\mathbf{p}^*) - \frac{k^7}{630\pi\epsilon_m'}\mathfrak{I}(\underline{\underline{\underline{\mathbf{\Omega}}}}:\underline{\underline{\mathbf{Q}}}^*) \tag{33}$$

We see that, generally, $<\mathbf{F_s}> \simeq 0$ for low-frequency fields, since the high powers of k become smaller and smaller. For clarity and completeness, we also report the expression for the i^{th} component of these two forces:[32]

$$<F_{mix}>_i = \frac{1}{2}\Re(\alpha^{(1)}E_j\partial_i E_j^*) + \frac{1}{4}\Re(\alpha^{(2)}\partial_k E_j\partial_i\partial_k E_j^*) + \frac{1}{12}\Re(\alpha^{(3)}\partial_l\partial_k E_j\partial_i\partial_l\partial_k E_j^*) \tag{34}$$

$$<F_s>_i = -\frac{k^5}{40\pi\epsilon_m'}\mathfrak{I}(\alpha^{(2)}\partial_j E_i\alpha^{(1)}E_j^*) - \frac{k^7}{630\pi\epsilon_m'}\mathfrak{I}(\alpha^{(3)}\partial_i\partial_j E_k\alpha^{(2)}\partial_j E_k^*) \tag{35}$$

where the Einstein summation convention is employed. These additional contributions to the dipolar force of eq 13 have been found to significantly affect the trapping dynamics at low frequencies in quadrupolar electrodes, octupolar field traps, and linear electrode arrays.[85−89] However, while the quadrupolar force can account for up to 10% of the total DEP force acting on a particle with a diameter equal to half of the electrode spacing, it becomes negligible for smaller particles[86,88] and is usually neglected in the majority of applications.

However, at higher frequencies the typical field wavelength becomes comparable or smaller than the particle size, and the higher multipolar contributions come into play.[90] As a result, higher multipolar orders have been more extensively studied at optical frequencies and have found a wider range of applications, for example, in explaining the nonlinear response

https://doi.org/10.1021/acs.chemrev.2c00576
Chem. Rev. 2023, 123, 1680−1711

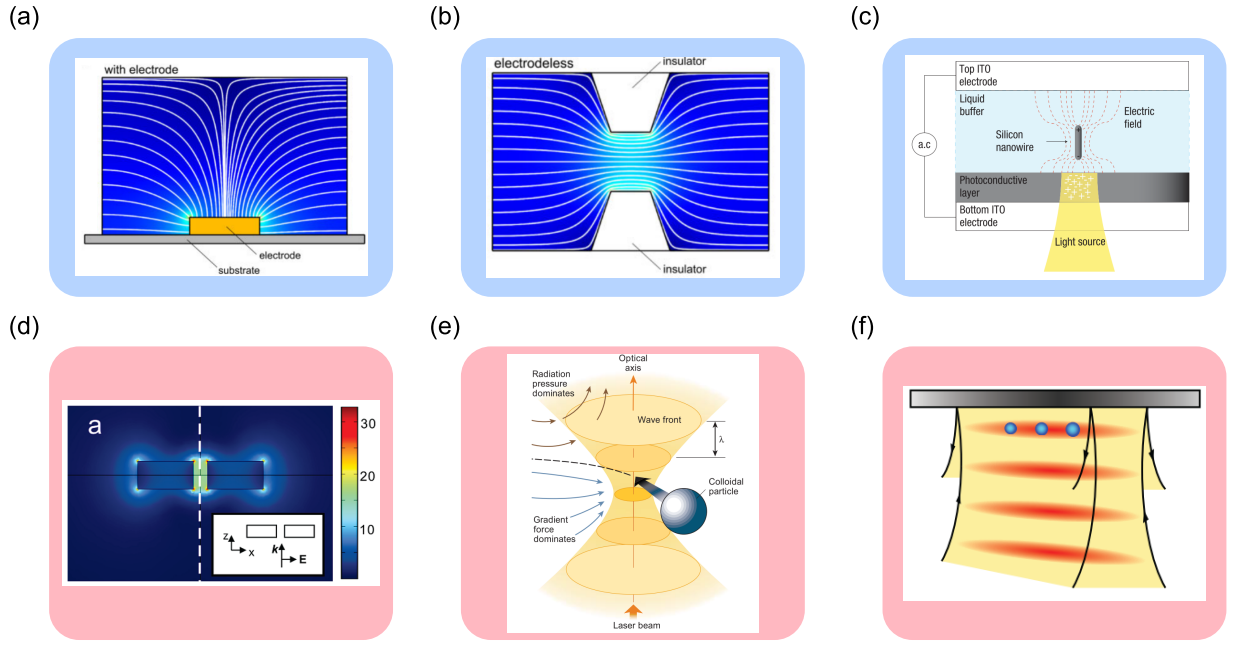

Figure 8. Intensity gradient generation with low- (blue panels) and high- (pink panels) frequency fields. (a) Traditional DEP setup employing metallic electrodes (Reprinted with permission from ref 25. Copyright 2011 Wiley). (b) iDEP employing insulating posts (Reprinted with permission from ref 25. Copyright 2011 Wiley). (c) LIDEP exploiting the photoconductive properties of a-Si:H (Reprinted with permission from ref 124. Copyright 2008 Springer Nature). Note that planar LIDEP geometries have also been proposed.[128] (d) Near-field hotspot generated around a metallic nanostructure (Reprinted with permission from ref 129. Copyright 2010 American Chemical Society). (e) Optical tweezer generated at the focal point of an objective (Reprinted with permission from ref 130. Copyright 2003 Springer Nature). (f) Optical standing wave generated by the interference between an incident laser beam on a mirror and the reflected beam (Adapted with permission from ref 131. Copyright 2011 Optical Society of America).

of optical systems[91] and the spectral features of Fano resonant structures.[92,93] The interference and coupling between different orders has also been used to explain the directional scattering properties of particles and the resulting optical force.[32,37,94−99] Again, we point out that the eq 17 and eq 5, used to calculate the higher order multipoles, are correct only for electrostatic fields. While they can still be safely adopted when the low-frequency fields used in DEP are employed, they do not anymore provide a correct description of the force at higher field frequencies. In this case, the correct values of the multipole moments can be derived by considering radiative corrections to their electrostatic values[94] or by using an equivalent form of eq 5 for their calculation.[100] We warn the reader that different approaches have been developed to do so,[101] and caution must be exercised when performing these calculations.[41]

To conclude this section, let us emphasize that when considering quadrupolar or higher order electric multipoles, magnetic modes need to also be taken into account to provide a full expression of the force. For the sake of clarity and brevity, these additional contributions are not considered here, but we refer the interested reader to the relevant literature on the topic.[29,32,37,102]

2.3. Experimental Platforms for Forces Generation

It is clear from the previous treatment that electromagnetic forces are proportional to the gradients of the field intensity and phase. The realization of such gradients is therefore of paramount importance for the generation of electromagnetic forces, and we begin by reviewing some of the experimental platforms that have been developed to produce low and high frequencies intensity and phase gradients. For simplicity, we treat separately the cases of intensity and phase gradients generation. It is, however, important to keep in mind that, when using optical beams to create electric field intensity hotspots, it is impossible to disentangle the effects of the intensity and phase gradient components of the force, contrary to what is usually done in DEP. This is because propagating beams naturally transfer momentum to an object when they interact with it, in such a way that if a particle is attracted to an optical intensity hotspot, it will also experience there the combined action of the radiation pressure, which we treat in more detail in Section 2.3.2. These multiple interactions result in an overall nonconservative force field where, even if the effects of the nonconservative part are often negligible,[103−106] it is important to keep in mind that both these components are simultaneously affecting the particle dynamics.

2.3.1. Intensity Gradients Generation. The creation of intensity gradients is generally achieved by concentrating the electric field in a region of space called a hotspot, where as a consequence, the intensity takes its maximum value. A simple and straightforward way to generate such a hotspot is to employ a metallic structure that, thanks to its shape, is able to concentrate the field around its edges and therefore generate an intensity gradient in its proximity.[107] This concept is shown in Figure 8a, where an electric potential is applied to a metallic electrode that becomes the source of a low-frequency electric field. Because of a higher concentration of charges around the edges and corners, the field around these areas is stronger and results in the generation of an intensity gradient. Similarly, as shown in Figure 8d, metallic nanostructures of suitable shape can absorb and re-emit optical radiation, thereby generating near-field hotspots around their edges. In general, the use of a metallic support to generate field intensity gradients presents multiple benefits: for example, a metallic electrode can be

https://doi.org/10.1021/acs.chemrev.2c00576
Chem. Rev. 2023, 123, 1680−1711

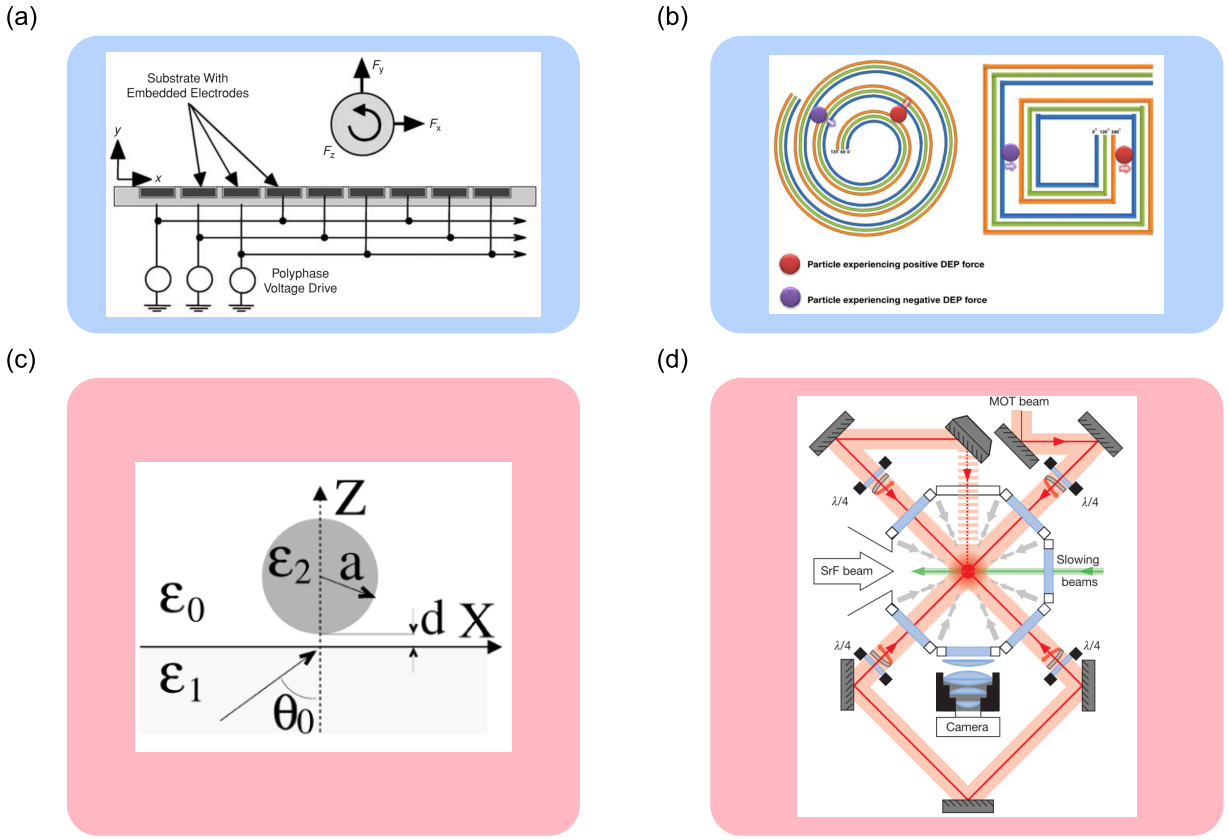

Figure 9. Phase gradient generation with low- (blue panels) and high- (pink panels) frequency fields. (a) A typical TWDEP setup, where multiple electrodes are excited with a polyphase AC voltage generating both a vertical (repulsive) and a horizontal (translating) force (Reprinted with permission from ref 148. Copyright 2003 IEEE). (b) TWDEP devices employed to trap analytes (Reprinted with permission from ref 55. Copyright 2009 Springer Nature). (c) Evanescent wave illumination for the near-field excitation of a particle at the interface between two different media (Reprinted with permission from ref 74. Copyright 2002 Optical Society of America). For dielectric media, illumination at an angle greater than the total reflection angle is needed,[74] while for metallic substrates, momentum-matching conditions need to be satisfied to excite plasmonic evanescent modes at the interface.[151] (d) A magneto-optical trap for atoms and molecule cooling and manipulation (Reprinted with permission from ref 170. Copyright 2014 Springer Nature).

easily integrated with RF equipment to generate low-frequency field hotspots for DEP manipulation, while at optical frequencies, the exploitation of the subwavelength nature of the nanostructures employed allows the simultaneous creation of multiple hotspots and enables the long-range manipulation of analytes.[108,109] Moreover, when two metallic nanostructures are brought close together, dramatic field enhancements are achieved that generate very high optical intensity gradients.[110] Interestingly, similar architectures have now also been proposed for DEP.[111,112] However, DEP manipulation systems usually make use of coplanar 2D electrode structures, often integrated into a microfluidic setup,[113] whose design can unfortunately become very complicated when multiple electrodes and different voltages are required for complex multipurpose devices.[114,115] Moreover, the use of a coplanar geometry means that the gradients do not extend to the whole liquid chamber on top of the electrodes, thus limiting the final device throughput. This limitation can be overcome by using electrodeless or insulator-based DEP (iDEP).[25,116−118] In this configuration, the field gradients are generated using insulating structures in the fluid, as depicted in Figure 8b. Moreover, the use of DC fields allows the simultaneous exploitation of electrokinetic phenomena (electrophoresis and electro-osmosis) and DEP, thereby resulting in complex particle dynamics.[119,120] A combination of DC and AC voltages has also been shown to overcome the need to use very strong (up to a few kV) DC fields.[120−122] Another hybrid approach to generate low-frequency electric field gradients is the creation of "floating" electrodes in a photoconductive material such as a-Si:H under light illumination, as depicted in Figure 8c. This approach, termed light-induced dielectrophoresis (LIDEP), is an elegant combination of optical and electrical effects that allows the dynamic reconfiguration of the DEP field with the use of light-shaping techniques, which enables massive parallel trapping and manipulation of analytes and liquid samples.[123−127]

In the optical regime, the metallic nanostructures employed are usually excited close to their plasmonic resonance, where their near field is enhanced,[132] and are therefore called *plasmonic tweezers*.[110,129,133] These tweezers are usually patterned on a dielectric substrate using cleanroom fabrication techniques, but metal colloids provide the same field enhancement and can, in principle, be used for the same applications.[134−136] Similarly, nanoscale apertures in metallic films also provide near field enhancements and can be used for the trapping and detection of nanoscale analytes.[6,137] Moreover, the use of multiple interacting structures, such as particle dimers, allows for further confinement of the field to deep subwavelength volumes and provides a platform to study enhanced optical forces and strong light−matter interac-

https://doi.org/10.1021/acs.chemrev.2c00576
Chem. Rev. 2023, 123, 1680−1711

tions.[129,138,139] The scattering force in these systems is generally normal to the substrate and pushes the particle away from (or toward) the field hotspots if the exciting beam illuminates the structures from the substrate (or the environment). Alternatively, the metallic structures can be excited with an evanescent wave generated at the interface between the substrate and the environment,[140] i.e., because of total internal reflection, as shown in Figure 9c. This configuration provides an additional intensity gradient force normal to the substrate and a scattering force parallel to it.

Unfortunately, the use of plasmonic tweezers requires access to cleanroom fabrication techniques that makes their realization very costly and time-consuming.[141,142] For this reason, in applications that do not require nanoscale analyte confinement, *optical tweezers* are usually used. These are optical intensity gradients created at the focal point of an objective lens, as shown in Figure 8e. In these hotspots, the particle experiences not only the intensity force but also its phase gradient counterpart in the form of radiation pressure, and if one wants to achieve stable trapping of the analyte, the former force needs to overcome the latter. As first recognized by Ashkin et al., this can be achieved by employing high numerical aperture objectives (NA > 1.2) to create a diffraction-limited hotspot.[16,51] Lower NA objectives can, in principle, also be used, but they do not provide enough field confinement for the intensity gradient force to overcome the radiation pressure. Similarly, the scattering force also limits the laser power intensity that can be used in these setups—especially when trapping very large (>10 μm) particles—to a few hundreds of mW/μm^2 and therefore sets some constraints to the maximum value of the achievable field gradient. Meanwhile, a minimum intensity of 1 mW/μm^2 is generally required for the field gradient force to overcome the radiation pressure.[143] Alternatively, as shown in Figure 8f, intensity hotspots can be generated at the antinodes of standing waves created by the interference of two counter-propagating laser beams.[144] The advantage of this configuration is the almost complete cancellation of the radiation pressure acting on the particle, since the two components of the scattering force act in opposite directions and cancel each other out ([15]). This allows a more stable trapping than in conventional optical tweezers, although the latter are easier to realize and offer greater tunability to address a wider range of applications in the physical and biological sciences.[145] Unfortunately, because of the r^3 dependence of the polarizability (see eq 15), these far-field interactions can typically generate sufficient forces to efficiently manipulate microsized objects only. For smaller particles, different approaches have to be devised.[146]

2.3.2. Phase Gradients Generation. Differently from intensity gradients, where the field is usually focused into a hotspot, phase gradients provide a constant force in the direction of propagation of an electromagnetic wave and are therefore better suited for the transport of analytes. Because of the traveling nature of optical waves, these naturally carry a phase gradient along their propagation direction that is responsible for the generation of radiation pressure forces: since the phase of the wave linearly increases from 0 to 2π as one moves one wavelength along the propagation direction, consequently, an object is pushed along the wave if $\mathfrak{I}(K) > 0$ or pulled against it if $\mathfrak{I}(K) < 0$. Unfortunately, in the low-frequency case, electric fields are usually confined between two electrodes and do not propagate in space. As a consequence, no phase gradient is generated in a standard DEP setup. Low-frequency electrical traveling waves can nonetheless be produced using a multielectrode system where a phase-shifted signal is applied to each terminal, thus generating a phase gradient. In such a configuration, a particle hovering above the electrodes is then pushed along or against the traveling wave depending on its properties and on its height above the substrate,[147,148] as shown in Figure 9a,b, in a phenomenon termed *traveling wave dielectrophoresis* (TWDEP).[55] Because of the presence of a phase nonuniformity, the particle also rotates as it moves along the electrodes, which is a phenomenon termed *electrorotation* (ER or ROT).[149] Multiple signals, of different amplitudes and frequencies can also be applied to provide better manipulation capabilities[150] ([16]). Particle actuation is usually performed at frequencies where $\mathfrak{R}(K) < 0$, and the resulting negative intensity DEP force is balanced by the gravitational attraction on the particle, which provides stable trapping of the analyte at a specific distance above the substrate. The particle is then free to move along the electrodes under the influence of the phase gradient force without sticking to the electrodes. In a similar configuration, phase gradients can also be generated by using optical evanescent waves, as shown in Figure 9c. In this case, the wave created at the interface between two media provides the intensity gradient force pulling the particle toward the substrate, while scattering forces generate transverse motion.[151−154] As already pointed out, when working with metallic particles, the evanescent wave gradient force disappears at the plasmon resonance frequency, exactly where the scattering force is strongest.[42,74] Unfortunately, heating effects due to photon−phonon conversion can become detrimental when employing a beam tuned at the particle's resonant frequency. In particular, depending on the particle size and laser power employed, a local temperature increase up to a few tens of degrees can occur in the vicinity of the particle,[155] thereby potentially damaging other biological species in the sample[156] and generating convection currents in the surrounding fluid.[157,158] A different wavelength should therefore be used to provide the desired trade-off between the relative strength of the intensity and phase gradient forces and the heating effects ([17]). Aside from the simple setup in Figure 9c, light-shaping techniques can also be used to design more complex beams that allow for complete three-dimensional particle manipulation.[130,165] For example, transverse phase gradients have been used to create transport lines of arbitrary shape for the manipulation of metallic nanoparticles,[166,167] while tractor beams have been employed to actuate Mie particles.[168,169]

Aside from analyte transport, phase gradients can also be employed to trap particles in systems of counter-propagating traveling waves. For instance, classical TWDEP setups can be modified to have an arrangement of spiralling concentric electrodes, as shown in Figure 9b. This way, a user creates concentric and counter-propagating traveling fields, which propagate toward (or from, depending on the chosen electrodes phase) the center of the configuration. Particles are therefore attracted to or repelled from this site depending on the sign of $\mathfrak{I}(K)$. In the optical domain, counter-propagating traveling waves can be easily realized by employing a system of three counter-propagating laser beams, such as the one shown in Figure 9d, where the opposing radiation pressure forces from the different waves can confine an object at the intersection point between the beams. Arguably, the most important application of this configuration

https://doi.org/10.1021/acs.chemrev.2c00576
Chem. Rev. 2023, 123, 1680−1711

has been the cooling of clouds of resonant atoms, which was recognized with the award of the 1997 Nobel Prize in Physics to Chu, Cohen-Tannoudji, and Phillips.[5] To this end, by referring to eqs 30 and 31, the scattering force for near-resonant excitation far from saturation can be written as

$$<\mathbf{F}_{\mathrm{scatt}}> = \frac{\hbar\omega_R^2\gamma}{4(\omega_0-\omega)^2+\gamma^2+2\omega_R^2}\mathbf{k} \tag{36}$$

If the lasers are tuned to a frequency slightly below ω_0, photon absorption is enhanced in atoms moving against the beam because of the Doppler effect. According to momentum conservation, the atoms are therefore slowed down, lose kinetic energy, and decrease their temperature.[171] An additional gradient force needs to be applied to achieve stable trapping of the cooled atoms to enable full control over the trapped objects.[50,172] This effect has not been reported for low-frequency electrical fields since their frequency (kHz to GHz) is usually far from the resonant frequencies of typical trapped analytes ($\sim 10^2$ THz), but it should be possible, in principle. Similar systems of counter-propagating evanescent waves have also been used to trap particles at the intensity hotspot created by the constructive interference of two propagating plasmonic modes.[153,154] Finally, optical phase gradients can also be generated along the antinodes of a standing wave[131] or in an optical lattice.[173]

3. TORQUES

After considering the generation of electromagnetic forces on micro- and nanoscale analytes, let us show how these forces can set a particle into rotational motion through a torque. From a theoretical point of view, the time-averaged mechanical torque $<\boldsymbol{\tau}>$ exerted on a particle can be found through the well-known formula

$$<\boldsymbol{\tau}> = <\mathbf{r}\times\mathbf{F}> = <\int_{\partial V}\mathbf{r}\cdot\mathbf{n}\times(\underline{\underline{\mathbf{T}}}\cdot\mathbf{n})dA> \tag{37}$$

where $\mathbf{r}$ is the vector going from the rotation axis to the point where the force $\mathbf{F}$ is applied. It is important to point out that a particle can be set into two different kinds of rotational motions: one around an axis passing through the particle's center of mass and another one around an external axis, as shown in Figure 10. We refer to the former as *spinning* and the latter as *orbiting*.[174] The total torque acting on the particle is therefore the sum of the spin and orbital torques

$$<\boldsymbol{\tau}> = <\boldsymbol{\tau}_S> + <\boldsymbol{\tau}_O> \tag{38}$$

An expression for the spin torque can be found by considering the force given by eq 12, which yields[30,35]

$$<\boldsymbol{\tau}_S> = \sum_{n=1}^{\infty}\frac{1}{2}\Re\left[\frac{1}{(n-1)!}\left(\underset{\cdot\cdot n}{\underline{\mathbf{p}}}[\cdot]^{(n-1)}\nabla^{(n-1)}\right)\times\mathbf{E}^*\right] + <\boldsymbol{\tau}_I> \tag{39}$$

where $<\boldsymbol{\tau}_I>$ is an interference torque arising from the mutual interference between multipoles. It can be expressed as[175]

$$<\boldsymbol{\tau}_I> = -\sum_{n=1}^{\infty}\Im\left[\frac{k^{2n+1}}{8\pi\epsilon_m'}\frac{2^n(n+1)}{(2n+1)!}\left(\underset{\cdot\cdot\cdot n}{\underline{\mathbf{p}}}\overset{(n-1)}{\cdot\cdot\cdot}\underset{\cdot\cdot n}{\underline{\mathbf{p}}}^*\right)\overset{(2)}{\cdot\cdot\cdot}\overleftrightarrow{\boldsymbol{\epsilon}}\right] \tag{40}$$

where $\overleftrightarrow{\boldsymbol{\epsilon}}$ is the Levi-Civita tensor and $\overset{(n-1)}{\cdot\cdot\cdot}$ and $\overset{(2)}{\cdot\cdot\cdot}$ are tensor contractions defined in ref 175. Likewise, the orbital torque is

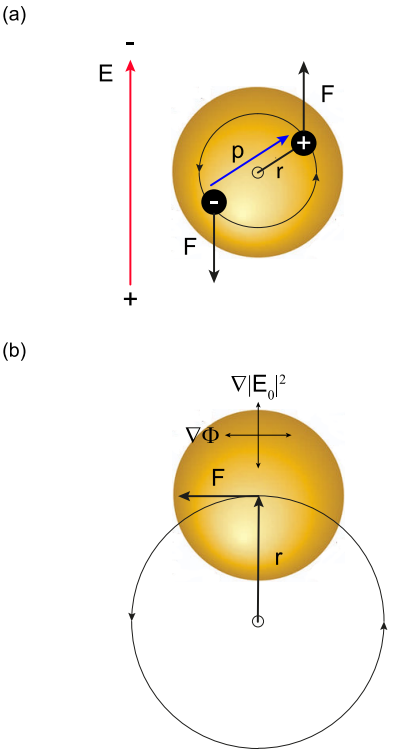

Figure 10. Spin and orbital torque. (a) A particle spinning around its center of mass. (b) The same particle can be set into orbit around an external axis. The directions of the intensity and phase gradients for a typical vortex beam are also shown. Here, the torque $\boldsymbol{\tau}$ is a vector coming out of the page toward the reader.

$$<\boldsymbol{\tau}_O> = \sum_{n=0}^{\infty}\frac{1}{2}\Re\left[\mathbf{r}\times\left(\frac{\underset{\cdot\cdot n}{\underline{\mathbf{p}}}[\cdot]^n\nabla^n\mathbf{E}^*}{n!}\right)\right] + <\mathbf{r}\times\mathbf{F}_s> \tag{41}$$

Analogous expressions have also been derived in the dipolar approximation for arbitrarily shaped incident electromagnetic fields.[176] We highlight the fact that the spin torque $<\boldsymbol{\tau}_S>$ is not defined for $n = 0$, thereby expressing the fact that one cannot set an electrical charge immersed in a uniform field into spinning motion around its center. As a consequence, the only torque acting on a charge is an orbital torque, which sets it into circular motion around an axis under the influence, for example, of an annular electric field. This can be created, for instance, by employing magnetic coils.[177]

3.1. First Order

After setting $n = 1$ in eqs 39, 40, and 41, we get the expression for the total torque acting on a point dipole:

$$<\boldsymbol{\tau}> = \frac{1}{2}\Re(\mathbf{p}\times\mathbf{E}^*) + \frac{k^3}{12\pi\epsilon_m'}\Im(\mathbf{p}\times\mathbf{p}^*) + \frac{1}{2}\Re[\mathbf{r}\times(\mathbf{p}\cdot\nabla\mathbf{E}^*)] \tag{42}$$

Here, the first term represents the spin torque, the second describes the interference spin torque, and the last component expresses the orbital torque. The interference torque usually produces negligible effects on the particle and will therefore not be further discussed here. As for the remaining two terms, we see that the spin torque depends on the field $\mathbf{E}^*$, while the orbital torque is generated by its gradient $\nabla\mathbf{E}^*$. It is important

https://doi.org/10.1021/acs.chemrev.2c00576
Chem. Rev. 2023, 123, 1680−1711

to recall now that, as mentioned toward the end of Section 1.2, the field **E** can only interact with the charges present in the particle, while $\nabla\mathbf{E}$ will interact with the induced dipole. As a consequence, when studying the spin torque, one cannot investigate the behavior of the induced dipole in the particle but rather has to analyze the forces acting on the two induced charges that build up the dipole. These forces are mainly the result of Coulomb interactions between these charges and those generating the field, as shown in Figure 10a. We see, here, that the field induces a couple of opposing forces with the same magnitude that will not generate any linear motion of the particle but will rather make it spin until **p** is aligned with $\mathbf{E}^*$, in accordance with the first term of eq 42. However, because the orbital torque generates a complete displacement of the particle in space, it can be simply described as the result of intensity and phase gradient forces, as described in Section 2.1, acting on its induced dipole.

We will now describe in greater detail the generation of spin and orbital torques from Coulomb and dipolar forces, respectively.

3.1.1. Spin Torque in Low- and High-Frequency Fields. We start our discussion on the spin torque by first noticing that, for this torque to be nonzero, the dipole moment **p** needs to point a different direction than the incoming electric field $\mathbf{E}^*$ (see eq 42), as shown in Figure 11. Under this

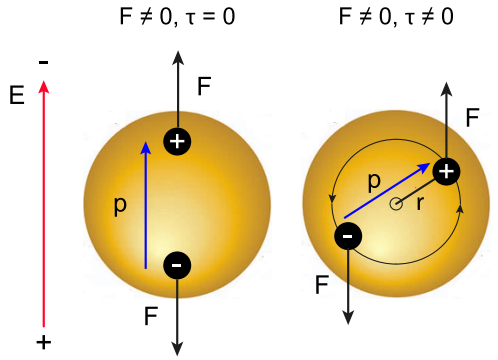

Figure 11. Condition for spin torque generation. On the left, the polarization vector in an isotropic and lossless material points in the same direction as the incoming electric field, thereby preventing the generation of a torque. On the right, the polarization in an anisotropic and/or lossy material can be noncollinear with the electric field, which gives rise to a torque.

configuration, a restoring torque is created on the particle and will tend to align **p** to $\mathbf{E}^*$. Once these two vectors are aligned, the spin torque is zero and the particle only experiences the action of the dipolar force $1/2\Re(\mathbf{p}\cdot\nabla\mathbf{E}^*)$ and the resulting orbital torque. If, however, the direction of the electric field vector continuously changes, for example, in circularly polarized fields, then the particle experiences a continuous rotation around its center as it tries to align its dipole moment to $\mathbf{E}^*$. In what follows, we describe the two main physical mechanisms that lead to the creation of noncollinear electric fields and polarizations, namely, the presence of absorption and/or anisotropy in the particle.

Let us first consider the spin torque generated on an absorptive particle by a right circularly polarized electric field propagating in the positive z direction. For such an excitation, the complex amplitude of the field is

$$\mathbf{E}_0(\mathbf{r}) = \mathbf{E}_0'(\mathbf{x} - i\mathbf{y}) \tag{43}$$

and the resulting torque exerted on the particle will be (see eqs 42, 43, and 17)

$$<\boldsymbol{\tau}_S> = \frac{1}{2}\Re(\alpha\mathbf{E}\times\mathbf{E}^*) = -\alpha''|\mathbf{E}_0'|^2\mathbf{z} \tag{44}$$

where **x**, **y**, and **z** are the Cartesian unit vectors. This expression shows that any absorbing particle ($\alpha'' \neq 0$) experiences a spin torque whose magnitude is proportional to the amount of loss or gain present in the material, as also depicted in the left panel of Figure 12a. We see here that the delay δ between the electric field and the polarization vector is proportional to α'', and moreover, $0 < \delta < \pi$, and the polarization is ahead of the field in gain media (i.e., for $\alpha'' < 0$). However, the direction of the torque is controlled by the sign of α'' in such a way that the torque acting on a lossy object points toward $-z$ and sets the particle into rotation with the field, as shown on the right of Figure 12a. Here, the charges generating the field repel the induced polarization charges and push the particle to follow the field rotation. Conversely, we see that a particle made of a gain material will spin in the opposite direction, against the field, because its torque is directed toward z ([18]). Interestingly, lossy metallic particles and rods immersed into an electrolyte solution have also been observed to spin against the field at frequencies smaller than $1/\tau_{EDL}$.[46,47] At these frequencies, the charging of the EDL at the metal−electrolyte interface results in a negative imaginary part of the polarizability in such a way that a metallic particle behaves as a gain material and spins against the field.[179] We stress that, regardless of the sign of α'', the polarization vector always rotates synchronously with the electric field; therefore, the induced charges always follow the field. Finally, the final rotation frequency of the object depends on many experimental factors, most notably on the viscous drag force exerted by the medium proportional to its viscosity. For cells, a few rotations per second are usually observed, while metallic nanoparticles can spin at frequencies up to several kilohertz.[180]

The other mechanism that generates noncollinear polarization and electric field vectors, thereby giving raise to a spin torque, is the presence of anisotropy in the particle. While this review is mainly concerned with isotropic materials, anisotropy has been greatly exploited for the generation of torques with both low- and high-frequency fields and deserves, therefore, at least an introductory treatment. Generally speaking, anisotropy is the feature of a material property to behave differently in different directions. For instance, crystals with noncubic structure can interact differently with electromagnetic waves depending on the crystal axis along which the waves are polarized.[181] As an example, a beam of light interacting with a block of calcite experiences different refractive indices (and therefore polarizes the material differently) according to its polarization direction, which is a property commonly known as *birefrengence*. Alternatively, anisotropy is also created by asymmetric particle shapes, which generates different dipole moments along the different particle axes. The presence of this anisotropy in the particle polarizability can set it into spinning motion, as shown in Figure 12b. We stress the fact that anisotropy can also arise in spherical and lossless particles, as shown on the left of Figure 12b; therefore, this mechanism of torque generation is fundamentally different from the one treated above for the case of absorptive materials. A complete and rigorous mathematical description of anisotropic materials

https://doi.org/10.1021/acs.chemrev.2c00576
Chem. Rev. 2023, 123, 1680−1711

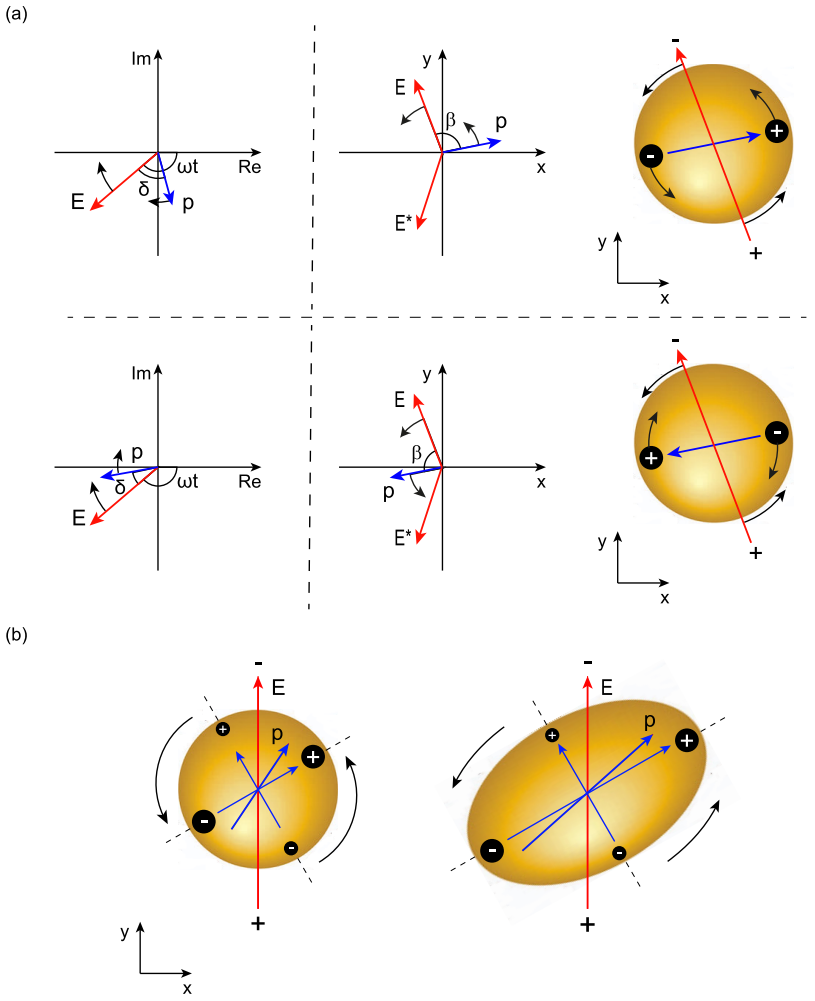

Figure 12. Spin torque generation. (a) Phasor (left) and real space (right) diagrams for a right circularly polarized field interacting with a lossy (top) or gain (bottom) particle. (b) Material (left) or shape (right) anisotropies induce different polarizations along two different directions, which generates a torque.

is beyond the scope of this work, so let it suffice to say that in these materials the polarizability is better described as a second-order tensor

$$\underline{\underline{\boldsymbol{\alpha}}} = \begin{pmatrix} \alpha_{xx} & 0 & 0 \\ 0 & \alpha_{yy} & 0 \\ 0 & 0 & \alpha_{zz} \end{pmatrix} \tag{45}$$

whose components represent the different polarizabilities along different directions ([19]). For simplicity, we are considering nonabsorptive materials for which $\underline{\underline{\boldsymbol{\alpha}}}$ is real. When a particle made of such a material is excited by a linearly polarized electric field propagating along z, the resulting torque is

$$\langle \boldsymbol{\tau}_S \rangle = \frac{1}{4} |\mathbf{E_0}|^2 (\alpha_{xx} - \alpha_{yy}) \sin(2\beta)\mathbf{z} \tag{46}$$

where β is the angle between the polarization and electric field vectors[182] shown in Figure 12. We see that this torque will act on the particle in order to realign the polarization with the electric field in such a way that $\beta = 0$. One can, therefore, control the orientation of the particle simply by changing the direction of the field, which is the reason why this torque is sometimes called the *reorientation* torque. If the polarization of the field is continuously changed, such as in circularly polarized fields, the particle will then generally tend to follow the field.[183] It is instructive to compare eq 46 with eq 44 in order to fully understand the differences between the two mechanisms of spin torque generation. We see that in both cases the torque is proportional to the intensity of the incoming field. Moreover, the anisotropy-generated torque is proportional to the anisotropy present in the material, $\alpha_{xx}-\alpha_{yy}$, and the angle β between the polarization and electric field vectors. In eq 46, the polarizability components are real, which shows how this torque can also act on lossless materials. However, absorption processes induce a torque proportional to α'', which demonstrates the fundamental difference between these two processes of spin torque generation. Clearly, both torques come into play when studying absorptive anisotropic particles, such as metallic nanorods. We conclude this discussion on spin torques by examining the final orientation of an anisotropic elongated particle under the influence of a linearly polarized field. One might expect the particle to align with its longest axis parallel to the field because the polarizability is greater along that direction. While this is always the case for DC fields, there have been several experimental reports of metallic nanorods and ellipsoidal cells aligning *perpendicularly* to time-varying electric fields.[184,185] This behavior can be explained by the presence of different charge relaxation times (see eq 20) along

https://doi.org/10.1021/acs.chemrev.2c00576
Chem. Rev. 2023, 123, 1680−1711

each of the particle's axes, thereby generating an uneven distribution of charges along the particle.[29] For a given particle−medium system, these relaxation times depend on the frequency of the excitation field and independently affect the values of the polarizability components in eq 45. Therefore, depending on the frequency of the applied field, the relative magnitudes of the polarizabilities change and can alter the sign of the torque experienced by the particle along a specific direction (see eq 46). This, in turn, results in a realignment of the particle along a different axis.[29]

3.1.2. Orbital Torque in High-Frequency Fields. We now turn our attention to the last term of eq 42. This describes the orbital torque of a dipolar particle under the influence of a force of the kind expressed by eq 13 and, as a consequence, takes into account the effects of both intensity and phase gradient forces. We first notice that, to generate a continuous orbiting motion, these gradients need to steadily provide a nonzero force to the particle. This is clearly not the case for intensity gradients, which tend to trap and then immobilize a particle in the regions of highest field intensity, where the field gradient force is zero. However, as shown in Figure 9, phase gradients can provide a continuous nonzero force that can create a stable orbital torque. This concept is further explained in Figure 10, right, where we show how, in a typical orbiting system, the phase and intensity gradients are respectively perpendicular and parallel to $\mathbf{r}$ (see also Figure 14). Consequently, as predicted by eq 42, the orbital torque generated by the intensity gradient force is zero, and only phase gradient forces are called into action when generating orbital motion. Next, we point out that, to the best of our knowledge, no orbiting of single particles using low-frequency fields has been reported in the literature, even though it would be, in principle, possible to observe it in an ROT setup (see Figure 13a) for particles smaller than the electrode size. Additionally, these setups have successfully produced orbital motion of binary particle systems,[186,187] while hydrodynamic and thermal effects have also been exploited in combination with RF and optical fields for the creation of fluid vortices, thereby effectively setting micro and nanoparticles into orbital motion.[188−190] However, "true" orbital torque acting on a single particle caused by phase inhomogeneities in the field has been generated only at optical frequencies where the analogy between paraxial optics and quantum mechanics[191] allows the simultaneous treatment of both the spin and orbital torque. In this framework, the total torque acting on a particle under the influence of a light beam can be written as[192]

$$\langle \boldsymbol{\tau} \rangle = \langle \boldsymbol{\tau}_S \rangle + \langle \boldsymbol{\tau}_O \rangle = \frac{P_{abs}}{\omega}(\sigma_s + l) \tag{47}$$

where P_{abs} is the power absorbed by the particle; $\sigma_s = \pm 1$ for left/right circularly polarized light, respectively, and 0 for linearly polarized fields; while l is the so-called *topological charge* of the beam. We see, here, that the total torque is divided into two components: one depending on σ_s and representing the polarization-dependent spin torque and another one depending on l, which represents the orbital torque. To this end, we point out that while eq 47 is derived within the paraxial approximation (i.e., in the case of weakly focused light beams) for Laguerre−Gaussian laser modes,[193] it still provides an *exact* description of the torque for a general near-cylindrical and nonparaxial beam, as long as this is linearly polarized (i.e., $\sigma_s = 0$).[194] However, for a more general polarization state, it is no longer possible to fully separate the spin and orbital torque in terms depending only on σ_s and l, while an additional corrective term needs to also be included in eq 47.[194] Luckily, the relative magnitude of this term is small and contributes up to a maximum 20% of the total torque even in beams focused only one wavelength across.[192] As a consequence, eq 47 has been successfully employed to also describe the torque exerted by optical fields focused by objectives having a high NA, up to 1.3.[192,195] We conclude by noting that, since P_{abs} is proportional to α'', the orbital torque is also proportional to the amount of losses present in the particle's material. The orbital motion can then be basically interpreted as the result of radiation pressure interactions (i.e., phase gradient forces) acting on the particle, and as a consequence, we can expect objects made of gain materials, which experience negative scattering forces, to orbit in the opposite direction from lossy particles, even though this phenomenon has not been observed experimentally.

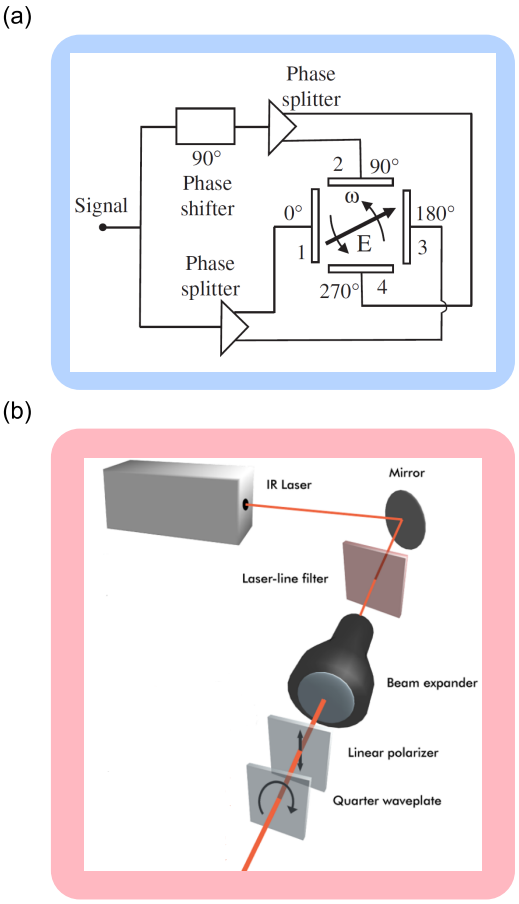

Figure 13. Generation of circularly polarized fields. (a) A typical ROT setup to produce left circularly polarized RF fields (Reprinted with permission from ref 64. Copyright 2017 Wiley), where each electrode is dephased by 90° with respect to the adjacent ones. (b) A combination of a linear polarizer and a quarter-wave plate converts an unpolarized laser beam to a circularly polarized electromagnetic wave (Adapted with permission from ref 180. Copyright 2013 American Chemical Society).

3.2. Higher Orders

While investigated theoretically,[30,35,196−198] the generation of electromagnetic torques arising from higher order multipole moments has not been the subject of a great deal of experimental attention. At low frequencies, quadrupolar contributions to the total torque have numerically been

https://doi.org/10.1021/acs.chemrev.2c00576
Chem. Rev. 2023, 123, 1680−1711

found to be negligible as long as the particle is placed far from the electrodes generating the field, but can account for up to 20% of the torque when the cell is brought closer to these electrodes.[199] At optical frequencies, we highlight the fact that eq 47 already provides a general description of the *total* torque acting on a particle and therefore takes into account *all* its multipolar contributions. As a consequence, less attention has been given to the study of its multipolar components, but these can, in principle, be calculated by substituting proper expressions for the multipoles into eq 39.[41] We conclude by mentioning that the generation of torque-employing magnetic fields is also possible and, to this end, we refer the interested reader to the relevant literature.[200]

3.3. Experimental Platforms for Torque Generation

For the spin torque, circularly polarized low-frequency fields can be created with a polyphase quadrupole electrode configuration, as shown in Figure 13a. When these fields are used to set a particle into spinning motion, we usually speak of *electrorotation* (ER or ROT), a technique that has found tremendous applications in biology, for example, for the determination of the membrane capacitance and the cytoplasmic conductivity of cells.[29] Alternatively, circularly polarized high-frequency fields can be readily produced by suitably polarizing an electromagnetic wave, for example, with the use of a quarter-wave plate (Figure 13b), and have been successfully used to set lossy particles into spinning motion.[180,192] We point out that, as was already the case for phase gradient forces, the torque exerted on a metallic particle is enhanced close to its plasmonic resonance when α'' takes its extreme value.

For the generation of orbital torque, phase gradients can be readily created in an optical beam with the use of spatial light modulators (SLMs), metasurfaces, or waveplates.[201,202] Such beams have been investigated since the 90s for their ability to transfer orbital angular momentum to trapped particles.[192,195,203] An example of a typical laser beam used to generate orbital motion is the vortex beam shown in Figure 14. This beam has an annular intensity distribution that traps a particle away from the center of the beam in the plane transverse to its propagation direction.[204] A linear phase gradient is then created in this plane by tailoring the topological charge l of the beam, as shown in Figure 14. Under this configuration, a particle will then move in orbital motion around the center of the beam toward higher or lower phases. However, it should be noted that if the particle under study is larger than the beam waist, the particle will be trapped in the center of the beam, and the effect of the orbital torque will thus be to make it spin, rather than orbit, around the beam center.[192]

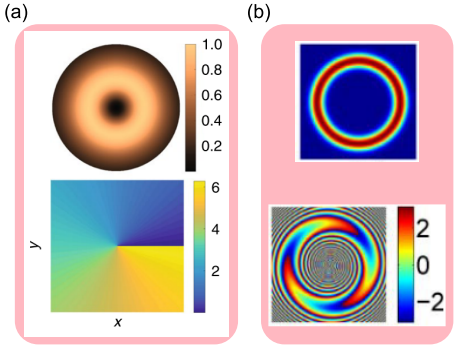

Figure 14. Generations of optical fields carrying orbital angular momentum. In particular, the intensity (top) and phase (bottom) profiles of a vortex beam having (a) $l = 1$ (Reprinted with permission from ref 205. Copyright 2020 Springer Nature) and (b) $l = 3$ (Adapted with permission from ref 204. Copyright 2013 Optical Society of America) are shown.

4. APPLICATIONS

Let us briefly review the main applications of low- and high-frequency forces and torques for the manipulation of micro- and nano-objects. We start by warning that the sizes of the particles considered here span a very wide range, from a few tens of microns for dielectric spheres and cells down to a few nanometers for molecules. While the interactions of the RF fields used for DEP (whose wavelengths range from a few meters to several thousands of kilometers) with objects of these dimensions can be perfectly described within the dipolar approximation that is the focus of this work, greater care is needed when considering high-frequency fields. The typical laser wavelengths used in optical setups are between 500 and 1100 nm, and as a consequence, the optical forces generated on micron-sized objects are usually better described within the framework of ray optics[206] or by considering higher order multipoles, as outlined in Sections 2.2 and 3.2.[41] Nonetheless, the dipolar approximation still provides a qualitatively accurate description of such systems,[197] and we will, therefore, cite here a number of works in which this approximation is not strictly satisfied. Aside from this, we recall that the polarizability of an object is directly proportional to its volume (see eq 15), and consequently, the force generated on larger (>1 μm) particles is stronger than that generated on nanosized objects, which can make their manipulation easier. Besides its size, it is clear from eq 24 that the force acting on a particle can be controlled by tuning its dielectric properties (ϵ_p), the solution (ϵ_m, for example by changing its conductivity), the frequency of the field (and therefore K), and its intensity and phase distributions. The torques, being derived from the forces, can be controlled in a similar fashion. For targeted applications, there is little freedom over the choice of the analyte and background medium, so modification of the field intensity and phase distribution usually provides the easiest and most straightforward way to control the motion of a particle. We have already outlined in Sections 2.3 and 3.3 the most common experimental platforms to create different and controllable intensity and phase distributions and we will review, here, their applications for the trapping, assembly, and transport of micro- and nanoscale analytes.

4.1. Trapping

By trapping, we mean immobilizing the object of interest in a predefined region of space, usually a field or phase extremum. This immobilization can allow, for example, further characterization of the trapped object or its transport and/or assembly into more complex structures, as depicted in Figures 15 and 16. It therefore represents a key enabling capability for many micro- and nanosystems designed for analyte manipulation. Trapping with optical tweezers, presented in Figure 8e, has enjoyed a greater attention from the research community compared with DEP trapping, largely thanks to its easier realization, which only requires a laser and a high NA objective, as opposed to the IC fabrication facilities needed for the realization of DEP electrodes (see Figure 8a,b). Moreover, the combination of optical beams with SLMs enables the

https://doi.org/10.1021/acs.chemrev.2c00576
Chem. Rev. 2023, 123, 1680−1711

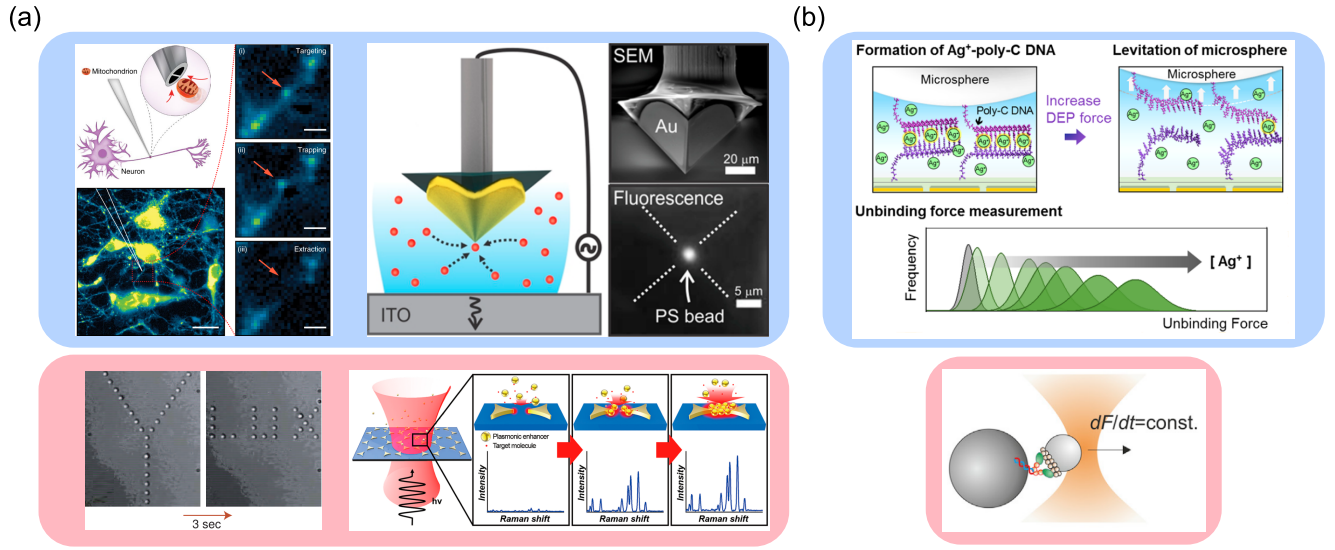

Figure 15. Analyte trapping with the use of intensity gradients. Panel (a) shows, in clockwise order from the top left figure, the use of DEP forces for mitochondrion removal (Reprinted with permission from ref 15. Copyright 2019 Springer Nature), particle trapping (Reprinted with permission from ref 11. Copyright 2014 American Chemical Society), and the use of optical forces for molecular trapping and sensing (Reprinted with permission from ref 226. Copyright 2016 American Chemical Society) and particle manipulation (Adapted with permission from ref 227. Copyright 2006 Optical Society of America). Panel (b) shows, on the top, the use of DEP force spectroscopy to detect Ag ions (Reprinted with permission from ref 228. Copyright 2016 American Chemical Society) and, on the bottom, the use of optical tweezers for molecular force spectroscopy (Adapted with permission from ref 229. Copyright 2013 Biophysical Society).

dynamical reconfiguration of both the field intensity and phase distributions, thereby allowing this technique to address an ever-growing number of applications.[10,130,143,146,207−212] Despite this, DEP trapping has, itself, developed into a lively research field in the past decades where both positive and negative DEP have been used to demonstrate microparticles and cells concentration and separation, which are now routinely implemented in lab-on-a-chip and μTAS devices.[53,128,213−218] For example, through the exploitation of the different dielectrophoretic properties of viable and nonviable cells, healthy *Saccharomyces cerevisiae* and human breast cells have been successfully separated from heterogeneous samples,[213,219] while the antibiotic resistance of *Staphylococcus* bacteria has also been characterized using DEP.[220] DEP trapping of nanoscale analytes, such as nanoparticles and nanotubes[11,221,222] and biomolecules,[15,164,222,223] has also been demonstrated and is usually combined with other sensing platforms, such as nanopores[224] or Raman spectrometers.[222,225] Similarly, optical tweezers have been applied to the trapping and sorting of cells[230,231] and particles,[24,227,232−235] and to molecular studies.[9,236] To this end, after the initial reports on the possibility of trapping cells, viruses, and bacteria using optical tweezers,[16,237] applications in the biological sciences have spurred. For example, optical tweezers have enabled the determination of the mechanical properties of cell membranes[238,239] and the manipulation of single chromosomes.[240,241] Moreover, optical tweezers have become one of the main tools of single-molecule force spectroscopy thanks to their ability to trap a wide range of different particles and molecules, which allows the study of a broad diversity of interactions in a variety of environments.[229,242−244] Notably, these tools have allowed the experimental determination of the Gibbs free energy profile of stretching processes in DNA molecules[245] and their relaxation times.[246] Interestingly, as shown in Figure 15b, similar platforms for force spectroscopy exploiting the DEP force have also been proposed.[228,247] Likewise, both low- and high-frequency fields have been applied to the study of molecular motors, as shown in Figure 16a. Trapping schemes with optical tweezers have allowed, among others,[248] the investigation of the kinesin stepping motion with nanometric precision,[249,250] while DEP forces have been used to sort, transport, and align actin filaments and microtubules.[22,23,251] Moreover, ROT setups have also been employed to characterize bacterial flagellar motors such as *Salmonella typhimurium*[252] and *Escherichia coli*[253] and molecular motors such as F_1-ATPase.[254−256]

As shown in Figure 16b, trapping applications in the field of micro- and nanofabrication also abound. For example, low-frequency fields have been used to trap metallic nanoparticles and carbon nanotubes for the fabrication of transistors,[221,259] atomic force microscope probes,[257] and ammonia sensors.[260] Similarly, high-frequency fields have been exploited to pattern particles and polymers on a substrate,[261−263] sometimes in combination with other fabrication methods such as two-photon polymerization (2PP).[258] As an example of an elegant combination of these two techniques, a screw-wrench microsystem has been realized with 2PP and effectively actuated using optical tweezers.[264] A related application is the fabrication and control of microfluidic components using optical tweezers.[265,266] Microfluidic pumps, in particular, have received exceptional attention and have been actuated either by exploiting the asymmetric light scattering of the pump[267,268] or the generation of spin[269] or orbital[270] torque on it. Low-frequency rotating fields have likewise been employed to pump and mix different fluids in lab-on-a-chip devices.[271] However, the major application of electrorotation has been the characterization of the dielectric properties of cells.[20] In these studies, one cell is usually placed at the center of a four electrode setup, such as the one shown in Figure 13a, either by exploiting the negative DEP force acting on it or by using an optical tweezer. The rotational speed of the cell is then

https://doi.org/10.1021/acs.chemrev.2c00576
Chem. Rev. 2023, 123, 1680−1711

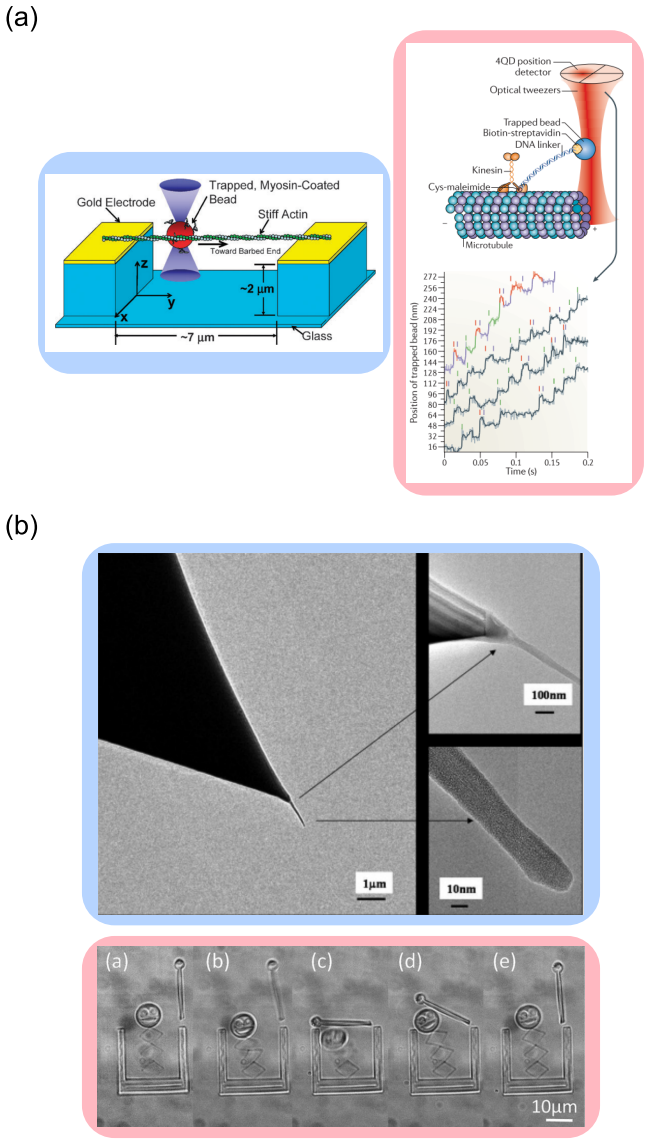

Figure 16. Analyte trapping with the use of intensity gradients. Panel (a) shows the use of trapping forces to study myosin (Reprinted with permission from ref 23. Copyright 2009 Royal Society of Chemistry) and kinesin molecular motors (Adapted with permission from ref 248. Copyright 2011 Springer Nature). Panel (b) shows, in blue, the fabrication of AFM probes using DEP forces (Reprinted with permission from ref 257. Copyright 2005 American Chemical Society) and, in pink, the fabrication and actuation of a Jack-in-the-box using optical tweezers (Reprinted with permission from ref 258. Copyright 2019 Royal Society of Chemistry).

measured as a function of the applied field frequency, which allows the extrapolation of important parameters, such as its membrane capacitance and its cytoplasm conductivity.[17,272] Moreover, applications in environmental monitoring[273,274] and neurosciences[275,276] have also started to develop recently. It is impossible to completely review all the applications of trapping with DEP and optical tweezers, but we hope that it is clear from our discussion how important these technologies are for controlling matter at the micro- and nanoscale. To this end, the creator of the optical tweezer Arthur Ashkin has been recently awarded the Nobel Prize in Physics in recognition of the role that this technology has played in the development of biological sciences.[277]

Aside from this more mature optical technology, plasmonic tweezers (see Figure 8d) have also emerged as an active and vibrant field of research in the past decade.[278] The trapping of nanoparticles and molecules has been demonstrated,[129,133,226,279−281] and a basic form of particle transport has also been realized by mounting these tweezers on the tip of an optical fiber.[282,283] Systems exhibiting SIBA have also been successfully employed as platforms for near field optical trapping with reduced laser power[6,82,83,284−286] and have been applied, among others, to the characterization of colloidal particles and molecules.[287,288] For example, such systems have allowed the determination of the molecular weight of globular proteins at the single-molecule level.[287]

Levitation schemes have also been conceived with both DEP and optical fields. However, despite their resemblance, they have been developed for different applications and exploit different physical interactions. In the low-frequency case, the main application has been the trapping of cells in the middle of microfluidic channels in order to avoid substrate interactions and facilitate transport.[289] As opposed to standard trapping, which usually occurs around the electrodes or the sidewalls of a microfluidic architecture, here, the negative intensity-based DEP force is used to balance the gravitational pull acting on the particle, thereby granting full control on the cell's distance above the substrate.[29] Similar schemes, which always employ the field gradient force, have also been devised to levitate gas bubbles and liquid droplets.[290,291] To the best of our knowledge, no DEP levitation schemes exploiting phase gradient forces have been proposed, and no DEP levitation experiments have been reported that were not conducted in water or some other liquid phase. A combination of intensity and scattering forces is instead used with optical fields to levitate and provide three-dimensional confinement of colloidal particles in air.[208,292,293] The optical intensity gradient force provides additional trapping and stability in the transverse direction, which produces a full 3D trap, as opposed to the DEP case. However, problems arise when trying to manipulate increasingly large particles, which cannot be levitated by single-beam optical tweezers since too much power would be required to counteract the growing weight. In such conditions, different trapping systems need to be devised, for example, by employing two counter-propagating beams that enable stable trapping outside the intensity hotspot.[294] After its first realization 50 years ago, optical levitation is now a common tool in the physical sciences, with a growing number of applications in metrology and quantum technologies.[295−301]

4.2. Assembly

The use of electromagnetic forces to assemble single particles into more complex structures exploits second-order particle−particle interactions whose detailed description is beyond the scope of this work. However, in view of the fundamentally important capabilities enabled by such assembly, we will outline the basic forces at play and give a brief applications overview in the low- and high-frequency regimes.

We consider here a system of two identical particles, A and B, under the action of an oscillating electric field, as previously defined. The polarizability $\alpha_{A,B}$ of one particle is induced by the total field at the particle's location, which is now composed of the incident field at that location, $\mathbf{E}_{A,B}$, plus the perturbation induced by the other particle $\hat{\mathbf{E}}_{B,A}$. By taking these additional contributions into account, the total force acting on particle A in the dipolar approximation can be written as[302]

https://doi.org/10.1021/acs.chemrev.2c00576
Chem. Rev. 2023, 123, 1680−1711

$$\langle \mathbf{F}_A \rangle = \frac{1}{2}\Re(\alpha_A \mathbf{E}_A \nabla \mathbf{E}_A^* + \alpha_A \hat{\mathbf{E}}_B \nabla \mathbf{E}_A^* + \alpha_A \mathbf{E}_A \nabla \hat{\mathbf{E}}_B^*) \quad (48)$$

where the first term is just the force defined in eq 13 for isolated particles, while the other two stem from mutual particle−particle interactions. In particular, the second term represents the force generated by the coupling of the incident field $\mathbf{E}_A$ to the polarization of particle A generated by the scattered field $\hat{\mathbf{E}}_B$ from particle B. Similarly, the last term accounts for the force generated by the interaction of the polarization of particle A generated by the incident field $\mathbf{E}_A$ with the scattered field $\hat{\mathbf{E}}_B$ generated by particle B. A similar equation can be written for the force acting on particle B. Depending on the value of the interparticle distance R, two different regimes can be identified: $kR < 1$ or $kR > 1$. These are called, respectively, the *near field* and *far field* regimes[302] and are described in Figure 17. For $kR < 1$, we note that, as long as K has the same sign for both particles, the force is always attractive in Figure 17a and repulsive in Figure 17b.[29,302] In this near field regime, which is the only one accessible when working with RF fields, the dipolar approximation used here can fail for small R (less than the particle's radius r) and high K (metallic particles), where higher multipolar orders come into play.[29,303] Moreover, the strong field between the particles can induce a change in their polarizations, which can increase or decrease depending on the applied frequency and number of particles assembled.[29,44] In the far-field regime, accessible only with optical fields, the binding force can be either positive or negative depending on R.[306] This behavior results from the different phases that the radiated field from particle A (B) takes up with respect to the incident field at the location of particle B (A). As a consequence, there exist several values of R that give rise to stable configurations where the binding force vanishes, which are separated by roughly λ in the case shown in Figure 17a and $\lambda/2$ in Figure 17b.[302] The theory presented here can be easily extended to consider the case of heterodimers or of more than two particles.[29,302]

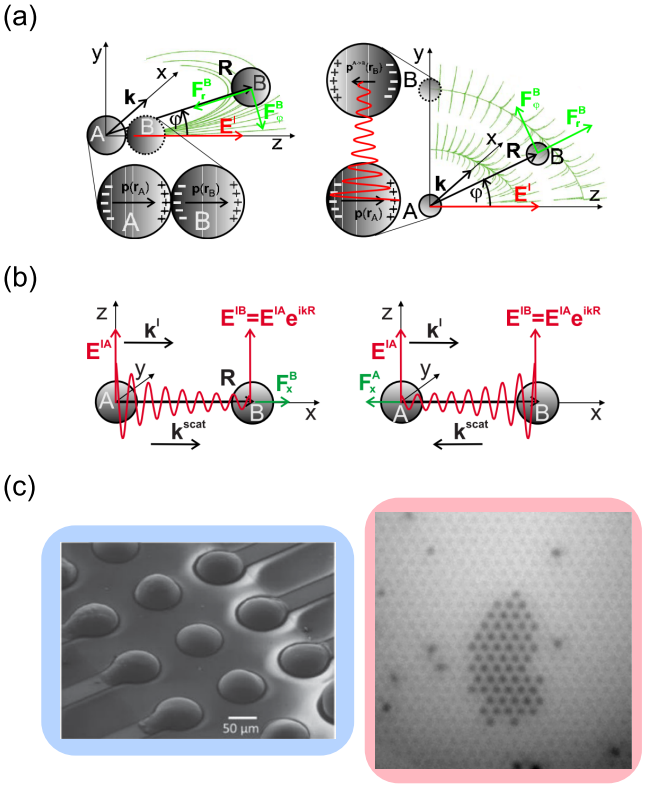

Figure 17. Electromagnetic binding. (a,b) Binding forces acting on a particle dimer excited with a plane wave propagating along $\mathbf{k} = (k, 0, 0)$ and polarized along $\mathbf{E}^I = (0, 0, E^I)$ (Reprinted with permission from ref 302. Copyright 2010 American Physical Society). The near field case is shown on the left, while the far-field interaction is shown on the right. Panel (a) depicts the case where $\mathbf{R} = [0, R\sin(\varphi), R\cos(\varphi)]$ is perpendicular to $\mathbf{k}$, and the green lines follow the trajectories of particle B toward its equilibrium position, as denoted by dotted edges. Panel (b) shows the case where $\mathbf{R} = (R, 0, 0)$ is parallel to $\mathbf{k}$. (c) On the left are 3D metallic electrodes fabricated by assembling and welding multiple Galinstan droplets through dielectrophoresis (Adapted with permission from ref 304. Copyright 2015 Wiley). On the right is a 2D crystal of gold nanoparticles assembled through optical binding (Reprinted with permission from ref 305. Copyright 2015 American Chemical Society).

From a practical perspective, applications of the binding force abound in the literature. For example, using low-frequency fields, this binding interaction has been exploited to direct the assembly of complex structures, such as pearl chains,[307−310] and has also allowed the manipulation of carbon nanotubes and welding of nanoparticles for electronics applications.[221,311−314] As shown in the blue panel of Figure 17c, 3D electrodes have been fabricated by exploiting low-frequency assembly forces to merge multiple liquid-metal droplets, thereby enabling the creation of microfluidic chips with enhanced DEP trapping and heat dissipation capabilities.[304]

For what concerns the high-frequency regime, optical binding was first demonstrated with Mie particles[315] and has since then developed into a very active research field, with nanoscale applications with Rayleigh particles becoming increasingly more common.[136,302] As a few examples, we can cite the realization of particle chains and arrays[316−318] for applications, among others, in optical printing.[319] Optical binding forces have also been used to control the epitaxial growth of gold nanoparticles to realize two-dimensional particle crystals,[305] as shown in the pink panel of Figure 17c. Furthermore, the possibility to tailor the particle interaction with structured light[320] or by exploiting plasmonic[321] and substrate[75] effects has also been shown. Repulsive optical binding forces have also been predicted theoretically but have yet to be observed experimentally.[71,322,323] Interestingly, phase gradients have also been shown to control the optical binding force,[324−326] while to the best of our knowledge, particle assembly driven by the phase gradient of low-frequency fields has not been reported in the literature.

4.3. Transport

The last application of interest is particle transport along predetermined patterns, which allows the particle to move to different parts of the device where subsequent tasks (functionalization, sensing, assembly) can be performed. This requires the generation of tailored intensity and/or phase gradient forces that can move the particle in the desired direction. We first point out that particle manipulation with optical fields has received more attention than that with low-frequency fields, and consequently, optical techniques are now more widely adopted for particle actuation. This difference stems from technological difficulties in fabricating moving DEP probes or multiple electrodes for TWDEP setups. However, the phase gradient naturally embedded in a propagating laser

https://doi.org/10.1021/acs.chemrev.2c00576
Chem. Rev. 2023, 123, 1680−1711

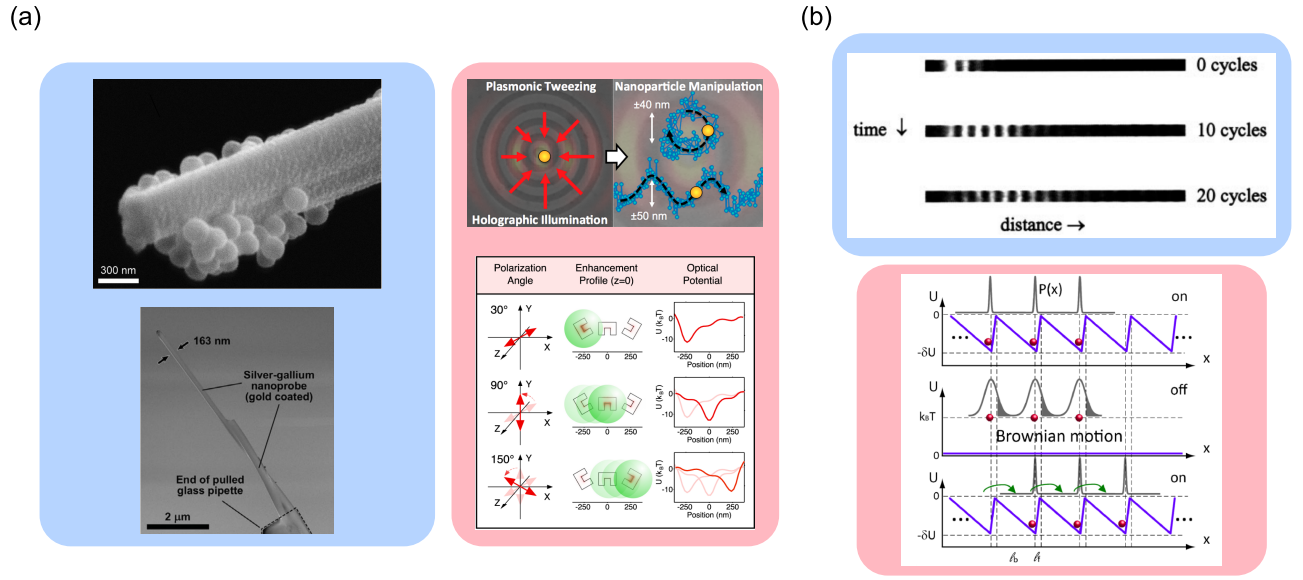

Figure 18. Analyte transport with the use of intensity gradients. Panel (a) shows particle manipulation, in blue, by utilizing a DEP probe (Reprinted with permission from ref 163. Copyright 2013 Wiley) and, in red, by moving a plasmonic hotspot in space (Reprinted with permission from ref 154. Copyright 2017 American Chemical Society) or by exploiting polarization effects on a metasurface (Reprinted with permission from ref 334. Copyright 2014 American Chemical Society). The top figure in Panel (b) shows the working principle of a Brownian ratchet (Reprinted with permission from ref 337. Copyright 2016 American Chemical Society), while the bottom one shows its application to the transport of DNA molecules (Reprinted with permission from ref 338. Copyright 1999 The National Academy of Sciences).

beam can be straightforwardly used for particle transport without needing any additional micro-/nanofabrication processes. As a consequence, the field of optical manipulation has grown significantly over the past years, and we address the interested reader to the relevant literature.[211,327] In the following, we will outline some of the main strategies for optical analyte transport and compare them to the state-of-the-art methods realized with low-frequency fields by employing both intensity and phase gradient forces.

To this end, the field intensity hotspots generated in common optical and DEP setups are usually static, i.e., are fixed in space; therefore, the trapped analyte cannot be easily moved to a different location. As a consequence, particular strategies need to be devised to dynamically move a field intensity hotspot in space. For instance, it is possible to employ an electrokinetic probe—such as the one shown in Figure 18a—as a DEP electrode. This way, once the particle of interest is trapped at the tip of the probe thanks to a positive DEP force, the electrode can be moved and transport the particle with it.[15,163,328,329] Similarly, the position of the focal point of an optical tweezer can be manipulated by either introducing additional optical components in the optical path of the beam (e.g., lenses or SLMs[330]) or by mechanically moving the objective or the sample stage.[16,331] Alternatively, by dynamically controlling the positions of the antinodes of a standing wave, particles trapped at these positions can also be easily transported along the wave.[332] Similarly, in near field traps, the trapping hotspot resulting from the interference of counterpropagating plasmonic waves can also be manipulated by tailoring the intensity[333] and spatial profile[154] of the incoming beam, as shown in Figure 18a. Besides this, localized plasmonic resonances can also be exploited when transporting a particle over a substrate patterned with several metallic nanostructures. In such a configuration, these structures create multiple trapping hotspots when illuminated by suitable optical radiation, and a particle can be transported from one intensity hotspot to the adjacent one by tuning the polarization[109,334,335] or the wavelength[336] of the incoming field, therefore allowing full 2D analyte manipulation.

Unfortunately, all the strategies presented so far always require continuous operator supervision and visual feedback to properly tailor the excitation field and/or direct the DEP tweezer, and therefore do not allow a full automated transport of the trapped analyte. One way to circumvent this limitation is to fabricate an array of structures, such as plasmonic nanostructures or DEP electrodes, with an asymmetric trapping potential in order to realize Brownian motors.[339] The working principle is relatively simple and is explained in Figure 18b. After trapping the analytes of interest in a field maximum, the field is turned off and the particles freely diffuse because of Brownian motion. As a result of the potential asymmetry, they will be statistically more likely to diffuse in the trapping well of the adjacent (on the right side in Figure 18b) hotspot when the field is turned on again, thereby leading to a net movement in one direction. This transport configuration has been successfully realized both with optical[337,340] and DEP fields[338,341] for the manipulation of particles and biomolecules. Unfortunately, the stochastic nature of the diffusion process makes this approach far from deterministic and, as a consequence, this technique lacks the degree of control and precision required for nanoscale manipulation.

While the manipulation of objects with intensity gradients requires the manual adjustment of the spatial position of the intensity hotspot, phase gradients usually exploit the natural phase profile of a propagating electromagnetic field. For such a wave, be that of a laser or a low-frequency field in a TWDEP setup, the phase linearly increases from 0 to 2π over a wavelength in such a way that a particle with $\alpha'' > 0$ is pushed by the wave along its propagation direction, while an object having $\alpha'' < 0$ is pulled against the wave, as predicted by eq 24. This effect has been demonstrated with low-frequency fields where yeast cells of *Saccharomyces cerevisiae* have been

https://doi.org/10.1021/acs.chemrev.2c00576
Chem. Rev. 2023, 123, 1680−1711

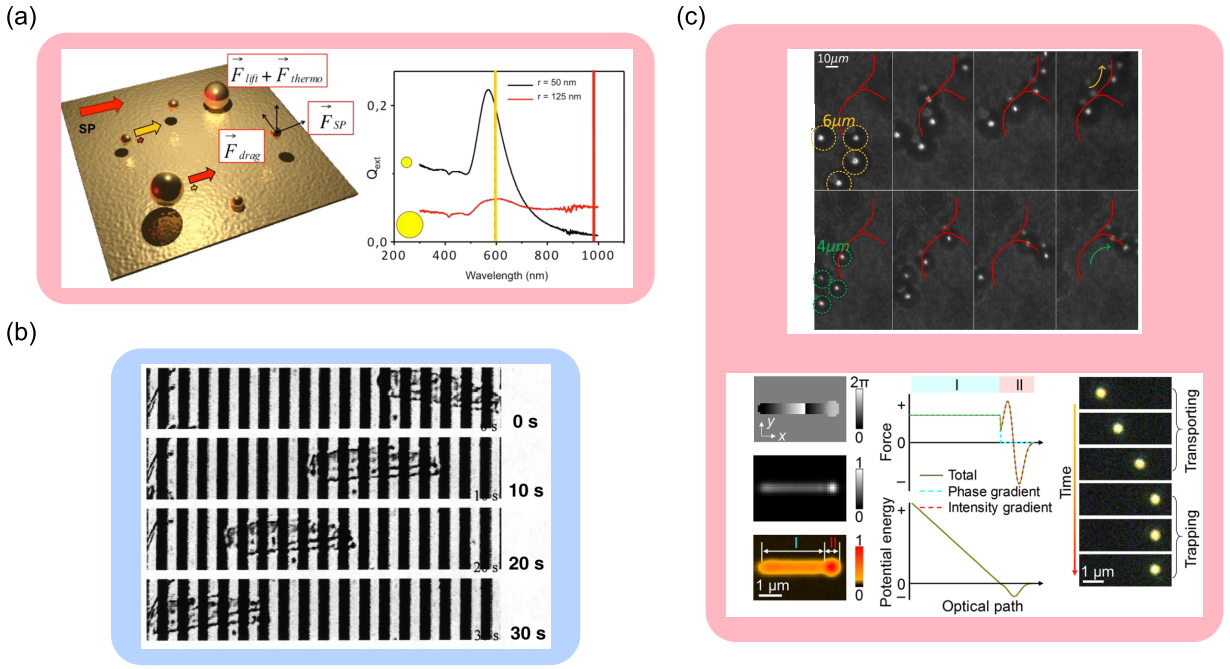

Figure 19. Strategies for analyte transport and sorting by exploiting phase gradients. (a) Exploitation of propagating plasmonic modes for particle transport (Reprinted with permission from ref 346. Copyright 2013 American Chemical Society). (b) TWDEP electrodes for cells and particles actuation (Reprinted with permission from ref 289. Copyright 2001 Wiley). (c) From top to bottom, the panel shows the use of SLMs for particle sorting (Adapted with permission from ref 347. Copyright 2021 AIP Publishing) and manipulation (Adapted with permission from ref 14. Copyright 2020 American Chemical Society).

observed to travel against a propagating RF field.[342] However, this "pulling" force on gain media particles has only been theoretically investigated at high frequencies[32,343] but, to the best of our knowledge, not realized experimentally. However, the use of different illumination conditions from the standard plane wave has allowed the full control of a particle's motion along and against the optical beam[32,168,169]—with the use of so-called *tractor beams*—with similar studies now also being conducted for near field plasmonic systems.[344] To this end, the exploitation of propagating plasmonic modes seems a promising strategy to employ for the manipulation of analytes,[345] for example, in the experimental configuration presented in Figure 9c. As depicted in Figure 19a, these setups have, for instance, been used to sort gold nanoparticles of different sizes by exploiting the different coupling between their localized plasmonic resonances and a propagating plasmonic mode in the underlying metallic substrate.[346] Similarly, TWDEP setups have, for example, been used to separate rabbit heart cells from latex beads (black dot in the blue panel of Figure 19b) through their different travel velocities.[289]

Aside from separately using intensity and phase gradients for analyte transport, a number of works have also proposed their combined use in optical setups to achieve full control of single particles.[14,347−349] Here, as shown in Figure 19c, intensity gradients are used to confine the analyte along a predefined pattern while phase gradients are then employed to move the object inside it. This way, a synergy of intensity and phase forces is used to trap and transport particles and provide a higher degree of control over the trapped analyte. For example, as shown in Figure 19c, this configuration has allowed the sorting of microparticles by automatically directing particles of different sizes along different paths by exploiting their different interactions with phase gradient forces.[347] We note that this combination of phase transport lines with intensity traps does not seem to have been proposed for DEP fields, but it would, in principle, be possible, for instance, by exploiting the different electrokinetic behaviors of cells as a function of the frequency of the applied DEP field.[342]

5. OUTLOOK

Field−matter interactions play a fundamental role in today's push toward the realization of always more versatile and accurate tools to study and manipulate matter at the micro- and nanoscales. Rather than just exploiting mere electrostatic interactions, multipolar forces stem from spatial inhomogeneities of the field intensity or phase, which also allows the manipulation of neutral particles and the exploitation of the frequency-dependent properties of the induced polarization. Our treatment has demonstrated that, regardless of the frequency chosen for the field, the physical principles behind the generation of these forces are always the same, i.e., the creation of induced multipoles inside the particle and their interaction with an inhomogeneous field. The main difference between the two frequency regimes analyzed here lies in the dominant loss mechanism in each case: conduction losses dominate for RF excitations, while dielectric losses prevail for optical fields. This can lead to very different values for the induced polarization in the particle but it does not change the underlying physics.

From a historical perspective, the term dielectrophoresis was coined as early as 1951 by Pohl,[350] while the first unified treatment of both intensity and phase gradient DEP was developed in 1993 by Pethig and collaborators.[342] It is interesting to note how the first DEP experiments of Pohl took place roughly a decade before the invention of the laser in 1960, a milestone of modern optical technology and a basic requirement for the experimental observation of optical

https://doi.org/10.1021/acs.chemrev.2c00576
Chem. Rev. 2023, 123, 1680−1711

intensity and phase gradient forces, which indeed followed shortly after.[51,351] However, a unified theory of optical forces was developed only in the early 2000s, with little or no attention paid to the very similar results that had already been published in the DEP literature. Maybe as a consequence of this, the terminology and notation used to express the optical force are usually different from those used for DEP: one would rather speak of scattering force or radiation pressure than of phase gradient force. Consequently, the potential of optical phase gradient manipulation has yet to be fully unlocked even though it is an acknowledged and well-recognized feature of DEP. Similarly, the generation of negative DEP forces is a well-known feature of the theory, while the idea of negative optical forces still surprises many of those working in the optical community.

From the experimental side, DEP has been mainly confined to lab-on-a-chip devices for analyses and quantification of biological samples, while optical tweezers have found a much wider range of applications. For example, when compared with RF fields, working at optical frequencies permits the exploitation of resonant effects in plasmonic particles, optical cavities, and two-level atomic systems. Furthermore, the use of SLMs to produce structured beams with unusual intensity and phase gradient distributions adds to the number of degrees of freedom in an optical experiment, thereby making this technique a much more versatile choice than DEP. Conversely, RF fields can be engineered to be more intense than their optical counterpart. This results in stronger DEP forces that are better suited to work with very diluted samples, for example, for quick analyses in biomedical research laboratories. To this end, DEP chips seem to provide a better platform to support the current trend of miniaturization for portable point-of-care devices thanks to the more advanced status of nanoelectronic fabrication techniques compared with nanophotonic technologies.

Besides this, we strongly believe that the field of nanoscale analyte manipulation will greatly benefit from combining both low- and high-frequency fields into a single device that can exploit electromagnetic interactions in both frequency regimes. For example, while low-frequency forces tend to be stronger than their high-frequency counterparts and, therefore, provide a better trapping efficiency, optical interactions are usually better suited to characterize the trapped analyte. As a consequence, lab-on-a-chip devices able to work in both frequency regimes promise to deliver superior trapping and sensing capabilities than current biosensors. Alternatively, by exploiting the phase-shaping properties of SLMs, optical phase gradients could be integrated into DEP devices to achieve a combined DEP intensity and optical phase manipulation of nanoscale analytes. On the technological side, a full integration of DEP and optical technologies will require the downscaling of DEP devices to match the submicron size of typical photonic components or, alternatively, an upscaling of optical components to sizes comparable with the typical wavelengths of RF fields. To this end, the downscaling of DEP components—to create, for example, plasmonic nanoelectrodes[142]—seems to be in a more mature stage than the upscaling of photonic devices. In this work, we greatly referred to the amazing light-shaping properties of SLMs. Upscaling this technology to impart arbitrary intensity and phase profiles to RF fields would represent a tremendous achievement for the DEP community. Such a device, which we could call a spatial radiation modulator (SRM), would bring about a revolution in our low-frequency manipulation capabilities, while a combination of SLMs and SRMs could really unlock a completely new paradigm in the way we interact with nanoscale matter. Unfortunately, this technology is not yet available, but we hope that this work will stimulate fruitful thinking into future lines of research that cross-fertilize low- and high-frequency electromagnetic interactions.

AUTHOR INFORMATION

Corresponding Author

Olivier J. F. Martin − *Nanophotonics and Metrology Laboratory, Swiss Federal Institute of Technology Lausanne (EPFL), EPFL-STI-NAM, CH-1015 Lausanne, Switzerland;* orcid.org/0000-0002-9574-3119; Email: olivier.martin@epfl.ch

Author

Marco Riccardi − *Nanophotonics and Metrology Laboratory, Swiss Federal Institute of Technology Lausanne (EPFL), EPFL-STI-NAM, CH-1015 Lausanne, Switzerland;* orcid.org/0000-0001-8260-581X

Complete contact information is available at: https://pubs.acs.org/10.1021/acs.chemrev.2c00576

Author Contributions

CRediT: **Marco Riccardi** conceptualization, data curation, formal analysis, investigation, methodology, resources, software, visualization, writing-original draft; **Olivier J.F. Martin** conceptualization, funding acquisition, methodology, project administration, resources, supervision, validation, writing-review & editing.

Notes

The authors declare no competing financial interest.

Biographies

Marco Riccardi has received a Laurea in Physics and a Master of Research in Nanomaterials degree from the Università degli Studi di Torino and Imperial College London, respectively. He carried out his Ph.D. in Photonics under the supervision of Prof. Olivier J. F. Martin at the École polytechnique fédérale de Lausanne, where he is now a postdoctoral investigator. His research interests span nanotechnology as a whole, with a particular emphasis on the development of novel devices for analyte manipulation and quantum sensing.

Olivier J. F. Martin is Full Professor of Nanophotonics and Optical Signal Processing at the Swiss Federal Institute of Technology Lausanne (EPFL), where he conducts comprehensive research that combines the development of numerical techniques for the solution of Maxwell's equations with advanced nanofabrication and experiments on plasmonic systems. Applications of his research include optical antennas, metasurfaces, nonlinear optics, optical nanomanipulations, heterogeneous catalysis, and security features.

ACKNOWLEDGMENTS

The authors gratefully acknowledge funding from the European Research Council (ERC-2015-AdG-695206 Nanofactory).

ADDITIONAL NOTES

[1]Despite not being strictly a multipole, the monopole can be considered as the zero-th order multipole. Equivalently, the zero-th order field derivative is just $\mathbf{E}_t$.

https://doi.org/10.1021/acs.chemrev.2c00576
Chem. Rev. 2023, 123, 1680−1711

[2]We warn that the majority of the literature concerned with low-frequency fields instead assumes a harmonic excitation with the other sign, $\mathbf{E}(\mathbf{r}, \omega) = \Re[\mathbf{E}(\mathbf{r})e^{i\omega t}]$. This is just a different convention that leads to the same description of the system.

[3]As a consequence, $\mathbf{E}_0$ retains a complex value, even for $\phi = 0$ and $\omega = 0$. This is needed in order to model polarization inhomogeneities that give rise to electromagnetic torques.

[4]With $(2n-1)!! = (2n-1)(2n-3)...5 \times 3 \times 1$. Analogous expressions can also be written for nonspherical particles.[33] Moreover, ∇^n represents the n^{th} order derivative.

[5]The center of the particle is placed in $\mathbf{r}_0 = 0$, while $\mathbf{r}$ is the position vector of a point belonging to ∂V. We show, here, only the series for the electric field; an analogous one can be written for $\mathbf{H}_t$.

[6]This simplification leads to exact results when considering the time-averaged force for $n = 1$ but breaks down for higher orders when magnetic effects also start to play a role.[37]

[7]Dielectric particles have few bulk conduction charges but, when dispersed into a liquid, build up an electrical double layer (EDL) of surface ions, and as a consequence, the particle acquires some surface conduction charges.[43]

[8]$\sigma_{p,m}(\omega) = \sigma'_{p,m} + i\sigma''_{p,m}$ is the complex valued conductivity, while $\epsilon^d_{p,m}$ and $\sigma_{p,m}/\omega$ are, respectively, the frequency-dependent dielectric and conductive loss terms.

[9]The phase gradient force, even though it can be expressed as a gradient of the scalar field ϕ, is generally not conservative because of the Doppler effect.[36]

[10]Recently, a computational toolbox for the determination of the Clausius−Mossotti factor for shell particles and cells has also been developed.[60]

[11]The DC polarizability of eq 6 for $n = 1$ is used because radiative corrections can still be neglected at the low frequencies considered in this section.

[12]Because we are considering here RF frequencies, dielectric losses do not play a role yet, and the particle can be considered lossless.

[13]We need to recognize that $\phi = \mathbf{k} \cdot \mathbf{r}$, in such a way that $\mathbf{k} = \nabla\phi$ with $|\mathbf{k}| = 2\pi/\lambda$, where λ is the wavelength.

[14]This holds in the case of small or slowly varying $\epsilon^d_{p,m}$ around the particle's resonant frequency.[78,79]

[15]In this configuration, the third component of the dipolar force in eq 28 is also necessary for a full description of the system.[66]

[16]Interestingly, intensity-based DEP can be seen as a special case of TWDEP where the two electrodes are excited with voltages that have the same frequency and phases of 0 and π, respectively, thus generating a standing wave.[147]

[17]Furthermore, when working with apertures milled in a metallic substrate, this acts as a heat sink and greatly reduces the local temperature increase around the structures to only a few degrees Celsius.[159] However, if needed, these substrates can also be properly engineered to act as efficient light-to-heat conversion systems.[160,161] In DEP experiments, while thermal effects generated by Joule and dielectric losses can significantly alter the local temperature around the metallic electrodes[162]—as well as in iDEP devices[118]—the temperature increase is usually reduced to only a few degrees Celsius when employing AC voltages with amplitudes smaller than 10 V.[15,163,164]

[18]The opposite happens for a left circularly polarized field $\mathbf{E}_0(\mathbf{r}) = \mathbf{E}'_0(\mathbf{x} + i\mathbf{y})$, which induces a torque $\langle\boldsymbol{\tau}_S\rangle = \alpha''|\mathbf{E}'_0|^2\mathbf{z}$.[178]

[19]Here, the off-diagonal terms are set to zero, which indicates that the particle axes correspond to the principal (crystalline) axes of the material. However, this is, in general, not true.

REFERENCES

(1) Geiger, M.; Hogerton, A. L.; Bowser, M. T. Capillary Electrophoresis. *Anal. Chem.* **2012**, *84*, 577−596.

(2) Kristoff, C. J.; Bwanali, L.; Veltri, L. M.; Gautam, G. P.; Rutto, P. K.; Newton, E. O.; Holland, L. A. Challenging Bioanalyses with Capillary Electrophoresis. *Anal. Chem.* **2020**, *92*, 49−66.

(3) Kepler, J.*De Cometis Libelli Tres*; Andrae Apergeri: Augsburg, 1619.

(4) Chu, S.; Bjorkholm, J. E.; Ashkin, A.; Cable, A. Experimental Observation of Optically Trapped Atoms. *Phys. Rev. Lett.* **1986**, *57*, 314−317.

(5) Phillips, W. D. Nobel Lecture: Laser Cooling and Trapping of Neutral Atoms. *Rev. Mod. Phys.* **1998**, *70*, 721−741.

(6) Pang, Y.; Gordon, R. Optical Trapping of a Single Protein. *Nano Lett.* **2012**, *12*, 402−406.

(7) Lesser-Rojas, L.; Ebbinghaus, P.; Vasan, G.; Chu, M.-L.; Erbe, A.; Chou, C.-F. Low-Copy Number Protein Detection by Electrode Nanogap-Enabled Dielectrophoretic Trapping for Surface-Enhanced Raman Spectroscopy and Electronic Measurements. *Nano Lett.* **2014**, *14*, 2242−2250.

(8) Taylor, A. B.; Zijlstra, P. Single-Molecule Plasmon Sensing: Current Status and Future Prospects. *ACS Sensors* **2017**, *2*, 1103−1122.

(9) Trepagnier, E. H.; Radenovic, A.; Sivak, D.; Geissler, P.; Liphardt, J. Controlling DNA Capture and Propagation through Artificial Nanopores. *Nano Lett.* **2007**, *7*, 2824−2830.

(10) Heller, I.; Hoekstra, T. P.; King, G. A.; Peterman, E. J. G.; Wuite, G. J. L. Optical Tweezers Analysis of DNA−Protein Complexes. *Chem. Rev.* **2014**, *114*, 3087−3119.

(11) Jose, J.; Kress, S.; Barik, A.; Otto, L. M.; Shaver, J.; Johnson, T. W.; Lapin, Z. J.; Bharadwaj, P.; Novotny, L.; Oh, S.-H. Individual Template-Stripped Conductive Gold Pyramids for Tip-Enhanced Dielectrophoresis. *ACS Photonics* **2014**, *1*, 464−470.

(12) Freedman, K. J.; Crick, C. R.; Albella, P.; Barik, A.; Ivanov, A. P.; Maier, S. A.; Oh, S.-H.; Edel, J. B. On-Demand Surface- and Tip-Enhanced Raman Spectroscopy Using Dielectrophoretic Trapping and Nanopore Sensing. *ACS Photonics* **2016**, *3*, 1036−1044.

(13) Spesyvtseva, S. E. S.; Dholakia, K. Trapping in a Material World. *ACS Photonics* **2016**, *3*, 719−736.

(14) Nan, F.; Yan, Z. Optical Sorting at the Single-Particle Level with Single-Nanometer Precision Using Coordinated Intensity and Phase Gradient Forces. *ACS Nano* **2020**, *14*, 7602−7609.

(15) Nadappuram, B. P.; Cadinu, P.; Barik, A.; Ainscough, A. J.; Devine, M. J.; Kang, M.; Gonzalez-Garcia, J.; Kittler, J. T.; Willison, K. R.; Vilar, R.; et al. Nanoscale Tweezers for Single-Cell Biopsies. *Nat. Nanotechnol.* **2019**, *14*, 80−88.

(16) Ashkin, A.; Dziedzic, J. M.; Yamane, T. Optical Trapping and Manipulation of Single Cells Using Infrared Laser Beams. *Nature* **1987**, *330*, 769−771.

(17) Becker, F. F.; Wang, X.-B.; Huang, Y.; Pethig, R.; Vykoukal, J.; Gascoyne, P. R. C. Separation of Human Breast Cancer Cells from Blood by Differential Dielectric Affinity. *Proc. Natl. Acad. Sci. U. S. A.* **1995**, *92*, 860−864.

(18) Bhatt, K. H.; Grego, S.; Velev, O. D. An AC Electrokinetic Technique for Collection and Concentration of Particles and Cells on Patterned Electrodes. *Langmuir* **2005**, *21*, 6603−6612.

(19) Nakano, A.; Ros, A. Protein Dielectrophoresis: Advances, Challenges, and Applications. *Electrophoresis* **2013**, *34*, 1085−1096.

(20) Zheng, Y.; Nguyen, J.; Wei, Y.; Sun, Y. Recent Advances in Microfluidic Techniques for Single-Cell Biophysical Characterization. *Lab Chip* **2013**, *13*, 2464−2483.

(21) Mejía-Salazar, J. R.; Oliveira, O. N. J. Plasmonic Biosensing. *Chem. Rev.* **2018**, *118*, 10617−10625.

https://doi.org/10.1021/acs.chemrev.2c00576
Chem. Rev. 2023, 123, 1680−1711

(22) Asokan, S. B.; Jawerth, L.; Carroll, R. L.; Cheney, R. E.; Washburn, S.; Superfine, R. Two-Dimensional Manipulation and Orientation of ActinMyosin Systems with Dielectrophoresis. *Nano Lett.* **2003**, *3*, 431−437.
(23) Arsenault, M. E.; Sun, Y.; Bau, H. H.; Goldman, Y. E. Using Electrical and Optical Tweezers to Facilitate Studies of Molecular Motors. *Phys. Chem. Chem. Phys.* **2009**, *11*, 4834−4839.
(24) MacDonald, M. P.; Spalding, G. C.; Dholakia, K. Microfluidic Sorting in an Optical Lattice. *Nature* **2003**, *426*, 421−424.
(25) Regtmeier, J.; Eichhorn, R.; Viefhues, M.; Bogunovic, L.; Anselmetti, D. Electrodeless Dielectrophoresis for Bioanalysis: Theory, Devices and Applications. *Electrophoresis* **2011**, *32*, 2253−2273.
(26) Baker, D.; Sali, A. Protein Structure Prediction and Structural Genomics. *Science (80-.)* **2001**, *294*, 93−96.
(27) Frigault, M. M.; Lacoste, J.; Swift, J. L.; Brown, C. M. Live-Cell Microscopy − Tips and Tools. *J. Cell Sci.* **2009**, *122*, 753−767.
(28) Qin, M.; Zhang, L.; Wu, H. Dielectric Loss Mechanism in Electromagnetic Wave Absorbing Materials. *Adv. Sci.* **2022**, *9*, 2105553.
(29) Jones, T. B.*Electromechanics of Particles*, 1st ed.; Cambridge University Press, 1995.
(30) Jones, T.; Washizu, M. Multipolar Dielectrophoretic and Electrorotation Theory. *J. Electrostat.* **1996**, *37*, 121−134.
(31) Washizu, M. Equivalent Multipole-Moment Theory for Dielectrophoresis and Electrorotation in Electromagnetic Field. *J. Electrostat.* **2004**, *62*, 15−33.
(32) Chen, J.; Ng, J.; Lin, Z.; Chan, C. T. Optical Pulling Force. *Nat. Photonics* **2011**, *5*, 531−534.
(33) Green, N. G.; Jones, T. B. Numerical Determination of the Effective Moments of Non-Spherical Particles. *J. Phys. D. Appl. Phys.* **2007**, *40*, 78−85.
(34) Draine, B. T. The Discrete-Dipole Approximation and its Application to Interstellar Graphite Grains. *Astrophys. J.* **1988**, *333*, 848.
(35) Wang, X.; Wang, X.-B.; Gascoyne, P. R. General Expressions for Dielectrophoretic Force and Electrorotational Torque Derived Using the Maxwell Stress Tensor Method. *J. Electrostat.* **1997**, *39*, 277−295.
(36) Novotny, L.; Hecht, B.*Principles of Nano-Optics*, 2nd ed.; Cambridge University Press, 2012.
(37) Jiang, Y.; Ng, J.; Lin, Z.Ab Initio Derivation of Multipolar Expansion of Optical Force. *arXiv*, December, 10, 2016, 1512.00420, ver. 2..
(38) Burt, J. P. H.; Al-Ameen, T. A. K.; Pethig, R. An Optical Dielectrophoresis Spectrometer for Low-Frequency Measurements on Colloidal Suspensions. *J. Phys. E* **1989**, *22*, 952−957.
(39) Wong, P.; Wang, T.-H.; Deval, J.; Ho, C.-M. Electrokinetics in Micro Devices for Biotechnology Applications. *IEEE/ASME Trans. Mechatronics* **2004**, *9*, 366−376.
(40) Velev, O. D.; Bhatt, K. H. On-Chip Micromanipulation and Assembly of Colloidal Particles by Electric Fields. *Soft Matter* **2006**, *2*, 738.
(41) Riccardi, M.; Kiselev, A.; Achouri, K.; Martin, O. J. F. Multipolar Expansions for Scattering and Optical Force Calculations Beyond the Long Wavelength Approximation. *Phys. Rev. B* **2022**, *106*, 115428.
(42) Arias-González, J. R.; Nieto-Vesperinas, M. Optical Forces on Small Particles: Attractive and Repulsive Nature and Plasmon-Resonance Conditions. *J. Opt. Soc. Am. A* **2003**, *20*, 1201.
(43) Parsons, R. The Electrical Double Layer: Recent Experimental and Theoretical Developments. *Chem. Rev.* **1990**, *90*, 813−826.
(44) Pethig, R. Review Article—Dielectrophoresis: Status of the Theory, Technology, and Applications. *Biomicrofluidics* **2010**, *4*, 022811.
(45) Jones, T. Dielectrophoretic Force Calculation. *J. Electrostat.* **1979**, *6*, 69−82.
(46) Arcenegui, J. J.; García-Sánchez, P.; Morgan, H.; Ramos, A. Electro-Orientation and Electrorotation of Metal Nanowires. *Phys. Rev. E* **2013**, *88*, 063018.
(47) Ramos, A.; García-Sánchez, P.; Morgan, H. AC Electrokinetics of Conducting Microparticles: A Review. *Curr. Opin. Colloid Interface Sci.* **2016**, *24*, 79−90.
(48) Seyedi, S. S.; Matyushov, D. V. Protein Dielectrophoresis in Solution. *J. Phys. Chem. B* **2018**, *122*, 9119−9127.
(49) Hölzel, R.; Pethig, R. Protein Dielectrophoresis: I. Status of Experiments and an Empirical Theory. *Micromachines* **2020**, *11*, 533.
(50) Ashkin, A.; Gordon, J. P. Stability of Radiation-Pressure Particle Traps: An Optical Earnshaw Theorem. *Opt. Lett.* **1983**, *8*, 511−513.
(51) Ashkin, A.; Dziedzic, J. M.; Bjorkholm, J. E.; Chu, S. Observation of a Single-Beam Gradient Force Optical Trap for Dielectric Particles. *Opt. Lett.* **1986**, *11*, 288−290.
(52) Jones, P. H.; Maragò, O. M.; Volpe, G.*Optical Tweezers*, 1st ed.; Cambridge University Press, 2015.
(53) Gascoyne, P. R. C.; Vykoukal, J. Particle Separation by Dielectrophoresis. *Electrophoresis* **2002**, *23*, 1973−1983.
(54) Hughes, M. P.; Morgan, H.; Flynn, M. F. The Dielectrophoretic Behavior of Submicron Latex Spheres: Influence of Surface Conductance. *J. Colloid Interface Sci.* **1999**, *220*, 454−457.
(55) Zhang, C.; Khoshmanesh, K.; Mitchell, A.; Kalantar-zadeh, K. Dielectrophoresis for Manipulation of Micro/Nano Particles in Microfluidic Systems. *Anal. Bioanal. Chem.* **2010**, *396*, 401−420.
(56) Green, N. G.; Morgan, H. Dielectrophoresis of Submicrometer Latex Spheres. 1. Experimental Results. *J. Phys. Chem. B* **1999**, *103*, 41−50.
(57) Ermolina, I.; Morgan, H. The Electrokinetic Properties of Latex Particles: Comparison of Electrophoresis and Dielectrophoresis. *J. Colloid Interface Sci.* **2005**, *285*, 419−428.
(58) Honegger, T.; Berton, K.; Picard, E.; Peyrade, D. Determination of Clausius−Mossotti Factors and Surface Capacitances for Colloidal Particles. *Appl. Phys. Lett.* **2011**, *98*, 181906.
(59) Clarke, R. W.; Piper, J. D.; Ying, L.; Klenerman, D. Surface Conductivity of Biological Macromolecules Measured by Nanopipette Dielectrophoresis. *Phys. Rev. Lett.* **2007**, *98*, 198102.
(60) Cottet, J.; Fabregue, O.; Berger, C.; Buret, F.; Renaud, P.; Frénéa-Robin, M. MyDEP: A New Computational Tool for Dielectric Modeling of Particles and Cells. *Biophys. J.* **2019**, *116*, 12−18.
(61) Jones, T. B.; Kaler, K. V. I. S. Relationship of Rotational and Dielectrophoretic Cell Spectra. *Proceedings of the Twelfth Annual International Conference of the IEEE Engineering in Medicine and Biology Society* **1990**, 1515−1516.
(62) Kuzyk, A. Dielectrophoresis at the Nanoscale. *Electrophoresis* **2011**, *32*, 2307−2313.
(63) Pethig, R. Review—Where Is Dielectrophoresis (DEP) Going? *J. Electrochem. Soc.* **2017**, *164*, B3049−B3055.
(64) Pethig, R.*Dielectrophoresis - Theory, Methodology and Biological Applications*, 1st ed.; John Wiley & Sons, Ltd: Chichester, UK, 2017.
(65) Sarno, B.; Heineck, D.; Heller, M. J.; Ibsen, S. D. Dielectrophoresis: Developments and Applications from 2010 to 2020. *Electrophoresis* **2021**, *42*, 539−564.
(66) Albaladejo, S.; Marqués, M. I.; Laroche, M.; Sáenz, J. J. Scattering Forces from the Curl of the Spin Angular Momentum of a Light Field. *Phys. Rev. Lett.* **2009**, *102*, 113602.
(67) Kiel, M.; Möhwald, H.; Bargheer, M. Broadband Measurements of the Transient Optical Complex Dielectric Function of a Nanoparticle/Polymer Composite upon Ultrafast Excitation. *Phys. Rev. B* **2011**, *84*, 165121.
(68) Djorović, A.; Oldenburg, S. J.; Grand, J.; Le Ru, E. C. Extinction-to-Absorption Ratio for Sensitive Determination of the Size and Dielectric Function of Gold Nanoparticles. *ACS Nano* **2020**, *14*, 17597−17605.
(69) Chaumet, P. C.; Nieto-Vesperinas, M. Electromagnetic Force on a Metallic Particle in the Presence of a Dielectric Surface. *Phys. Rev. B* **2000**, *62*, 11185−11191.
(70) Fedoruk, M.; Meixner, M.; Carretero-Palacios, S.; Lohmüller, T.; Feldmann, J. Nanolithography by Plasmonic Heating and Optical Manipulation of Gold Nanoparticles. *ACS Nano* **2013**, *7*, 7648−7653.

https://doi.org/10.1021/acs.chemrev.2c00576
Chem. Rev. 2023, 123, 1680−1711

(71) Zhang, Q.; Xiao, J. J.; Zhang, X. M.; Yao, Y.; Liu, H. Reversal of Optical Binding Force by Fano Resonance in Plasmonic Nanorod Heterodimer. *Opt. Express* **2013**, *21*, 6601−6608.
(72) Li, Z.; Zhang, S.; Tong, L.; Wang, P.; Dong, B.; Xu, H. Ultrasensitive Size-Selection of Plasmonic Nanoparticles by Fano Interference Optical Force. *ACS Nano* **2014**, *8*, 701−708.
(73) Chen, H.; Liu, S.; Zi, J.; Lin, Z. Fano Resonance-Induced Negative Optical Scattering Force on Plasmonic Nanoparticles. *ACS Nano* **2015**, *9*, 1926−1935.
(74) Arias-González, J. R.; Nieto-Vesperinas, M. Radiation Pressure Over Dielectric and Metallic Nanocylinders on Surfaces: Polarization Dependence and Plasmon Resonance Conditions. *Opt. Lett.* **2002**, *27*, 2149−2151.
(75) Salary, M. M.; Mosallaei, H. Tailoring optical forces for nanoparticle manipulation on layered substrates. *Phys. Rev. B* **2016**, *94*, 035410.
(76) Johnson, P. B.; Christy, R. W. Optical Constants of the Noble Metals. *Phys. Rev. B* **1972**, *6*, 4370−4379.
(77) Huang, L.; Martin, O. J. F. Reversal of the Optical Force in a Plasmonic Trap. *Opt. Lett.* **2008**, *33*, 3001−3003.
(78) Bohren, C. F.; Huffman, D. R.*Absorption and Scattering of Light by Small Particles*; Wiley, 1998.
(79) Maier, S. a.*Plasmonics: Fundamentals and Applications*, 1st ed.; Springer: New York, NY, 2007.
(80) Zayats, A. V.; Smolyaninov, I. I.; Maradudin, A. A. Nano-Optics of Surface Plasmon Polaritons. *Phys. Rep.* **2005**, *408*, 131−314.
(81) Gordon, J. P.; Ashkin, A. Motion of Atoms in a Radiation Trap. *Phys. Rev. A* **1980**, *21*, 1606−1617.
(82) Descharmes, N.; Dharanipathy, U. P.; Diao, Z.; Tonin, M.; Houdré, R. Observation of Backaction and Self-Induced Trapping in a Planar Hollow Photonic Crystal Cavity. *Phys. Rev. Lett.* **2013**, *110*, 123601.
(83) Juan, M. L.; Gordon, R.; Pang, Y.; Eftekhari, F.; Quidant, R. Self-Induced Back-Action Optical Trapping of Dielectric Nanoparticles. *Nat. Phys.* **2009**, *5*, 915−919.
(84) Neumeier, L.; Quidant, R.; Chang, D. E. Self-Induced Back-Action Optical Trapping in Nanophotonic Systems. *New J. Phys.* **2015**, *17*, 123008.
(85) Jones, T.; Washizu, M. Equilibria and Dynamics of DEP-Levitated Particles: Multipolar Theory. *J. Electrostat.* **1994**, *33*, 199−212.
(86) Schnelle, T.; Müller, T.; Fiedler, S.; Fuhr, G. The Influence of Higher Moments on Particle Behaviour in Dielectrophoretic Field Cages. *J. Electrostat.* **1999**, *46*, 13−28.
(87) Voldman, J.; Braff, R. A.; Toner, M.; Gray, M. L.; Schmidt, M. A. Holding Forces of Single-Particle Dielectrophoretic Traps. *Biophys. J.* **2001**, *80*, 531−542.
(88) Liang, E.; Smith, R. L.; Clague, D. S. Dielectrophoretic Manipulation of Finite Sized Species and the Importance of the Quadrupolar Contribution. *Phys. Rev. E* **2004**, *70*, 066617.
(89) Rosales, C.; Lim, K. M. Numerical Comparison Between Maxwell Stress Method and Equivalent Multipole Approach for Calculation of the Dielectrophoretic Force in Single-Cell Traps. *Electrophoresis* **2005**, *26*, 2057−2065.
(90) Alaee, R.; Rockstuhl, C.; Fernandez-Corbaton, I. Exact Multipolar Decompositions with Applications in Nanophotonics. *Adv. Opt. Mater.* **2019**, *7*, 1800783.
(91) Smirnova, D.; Kivshar, Y. S. Multipolar Nonlinear Nanophotonics. *Optica* **2016**, *3*, 1241−1254.
(92) Lovera, A.; Gallinet, B.; Nordlander, P.; Martin, O. J. Mechanisms of Fano Resonances in Coupled Plasmonic Systems. *ACS Nano* **2013**, *7*, 4527−4536.
(93) Riccardi, M.; Martin, O. J. F. Role of Electric Currents in the Fano Resonances of Connected Plasmonic Structures. *Opt. Express* **2021**, *29*, 11635−11644.
(94) Nieto-Vesperinas, M.; Sáenz, J. J.; Gómez-Medina, R.; Chantada, L. Optical Forces on Small Magnetodielectric Particles. *Opt. Express* **2010**, *18*, 11428−11443.
(95) Liu, W.; Miroshnichenko, A. E.; Neshev, D. N.; Kivshar, Y. S. Broadband Unidirectional Scattering by Magneto-Electric Core−Shell Nanoparticles. *ACS Nano* **2012**, *6*, 5489−5497.
(96) Krasnok, A. E.; Simovski, C. R.; Belov, P. A.; Kivshar, Y. S. Superdirective Dielectric Nanoantennas. *Nanoscale* **2014**, *6*, 7354−7361.
(97) Liberal, I.; Ederra, I.; Gonzalo, R.; Ziolkowski, R. W. Superbackscattering from Single Dielectric Particles. *J. Opt.* **2015**, *17*, 072001.
(98) Kiselev, A.; Achouri, K.; Martin, O. J. F. Multipole Interplay Controls Optical Forces and Ultra-Directional Scattering. *Opt. Express* **2020**, *28*, 27547−27560.
(99) Achouri, K.; Kiselev, A.; Martin, O. J. F. Multipolar Origin of Electromagnetic Transverse Force Resulting from Two-Wave Interference. *Phys. Rev. B* **2020**, *102*, 085107.
(100) Nanz, S.*Toroidal Multipole Moments in Classical Electrodynamics*; Springer Fachmedien Wiesbaden: Wiesbaden, 2016.
(101) Evlyukhin, A. B.; Chichkov, B. N. Multipole Decompositions for Directional Light Scattering. *Phys. Rev. B* **2019**, *100*, 125415.
(102) Alnaimat, F.; Dagher, S.; Mathew, B.; Hilal-Alnqbi, A.; Khashan, S. Microfluidics Based Magnetophoresis: A Review. *Chem. Rec.* **2018**, *18*, 1596−1612.
(103) Roichman, Y.; Sun, B.; Stolarski, A.; Grier, D. G. Influence of Nonconservative Optical Forces on the Dynamics of Optically Trapped Colloidal Spheres: The Fountain of Probability. *Phys. Rev. Lett.* **2008**, *101*, 128301.
(104) Pesce, G.; Volpe, G.; De Luca, A. C.; Rusciano, G.; Volpe, G. Quantitative Assessment of Non-Conservative Radiation Forces in an Optical Trap. *Europhys. Lett.* **2009**, *86*, 38002.
(105) Wu, P.; Huang, R.; Tischer, C.; Jonas, A.; Florin, E.-L. Direct Measurement of the Nonconservative Force Field Generated by Optical Tweezers. *Phys. Rev. Lett.* **2009**, *103*, 108101.
(106) Zaman, M. A.; Padhy, P.; Hesselink, L. Near-Field Optical Trapping in a Non-Conservative Force Field. *Sci. Rep.* **2019**, *9*, 649.
(107) Van Bladel, J. G. Deep Field Penetration Into a Conducting Cylinder. *IEEE Trans. Electromagn. Compat.* **1996**, *38*, 549−556.
(108) Shalin, A. S.; Sukhov, S. V.; Bogdanov, A. A.; Belov, P. A.; Ginzburg, P. Optical Pulling Forces in Hyperbolic Metamaterials. *Phys. Rev. A* **2015**, *91*, 063830.
(109) Jiang, M.; Wang, G.; Xu, W.; Ji, W.; Zou, N.; Ho, H.-P.; Zhang, X. Two-Dimensional Arbitrary Nano-Manipulation on a Plasmonic Metasurface. *Opt. Lett.* **2018**, *43*, 1602−1605.
(110) Lovera, A.; Martin, O. J. F. Plasmonic Trapping with Realistic Dipole Nanoantennas: Analysis of the Detection Limit. *Appl. Phys. Lett.* **2011**, *99*, 151104.
(111) Barik, A.; Chen, X.; Oh, S.-H. Ultralow-Power Electronic Trapping of Nanoparticles with Sub-10 nm Gold Nanogap Electrodes. *Nano Lett.* **2016**, *16*, 6317−6324.
(112) Yoo, D.; Barik, A.; de León-Pérez, F.; Mohr, D. A.; Pelton, M.; Martín-Moreno, L.; Oh, S.-H. Plasmonic Split-Trench Resonator for Trapping and Sensing. *ACS Nano* **2021**, *15*, 6669−6677.
(113) Zhang, H.; Chang, H.; Neuzil, P. DEP-on-a-Chip: Dielectrophoresis Applied to Microfluidic Platforms. *Micromachines* **2019**, *10*, 423.
(114) Wang, L.; Flanagan, L. A.; Jeon, N. L.; Monuki, E.; Lee, A. P. Dielectrophoresis Switching with Vertical Sidewall Electrodes for Microfluidic Flow Cytometry. *Lab Chip* **2007**, *7*, 1114−1120.
(115) Chu, H. K.; Huan, Z.; Mills, J. K.; Yang, J.; Sun, D. Three-Dimensional Cell Manipulation and Patterning Using Dielectrophoresis Via a Multi-Layer Scaffold Structure. *Lab Chip* **2015**, *15*, 920−930.
(116) Cummings, E. B.; Singh, A. K. Dielectrophoresis in Microchips Containing Arrays of Insulating Posts: Theoretical and Experimental Results. *Anal. Chem.* **2003**, *75*, 4724−4731.
(117) Srivastava, S. K.; Gencoglu, A.; Minerick, A. R. DC Insulator Dielectrophoretic Applications in Microdevice Technology: A Review. *Anal. Bioanal. Chem.* **2011**, *399*, 301−321.

https://doi.org/10.1021/acs.chemrev.2c00576
Chem. Rev. 2023, 123, 1680−1711

(118) Lapizco-Encinas, B. H. On the Recent Developments of Insulator-Based Dielectrophoresis: A Review. *Electrophoresis* **2019**, *40*, 358−375.
(119) Cardenas-Benitez, B.; Jind, B.; Gallo-Villanueva, R. C.; Martinez-Chapa, S. O.; Lapizco-Encinas, B. H.; Perez-Gonzalez, V. H. Direct Current Electrokinetic Particle Trapping in Insulator-Based Microfluidics: Theory and Experiments. *Anal. Chem.* **2020**, *92*, 12871−12879.
(120) Liu, W.; Tao, Y.; Xue, R.; Song, C.; Wu, Q.; Ren, Y. Continuous-Flow Nanoparticle Trapping Driven by Hybrid Electrokinetics in Microfluidics. *Electrophoresis* **2021**, *42*, 939−949.
(121) Hawkins, B. G.; Smith, A. E.; Syed, Y. A.; Kirby, B. J. Continuous-Flow Particle Separation by 3D Insulative Dielectrophoresis Using Coherently Shaped, DC-Biased, AC Electric Fields. *Anal. Chem.* **2007**, *79*, 7291−7300.
(122) Lewpiriyawong, N.; Yang, C.; Lam, Y. C. Electrokinetically Driven Concentration of Particles and Cells by Dielectrophoresis with DC-Offset AC Electric Field. *Microfluid. Nanofluidics* **2012**, *12*, 723−733.
(123) Chiou, P. Y.; Ohta, A. T.; Wu, M. C. Massively Parallel Manipulation of Single Cells and Microparticles Using Optical Images. *Nature* **2005**, *436*, 370−372.
(124) Jamshidi, A.; Pauzauskie, P. J.; Schuck, P. J.; Ohta, A. T.; Chiou, P.-Y.; Chou, J.; Yang, P.; Wu, M. C. Dynamic Manipulation and Separation of Individual Semiconducting and Metallic Nanowires. *Nat. Photonics* **2008**, *2*, 85−89.
(125) Valley, J. K.; Jamshidi, A.; Ohta, A. T.; Hsu, H.-Y.; Wu, M. C. Operational Regimes and Physics Present in Optoelectronic Tweezers. *J. Microelectromechanical Syst.* **2008**, *17*, 342−350.
(126) Wu, M. C. Optoelectronic Tweezers. *Nat. Photonics* **2011**, *5*, 322−324.
(127) Zhang, S.; Juvert, J.; Cooper, J. M.; Neale, S. L. Manipulating and Assembling Metallic Beads with Optoelectronic Tweezers. *Sci. Rep.* **2016**, *6*, 32840.
(128) Ohta, A. T.; Chiou, P.-Y.; Phan, H. L.; Sherwood, S. W.; Yang, J. M.; Lau, A. N. K.; Hsu, H.-Y.; Jamshidi, A.; Wu, M. C. Optically Controlled Cell Discrimination and Trapping Using Optoelectronic Tweezers. *IEEE J. Sel. Top. Quantum Electron.* **2007**, *13*, 235−243.
(129) Zhang, W.; Huang, L.; Santschi, C.; Martin, O. J. F. Trapping and Sensing 10 nm Metal Nanoparticles Using Plasmonic Dipole Antennas. *Nano Lett.* **2010**, *10*, 1006−1011.
(130) Grier, D. G. A Revolution in Optical Manipulation. *Nature* **2003**, *424*, 810−816.
(131) Demergis, V.; Florin, E.-L. High Precision and Continuous Optical Transport Using a Standing Wave Optical Line Trap. *Opt. Express* **2011**, *19*, 20833−20848.
(132) Kottmann, J. P.; Martin, O. J. F. Plasmon Resonant Coupling in Metallic Nanowires. *Opt. Express* **2001**, *8*, 655−663.
(133) Righini, M.; Zelenina, A. S.; Girard, C.; Quidant, R. Parallel and Selective Trapping in a Patterned Plasmonic Landscape. *Nat. Phys.* **2007**, *3*, 477−480.
(134) Grzegorczyk, T. M.; Rohner, J.; Fournier, J.-M. Optical Mirror from Laser-Trapped Mesoscopic Particles. *Phys. Rev. Lett.* **2014**, *112*, 023902.
(135) Foti, A.; D'Andrea, C.; Villari, V.; Micali, N.; Donato, M. G.; Fazio, B.; Maragò, O. M.; Gillibert, R.; Lamy de la Chapelle, M.; Gucciardi, P. G. Optical Aggregation of Gold Nanoparticles for SERS Detection of Proteins and Toxins in Liquid Environment: Towards Ultrasensitive and Selective Detection. *Materials (Basel).* **2018**, *11*, 440.
(136) Forbes, K. A.; Bradshaw, D. S.; Andrews, D. L. Optical Binding of Nanoparticles. *Nanophotonics* **2019**, *9*, 1−17.
(137) Gordon, R. Biosensing with Nanoaperture Optical Tweezers. *Opt. Laser Technol.* **2019**, *109*, 328−335.
(138) Benz, F.; Schmidt, M. K.; Dreismann, A.; Chikkaraddy, R.; Zhang, Y.; Demetriadou, A.; Carnegie, C.; Ohadi, H.; de Nijs, B.; Esteban, R.; et al. Single-Molecule Optomechanics in "Picocavities. *Science (80-.)* **2016**, *354*, 726−729.
(139) Roller, E.-M.; Argyropoulos, C.; Högele, A.; Liedl, T.; Pilo-Pais, M. Plasmon−Exciton Coupling Using DNA Templates. *Nano Lett.* **2016**, *16*, 5962−5966.
(140) Quidant, R.; Girard, C. Surface-Plasmon-Based Optical Manipulation. *Laser Photon. Rev.* **2008**, *2*, 47−57.
(141) Abasahl, B.; Santschi, C.; Raziman, T. V.; Martin, O. J. F. Fabrication of Plasmonic Structures with Well-Controlled Nanometric Features: A Comparison Between Lift-Off and Ion Beam Etching. *Nanotechnology* **2021**, *32*, 475202.
(142) Riccardi, M.; Santschi, C.; Martin, O. J. F Controlling Surface Effects in Extremely High Aspect Ratio Gold Plasmonic Electrodes. *Microelectron. Eng.* **2022**, *263*, 111856.
(143) Bradac, C. Nanoscale Optical Trapping: A Review. *Adv. Opt. Mater.* **2018**, *6*, 1800005.
(144) Zemánek, P.; Jonáš, A.; Šrámek, L.; Liška, M. Optical Trapping of Nanoparticles and Microparticles by a Gaussian Standing Wave. *Opt. Lett.* **1999**, *24*, 1448−1450.
(145) Moffitt, J. R.; Chemla, Y. R.; Smith, S. B.; Bustamante, C. Recent Advances in Optical Tweezers. *Annu. Rev. Biochem.* **2008**, *77*, 205−228.
(146) Maragò, O. M.; Jones, P. H.; Gucciardi, P. G.; Volpe, G.; Ferrari, A. C. Optical Trapping and Manipulation of Nanostructures. *Nat. Nanotechnol.* **2013**, *8*, 807−819.
(147) Hughes, M. P.; Pethig, R.; Wang, X.-B. Dielectrophoretic Forces on Particles in Travelling Electric Fields. *J. Phys. D. Appl. Phys.* **1996**, *29*, 474−482.
(148) Jones, T. Basic Theory of Dielectrophoresis and Electrorotation. *IEEE Eng. Med. Biol. Mag.* **2003**, *22*, 33−42.
(149) Desai, J. P.; Pillarisetti, A.; Brooks, A. D. Engineering Approaches to Biomanipulation. *Annu. Rev. Biomed. Eng.* **2007**, *9*, 35−53.
(150) Pethig, R.; Talary, M.; Lee, R. Enhancing Traveling-Wave Dielectrophoresis with Signal Superposition. *IEEE Eng. Med. Biol. Mag.* **2003**, *22*, 43−50.
(151) Volpe, G.; Quidant, R.; Badenes, G.; Petrov, D. Surface Plasmon Radiation Forces. *Phys. Rev. Lett.* **2006**, *96*, 238101.
(152) Ploschner, M.; Čižmár, T.; Mazilu, M.; Di Falco, A.; Dholakia, K. Bidirectional Optical Sorting of Gold Nanoparticles. *Nano Lett.* **2012**, *12*, 1923−1927.
(153) Min, C.; Shen, Z.; Shen, J.; Zhang, Y.; Fang, H.; Yuan, G.; Du, L.; Zhu, S.; Lei, T.; Yuan, X. Focused Plasmonic Trapping of Metallic Particles. *Nat. Commun.* **2013**, *4*, 2891.
(154) Huft, P. R.; Kolbow, J. D.; Thweatt, J. T.; Lindquist, N. C. Holographic Plasmonic Nanotweezers for Dynamic Trapping and Manipulation. *Nano Lett.* **2017**, *17*, 7920−7925.
(155) Govorov, A. O.; Richardson, H. H. Generating Heat with Metal Nanoparticles. *Nano Today* **2007**, *2*, 30−38.
(156) Moriyama, Y.; Watanabe, E.; Kobayashi, K.; Harano, H.; Inui, E.; Takeda, K. Secondary Structural Change of Bovine Serum Albumin in Thermal Denaturation up to 130 °C and Protective Effect of Sodium Dodecyl Sulfate on the Change. *J. Phys. Chem. B* **2008**, *112*, 16585−16589.
(157) Donner, J. S.; Baffou, G.; McCloskey, D.; Quidant, R. Plasmon-Assisted Optofluidics. *ACS Nano* **2011**, *5*, 5457−5462.
(158) Baffou, G.; Cichos, F.; Quidant, R. Applications and Challenges of Thermoplasmonics. *Nat. Mater.* **2020**, *19*, 946−958.
(159) Gordon, R. Future Prospects for Biomolecular Trapping with Nanostructured Metals. *ACS Photonics* **2022**, *9*, 1127−1135.
(160) Crick, C. R.; Albella, P.; Ng, B.; Ivanov, A. P.; Roschuk, T.; Cecchini, M. P.; Bresme, F.; Maier, S. A.; Edel, J. B. Precise Attoliter Temperature Control of Nanopore Sensors Using a Nanoplasmonic Bullseye. *Nano Lett.* **2015**, *15*, 553−559.
(161) Jiang, Q.; Rogez, B.; Claude, J.-B.; Baffou, G.; Wenger, J. Temperature Measurement in Plasmonic Nanoapertures Used for Optical Trapping. *ACS Photonics* **2019**, *6*, 1763−1773.
(162) Kwak, T. J.; Hossen, I.; Bashir, R.; Chang, W.-J.; Lee, C. H. Localized Dielectric Loss Heating in Dielectrophoresis Devices. *Sci. Rep.* **2019**, *9*, 18977.

https://doi.org/10.1021/acs.chemrev.2c00576
Chem. Rev. 2023, 123, 1680−1711

(163) Wood, N. R.; Wolsiefer, A. I.; Cohn, R. W.; Williams, S. J. Dielectrophoretic Trapping of Nanoparticles with an Electrokinetic Nanoprobe. *Electrophoresis* **2013**, *34*, 1922−1930.
(164) Barik, A.; Zhang, Y.; Grassi, R.; Nadappuram, B. P.; Edel, J. B.; Low, T.; Koester, S. J.; Oh, S.-H. Graphene-Edge Dielectrophoretic Tweezers for Trapping of Biomolecules. *Nat. Commun.* **2017**, *8*, 1867.
(165) Roichman, Y.; Sun, B.; Roichman, Y.; Amato-Grill, J.; Grier, D. G. Optical Forces Arising from Phase Gradients. *Phys. Rev. Lett.* **2008**, *100*, 013602.
(166) Lee, S.-H.; Roichman, Y.; Grier, D. G. Optical Solenoid Beams. *Opt. Express* **2010**, *18*, 6988−6993.
(167) Rodrigo, J. A.; Angulo, M.; Alieva, T. All-Optical Motion Control of Metal Nanoparticles Powered by Propulsion Forces Tailored in 3D Trajectories. *Photonics Res.* **2021**, *9*, 1−12.
(168) Ruffner, D. B.; Grier, D. G. Optical Conveyors: A Class of Active Tractor Beams. *Phys. Rev. Lett.* **2012**, *109*, 163903.
(169) Brzobohatý, O.; Karásek, V.; Šiler, M.; Chvátal, L.; Čižmár, T.; Zemánek, P. Experimental Demonstration of Optical Transport, Sorting and Self-Arrangement Using a 'Tractor Beam. *Nat. Photonics* **2013**, *7*, 123−127.
(170) Barry, J. F.; McCarron, D. J.; Norrgard, E. B.; Steinecker, M. H.; DeMille, D. Magneto-Optical Trapping of a Diatomic Molecule. *Nature* **2014**, *512*, 286−289.
(171) Hänsch, T.; Schawlow, A. Cooling of Gases by Laser Radiation. *Opt. Commun.* **1975**, *13*, 68−69.
(172) Wieman, C. E.; Pritchard, D. E.; Wineland, D. J. Atom Cooling, Trapping, and Quantum Manipulation. *Rev. Mod. Phys.* **1999**, *71*, S253−S262.
(173) Raziman, T. V.; Martin, O. J. F. Universal Trapping in a Three-Beam Optical Lattice. *Phys. Rev. A* **2018**, *98*, 023420.
(174) Bruce, G. D.; Rodríguez-Sevilla, P.; Dholakia, K. Initiating Revolutions for Optical Manipulation: The Origins and Applications of Rotational Dynamics of Trapped Particles. *Adv. Phys. X* **2021**, *6*, 1838322.
(175) Jiang, Y.; Chen, H.; Chen, J.; Ng, J.; Lin, Z.Universal Relationships Between Optical Force/Torque and Orbital Versus Spin Momentum/Angular Momentum of Light. *arXiv*, December 29, 2017, 1511.08546, ver. *3*.
(176) Nieto-Vesperinas, M. Optical Torque: Electromagnetic Spin and Orbital-Angular-Momentum Conservation Laws and Their Significance. *Phys. Rev. A* **2015**, *92*, 043843.
(177) Maccabee, P.; Amassian, V.; Eberle, L.; Rudell, A.; Cracco, R.; Lai, K.; Somasundarum, M. Measurement of the Electric Field Induced into Inhomogeneous Volume Conductors by Magnetic Coils: Application to Human Spinal Neurogeometry. *Electroencephalogr. Clin. Neurophysiol. Potentials Sect.* **1991**, *81*, 224−237.
(178) Marston, P. L.; Crichton, J. H. Radiation Torque on a Sphere Caused by a Circularly-Polarized Electromagnetic Wave. *Phys. Rev. A* **1984**, *30*, 2508−2516.
(179) Arcenegui, J. J.; García-Sánchez, P.; Morgan, H.; Ramos, A. Electric-Field-Induced Rotation of Brownian Metal Nanowires. *Phys. Rev. E* **2013**, *88*, 033025.
(180) Lehmuskero, A.; Ogier, R.; Gschneidtner, T.; Johansson, P.; Käll, M. Ultrafast Spinning of Gold Nanoparticles in Water Using Circularly Polarized Light. *Nano Lett.* **2013**, *13*, 3129−3134.
(181) Yariv, A.; Yeh, P.*Optical Waves in Crystals: Propagation and Control of Laser Radiation*; Wiley, 2002.
(182) Shelton, W. A.; Bonin, K. D.; Walker, T. G. Nonlinear Motion of Optically Torqued Nanorods. *Phys. Rev. E* **2005**, *71*, 036204.
(183) Friese, M. E. J.; Nieminen, T. A.; Heckenberg, N. R.; Rubinsztein-Dunlop, H. Optical Alignment and Spinning of Laser-Trapped Microscopic Particles. *Nature* **1998**, *394*, 348−350.
(184) Miller, R.; Jones, T. Electro-Orientation of Ellipsoidal Erythrocytes. Theory and Experiment. *Biophys. J.* **1993**, *64*, 1588−1595.
(185) Tong, L.; Miljković, V. D.; Käll, M. Alignment, Rotation, and Spinning of Single Plasmonic Nanoparticles and Nanowires Using Polarization Dependent Optical Forces. *Nano Lett.* **2010**, *10*, 268−273.
(186) Simpson, G. J.; Wilson, C. F.; Gericke, K.-H.; Zare, R. N. Coupled Electrorotation: Two Proximate Microspheres Spin in Registry with an AC Electric Field. *ChemPhysChem* **2002**, *3*, 416−423.
(187) Sancho, M.; Martínez, G.; Muñoz, S.; Sebastián, J. L.; Pethig, R. Interaction Between Cells in Dielectrophoresis and Electrorotation Experiments. *Biomicrofluidics* **2010**, *4*, 022802.
(188) Hoettges, K. F.; McDonnell, M. B.; Hughes, M. P. Use of Combined Dielectrophoretic/Electrohydrodynamic Forces for Biosensor Enhancement. *J. Phys. D. Appl. Phys.* **2003**, *36*, L101−L104.
(189) Kumar, A.; Williams, S. J.; Wereley, S. T. Experiments on Opto-Electrically Generated Microfluidic Vortices. *Microfluid. Nanofluidics* **2009**, *6*, 637−646.
(190) Ndukaife, J. C.; Kildishev, A. V.; Nnanna, A. G. A.; Shalaev, V. M.; Wereley, S. T.; Boltasseva, A. Long-Range and Rapid Transport of Individual Nano-Objects by a Hybrid Electrothermoplasmonic Nanotweezer. *Nat. Nanotechnol.* **2016**, *11*, 53−59.
(191) Marcuse, D.*Light Transmission Optics*, 1st ed.; Van Nostrand Reinhold: New York, 1972.
(192) Friese, M. E. J.; Enger, J.; Rubinsztein-Dunlop, H.; Heckenberg, N. R. Optical Angular-Momentum Transfer to Trapped Absorbing Particles. *Phys. Rev. A* **1996**, *54*, 1593−1596.
(193) Allen, L.; Beijersbergen, M. W.; Spreeuw, R. J. C.; Woerdman, J. P. Orbital Angular Momentum of Light and the Transformation of Laguerre-Gaussian Laser Modes. *Phys. Rev. A* **1992**, *45*, 8185−8189.
(194) Barnett, S. M.; Allen, L. Orbital Angular Momentum and Nonparaxial Light Beams. *Opt. Commun.* **1994**, *110*, 670−678.
(195) O'Neil, A. T.; MacVicar, I.; Allen, L.; Padgett, M. J. Intrinsic and Extrinsic Nature of the Orbital Angular Momentum of a Light Beam. *Phys. Rev. Lett.* **2002**, *88*, 053601.
(196) Fernandez-Corbaton, I.; Zambrana-Puyalto, X.; Bonod, N.; Rockstuhl, C. Transverse Multipolar Light-Matter Couplings in Evanescent Waves. *Phys. Rev. A* **2016**, *94*, 053822.
(197) Rahimzadegan, A.; Alaee, R.; Fernandez-Corbaton, I.; Rockstuhl, C. Fundamental Limits of Optical Force and Torque. *Phys. Rev. B* **2017**, *95*, 035106.
(198) Wei, L.; Rodríguez-Fortuño, F. J. Optical Multipolar Torque in Structured Electromagnetic Fields: On Helicity Gradient Torque, Quadrupolar Torque, and Spin of the Field Gradient. *Phys. Rev. B* **2022**, *105*, 125424.
(199) Sebastián, J. L.; Muñoz, S.; Sancho, M.; Martínez, G.; Álvarez, G. Electromechanical Effects on Multilayered Cells in Nonuniform Rotating Fields. *Phys. Rev. E* **2011**, *84*, 011926.
(200) Erb, R. M.; Martin, J. J.; Soheilian, R.; Pan, C.; Barber, J. R. Actuating Soft Matter with Magnetic Torque. *Adv. Funct. Mater.* **2016**, *26*, 3859−3880.
(201) Chen, J.; Wan, C.; Zhan, Q. Engineering Photonic Angular Momentum with Structured Light: A Review. *Adv. Photonics* **2021**, *3*, 064001.
(202) Yang, Y.; Ren, Y.-X.; Chen, M.; Arita, Y.; Rosales-Guzmán, C. Optical Trapping with Structured Light: A Review. *Adv. Photonics* **2021**, *3*, 034001.
(203) He, H.; Friese, M. E. J.; Heckenberg, N. R.; Rubinsztein-Dunlop, H. Direct Observation of Transfer of Angular Momentum to Absorptive Particles from a Laser Beam with a Phase Singularity. *Phys. Rev. Lett.* **1995**, *75*, 826−829.
(204) Chen, M.; Mazilu, M.; Arita, Y.; Wright, E. M.; Dholakia, K. Dynamics of Microparticles Trapped in a Perfect Vortex Beam. *Opt. Lett.* **2013**, *38*, 4919−4922.
(205) Chong, A.; Wan, C.; Chen, J.; Zhan, Q. Generation of Spatiotemporal Optical Vortices with Controllable Transverse Orbital Angular Momentum. *Nat. Photonics* **2020**, *14*, 350−354.
(206) Ashkin, A. Forces of a Single-Beam Gradient Laser Trap on a Dielectric Sphere in the Ray Optics Regime. *Biophys. J.* **1992**, *61*, 569−582.
(207) Neuman, K. C.; Block, S. M. Optical Trapping. *Rev. Sci. Instrum.* **2004**, *75*, 2787−2809.
(208) Ashkin, A.*Optical Trapping and Manipulation of Neutral Particles Using Lasers - A Reprint Vol. with Commentaries*; World Scientific Publishing Co. Pte. Ltd., 2006.

https://doi.org/10.1021/acs.chemrev.2c00576
Chem. Rev. 2023, 123, 1680−1711

(209) Padgett, M.; Di Leonardo, R. Holographic Optical Tweezers and Their Relevance to Lab on Chip Devices. *Lab Chip* **2011**, *11*, 1196−1205.
(210) Lehmuskero, A.; Johansson, P.; Rubinsztein-Dunlop, H.; Tong, L.; Käll, M. Laser Trapping of Colloidal Metal Nanoparticles. *ACS Nano* **2015**, *9*, 3453−3469.
(211) Gao, D.; Ding, W.; Nieto-Vesperinas, M.; Ding, X.; Rahman, M.; Zhang, T.; Lim, C.; Qiu, C.-W. Optical Manipulation from the Microscale to the Nanoscale: Fundamentals, Advances and Prospects. *Light Sci. Appl.* **2017**, *6*, No. e17039.
(212) Polimeno, P.; Magazzù, A.; Iatì, M. A.; Patti, F.; Saija, R.; Degli Esposti Boschi, C.; Donato, M. G.; Gucciardi, P. G.; Jones, P. H.; Volpe, G.; et al. Optical Tweezers and Their Applications. *J. Quant. Spectrosc. Radiat. Transfer* **2018**, *218*, 131−150.
(213) Markx, G. H.; Talary, M. S.; Pethig, R. Separation of Viable and Non-Viable Yeast Using Dielectrophoresis. *J. Biotechnol.* **1994**, *32*, 29−37.
(214) Morgan, H.; Hughes, M. P.; Green, N. G. Separation of Submicron Bioparticles by Dielectrophoresis. *Biophys. J.* **1999**, *77*, 516−525.
(215) Zhang, J.; Yuan, D.; Zhao, Q.; Yan, S.; Tang, S.-Y.; Tan, S. H.; Guo, J.; Xia, H.; Nguyen, N.-T.; Li, W. Tunable Particle Separation in a Hybrid Dielectrophoresis (DEP)- Inertial Microfluidic Device. *Sensors Actuators B Chem.* **2018**, *267*, 14−25.
(216) Qin, Y.; Wu, L.; Schneider, T.; Yen, G. S.; Wang, J.; Xu, S.; Li, M.; Paguirigan, A. L.; Smith, J. L.; Radich, J. P.; et al. A Self-Digitization Dielectrophoretic (SD-DEP) Chip for High-Efficiency Single-Cell Capture, On-Demand Compartmentalization, and Downstream Nucleic Acid Analysis. *Angew. Chemie Int. Ed.* **2018**, *57*, 11378−11383.
(217) Mansoorifar, A.; Koklu, A.; Beskok, A. Quantification of Cell Death Using an Impedance-Based Microfluidic Device. *Anal. Chem.* **2019**, *91*, 4140−4148.
(218) Keim, K.; Rashed, M. Z.; Kilchenmann, S. C.; Delattre, A.; Gonçalves, A. F.; Éry, P.; Guiducci, C. On-Chip Technology for Single-Cell Arraying, Electrorotation-Based Analysis and Selective Release. *Electrophoresis* **2019**, *40*, 1830−1838.
(219) Henslee, E. A.; Sano, M. B.; Rojas, A. D.; Schmelz, E. M.; Davalos, R. V. Selective Concentration of Human Cancer Cells Using Contactless Dielectrophoresis. *Electrophoresis* **2011**, *32*, 2523−2529.
(220) Jones, P. V.; Huey, S.; Davis, P.; McLemore, R.; McLaren, A.; Hayes, M. A. Biophysical Separation of Staphylococcus Epidermidis Strains Based on Antibiotic Resistance. *Analyst* **2015**, *140*, 5152−5161.
(221) Khondaker, S. I.; Luo, K.; Yao, Z. The Fabrication of Single-Electron Transistors Using Dielectrophoretic Trapping of Individual Gold Nanoparticles. *Nanotechnology* **2010**, *21*, 095204.
(222) Barik, A.; Otto, L. M.; Yoo, D.; Jose, J.; Johnson, T. W.; Oh, S.-H. Dielectrophoresis-Enhanced Plasmonic Sensing with Gold Nanohole Arrays. *Nano Lett.* **2014**, *14*, 2006−2012.
(223) Hölzel, R.; Calander, N.; Chiragwandi, Z.; Willander, M.; Bier, F. F. Trapping Single Molecules by Dielectrophoresis. *Phys. Rev. Lett.* **2005**, *95*, 128102.
(224) Freedman, K. J.; Otto, L. M.; Ivanov, A. P.; Barik, A.; Oh, S.-H.; Edel, J. B. Nanopore Sensing at Ultra-Low Concentrations Using Single-Molecule Dielectrophoretic Trapping. *Nat. Commun.* **2016**, *7*, 10217.
(225) Ertsgaard, C. T.; Wittenberg, N. J.; Klemme, D. J.; Barik, A.; Shih, W.-C.; Oh, S.-H. Integrated Nanogap Platform for Sub-Volt Dielectrophoretic Trapping and Real-Time Raman Imaging of Biological Nanoparticles. *Nano Lett.* **2018**, *18*, 5946−5953.
(226) Hong, S.; Shim, O.; Kwon, H.; Choi, Y. Autoenhanced Raman Spectroscopy via Plasmonic Trapping for Molecular Sensing. *Anal. Chem.* **2016**, *88*, 7633−7638.
(227) Chapin, S. C.; Germain, V.; Dufresne, E. R. Automated Trapping, Assembly, and Sorting with Holographic Optical Tweezers. *Opt. Express* **2006**, *14*, 13095−13100.
(228) Choi, S.; Lee, G.; Park, I. S.; Son, M.; Kim, W.; Lee, H.; Lee, S.-Y.; Na, S.; Yoon, D. S.; Bashir, R.; et al. Detection of Silver Ions Using Dielectrophoretic Tweezers-Based Force Spectroscopy. *Anal. Chem.* **2016**, *88*, 10867−10875.
(229) Capitanio, M.; Pavone, F. Interrogating Biology with Force: Single Molecule High-Resolution Measurements with Optical Tweezers. *Biophys. J.* **2013**, *105*, 1293−1303.
(230) Xie, C.; Dinno, M. A.; Li, Y.-q. Near-Infrared Raman Spectroscopy of Single Optically Trapped Biological Cells. *Opt. Lett.* **2002**, *27*, 249−251.
(231) Enger, J.; Goksör, M.; Ramser, K.; Hagberg, P.; Hanstorp, D. Optical Tweezers Applied to a Microfluidic System. *Lab Chip* **2004**, *4*, 196−200.
(232) Donato, M. G.; Monaca, M. A.; Faggio, G.; Stefano, L. D.; Jones, P. H.; Gucciardi, P. G.; Maragò, O. M. Optical Trapping of Porous Silicon Nanoparticles. *Nanotechnology* **2011**, *22*, 505704.
(233) Geiselmann, M.; Juan, M. L.; Renger, J.; Say, J. M.; Brown, L. J.; de Abajo, F. J. G.; Koppens, F.; Quidant, R. Three-Dimensional Optical Manipulation of a Single Electron Spin. *Nat. Nanotechnol.* **2013**, *8*, 175−179.
(234) Setoura, K.; Tsuji, T.; Ito, S.; Kawano, S.; Miyasaka, H. Opto-Thermophoretic Separation and Trapping of Plasmonic Nanoparticles. *Nanoscale* **2019**, *11*, 21093−21102.
(235) Kim, J.; Martin, O. J. F. Surfactants Control Optical Trapping near a Glass Wall. *J. Phys. Chem. C* **2022**, *126*, 378−386.
(236) Bulushev, R. D.; Marion, S.; Radenovic, A. Relevance of the Drag Force during Controlled Translocation of a DNA−Protein Complex through a Glass Nanocapillary. *Nano Lett.* **2015**, *15*, 7118−7125.
(237) Ashkin, A.; Dziedzic, J. M. Optical Trapping and Manipulation of Viruses and Bacteria. *Science (80-.).* **1987**, *235*, 1517−1520.
(238) Dai, J.; Sheetz, M. P.Chapter 9 Cell Membrane Mechanics. In *Methods Cell Biol.*, Vol. *55*; Sheetz, M. P., Ed.; Academic Press, 1998; pp 157−171.
(239) Rancourt-Grenier, S.; Wei, M.-T.; Bai, J.-J.; Chiou, A.; Bareil, P. P.; Duval, P.-L.; Sheng, Y. Dynamic Deformation of Red Blood Cell in Dual-Trap Optical Tweezers. *Opt. Express* **2010**, *18*, 10462−10472.
(240) Berns, M. W. Laser Scissors and Tweezers to Study Chromosomes: A Review. *Front. Bioeng. Biotechnol.* **2020**, *8*, 721.
(241) Patrick, E. M.; Slivka, J. D.; Payne, B.; Comstock, M. J.; Schmidt, J. C. Observation of Processive Telomerase Catalysis Using High-Resolution Optical Tweezers. *Nat. Chem. Biol.* **2020**, *16*, 801−809.
(242) Neuman, K. C.; Nagy, A. Single-Molecule Force Spectroscopy: Optical Tweezers, Magnetic Tweezers and Atomic Force Microscopy. *Nat. Methods* **2008**, *5*, 491−505.
(243) Black, J. W.; Kamenetska, M.; Ganim, Z. An Optical Tweezers Platform for Single Molecule Force Spectroscopy in Organic Solvents. *Nano Lett.* **2017**, *17*, 6598−6605.
(244) Mandal, S. S. Force Spectroscopy on Single Molecules of Life. *ACS Omega* **2020**, *5*, 11271−11278.
(245) Liphardt, J.; Dumont, S.; Smith, S. B.; Tinoco, I. J.; Bustamante, C. Equilibrium Information from Nonequilibrium Measurements in an Experimental Test of Jarzynski's Equality. *Science (80-.)* **2002**, *296*, 1832−1835.
(246) Meiners, J.-C.; Quake, S. R. Femtonewton Force Spectroscopy of Single Extended DNA Molecules. *Phys. Rev. Lett.* **2000**, *84*, 5014−5017.
(247) Cheng, P.; Barrett, M. J.; Oliver, P. M.; Cetin, D.; Vezenov, D. Dielectrophoretic Tweezers as a Platform for Molecular Force Spectroscopy in a Highly Parallel Format. *Lab Chip* **2011**, *11*, 4248−4259.
(248) Veigel, C.; Schmidt, C. F. Moving into the Cell: Single-Molecule Studies of Molecular Motors in Complex Environments. *Nat. Rev. Mol. Cell Biol.* **2011**, *12*, 163−176.
(249) Svoboda, K.; Schmidt, C. F.; Schnapp, B. J.; Block, S. M. Direct Observation of Kinesin Stepping by Optical Trapping Interferometry. *Nature* **1993**, *365*, 721−727.
(250) Nishiyama, M.; Muto, E.; Inoue, Y.; Yanagida, T.; Higuchi, H. Substeps within the 8-nm Step of the ATPase Cycle of Single Kinesin Molecules. *Nat. Cell Biol.* **2001**, *3*, 425−428.

https://doi.org/10.1021/acs.chemrev.2c00576
Chem. Rev. 2023, 123, 1680−1711

(251) Jia, L.; Moorjani, S. G.; Jackson, T. N.; Hancock, W. O. Microscale Transport and Sorting by Kinesin Molecular Motors. *Biomed. Microdevices* **2004**, *6*, 67−74.
(252) Washizu, M.; Kurahashi, Y.; Iochi, H.; Kurosawa, O.; Aizawa, S.-i.; Kudo, S.; Magariyama, Y.; Hotani, H. Dielectrophoretic Measurement of Bacterial Motor Characteristics. *IEEE Trans. Ind. Appl.* **1993**, *29*, 286−294.
(253) Berry, R. M.; Berg, H. C. Torque Generated by the Bacterial Flagellar Motor Close to Stall. *Biophys. J.* **1996**, *71*, 3501−3510.
(254) Watanabe-Nakayama, T.; Toyabe, S.; Kudo, S.; Sugiyama, S.; Yoshida, M.; Muneyuki, E. Effect of External Torque on the ATP-Driven Rotation of F1-ATPase. *Biochem. Biophys. Res. Commun.* **2008**, *366*, 951−957.
(255) Toyabe, S.; Okamoto, T.; Watanabe-Nakayama, T.; Taketani, H.; Kudo, S.; Muneyuki, E. Nonequilibrium Energetics of a Single F1-ATPase Molecule. *Phys. Rev. Lett.* **2010**, *104*, 198103.
(256) Toyabe, S.; Watanabe-Nakayama, T.; Okamoto, T.; Kudo, S.; Muneyuki, E. Thermodynamic Efficiency and Mechanochemical Coupling of F1 -ATPase. *Proc. Natl. Acad. Sci. U. S. A.* **2011**, *108*, 17951−17956.
(257) Tang, J.; Yang, G.; Zhang, Q.; Parhat, A.; Maynor, B.; Liu, J.; Qin, L.-C.; Zhou, O. Rapid and Reproducible Fabrication of Carbon Nanotube AFM Probes by Dielectrophoresis. *Nano Lett.* **2005**, *5*, 11−14.
(258) Chizari, S.; Shaw, L. A.; Hopkins, J. B. Simultaneous Printing and Deformation of Microsystems via Two-Photon Lithography and Holographic Optical Tweezers. *Mater. Horizons* **2019**, *6*, 350−355.
(259) Li, J.; Zhang, Q.; Yang, D.; Tian, J. Fabrication of Carbon Nanotube Field Effect Transistors by AC Dielectrophoresis Method. *Carbon N. Y.* **2004**, *42*, 2263−2267.
(260) Suehiro, J.; Zhou, G.; Hara, M. Fabrication of a Carbon Nanotube-Based Gas Sensor using Dielectrophoresis and Its Application for Ammonia Detection by Impedance Spectroscopy. *J. Phys. D. Appl. Phys.* **2003**, *36*, L109−L114.
(261) Ito, S.; Yoshikawa, H.; Masuhara, H. Optical Patterning and Photochemical Fixation of Polymer Nanoparticles on Glass Substrates. *Appl. Phys. Lett.* **2001**, *78*, 2566−2568.
(262) Guffey, M. J.; Scherer, N. F. All-Optical Patterning of Au Nanoparticles on Surfaces Using Optical Traps. *Nano Lett.* **2010**, *10*, 4302−4308.
(263) Gould, O. E. C.; Box, S. J.; Boott, C. E.; Ward, A. D.; Winnik, M. A.; Miles, M. J.; Manners, I. Manipulation and Deposition of Complex, Functional Block Copolymer Nanostructures Using Optical Tweezers. *ACS Nano* **2019**, *13*, 3858−3866.
(264) Köhler, J.; Ksouri, S. I.; Esen, C.; Ostendorf, A. Optical Screw-Wrench for Microassembly. *Microsystems Nanoeng* **2017**, *3*, 16083.
(265) Terray, A.; Oakey, J.; Marr, D. W. M. Microfluidic Control Using Colloidal Devices. *Science (80-.)* **2002**, *296*, 1841−1844.
(266) Terray, A.; Oakey, J.; Marr, D. W. M. Fabrication of Linear Colloidal Structures for Microfluidic Applications. *Appl. Phys. Lett.* **2002**, *81*, 1555−1557.
(267) Maruo, S.; Takaura, A.; Saito, Y. Optically Driven Micropump with a Twin Spiral Microrotor. *Opt. Express* **2009**, *17*, 18525−18532.
(268) Lin, C.-L.; Vitrant, G.; Bouriau, M.; Casalegno, R.; Baldeck, P. L. Optically Driven Archimedes Micro-Screws for Micropump Application. *Opt. Express* **2011**, *19*, 8267−8276.
(269) Leach, J.; Mushfique, H.; di Leonardo, R.; Padgett, M.; Cooper, J. An Optically Driven Pump for Microfluidics. *Lab Chip* **2006**, *6*, 735−739.
(270) Ladavac, K.; Grier, D. G. Microoptomechanical Pumps Assembled and Driven by Holographic Optical Vortex Arrays. *Opt. Express* **2004**, *12*, 1144−1149.
(271) Liu, W.; Ren, Y.; Tao, Y.; Chen, X.; Yao, B.; Hui, M.; Bai, L. Control of Two-Phase Flow in Microfluidics Using Out-of-Phase Electroconvective Streaming. *Phys. Fluids* **2017**, *29*, 112002.
(272) Huang, Y.; Holzel, R.; Pethig, R.; Wang, X.-B. Differences in the AC Electrodynamics of Viable and Non-Viable Yeast Cells Determined Through Combined Dielectrophoresis and Electrorotation Studies. *Phys. Med. Biol.* **1992**, *37*, 1499−1517.
(273) Schwaferts, C.; Sogne, V.; Welz, R.; Meier, F.; Klein, T.; Niessner, R.; Elsner, M.; Ivleva, N. P. Nanoplastic Analysis by Online Coupling of Raman Microscopy and Field-Flow Fractionation Enabled by Optical Tweezers. *Anal. Chem.* **2020**, *92*, 5813−5820.
(274) Sullivan, R. C.; Boyer-Chelmo, H.; Gorkowski, K.; Beydoun, H. Aerosol Optical Tweezers Elucidate the Chemistry, Acidity, Phase Separations, and Morphology of Atmospheric Microdroplets. *Acc. Chem. Res.* **2020**, *53*, 2498−2509.
(275) Soe, A. K.; Nahavandi, S.; Khoshmanesh, K. Neuroscience Goes on a Chip. *Biosens. Bioelectron.* **2012**, *35*, 1−13.
(276) Lenton, I. C. D.; Scott, E. K.; Rubinsztein-Dunlop, H.; Favre-Bulle, I. A. Optical Tweezers Exploring Neuroscience. *Front. Bioeng. Biotechnol.* **2020**, *8*, 602797.
(277) Ashkin, A.*Nobel Lecture: Optical Tweezers and their Application to Biological Systems*; Watson Publishing International LLC, 2018; pp 65−78.
(278) Tan, H.; Hu, H.; Huang, L.; Qian, K. Plasmonic Tweezers for Optical Manipulation and Biomedical Applications. *Analyst* **2020**, *145*, 5699−5712.
(279) Huang, L.; Maerkl, S. J.; Martin, O. J. F. Integration of Plasmonic Trapping in a Microfluidic Environment. *Opt. Express* **2009**, *17*, 6018−6024.
(280) Wang, K.; Schonbrun, E.; Steinvurzel, P.; Crozier, K. B. Trapping and Rotating Nanoparticles Using a Plasmonic Nano-Tweezer with an Integrated Heat Sink. *Nat. Commun.* **2011**, *2*, 469.
(281) Yoo, D.; Gurunatha, K. L.; Choi, H.-K.; Mohr, D. A.; Ertsgaard, C. T.; Gordon, R.; Oh, S.-H. Low-Power Optical Trapping of Nanoparticles and Proteins with Resonant Coaxial Nanoaperture Using 10 nm Gap. *Nano Lett.* **2018**, *18*, 3637−3642.
(282) Berthelot, J.; Aćimović, S. S.; Juan, M. L.; Kreuzer, M. P.; Renger, J.; Quidant, R. Three-Dimensional Manipulation with Scanning Near-Field Optical Nanotweezers. *Nat. Nanotechnol.* **2014**, *9*, 295−299.
(283) Ehtaiba, J. M.; Gordon, R. Template-Stripped Nanoaperture Tweezer Integrated with Optical Fiber. *Opt. Express* **2018**, *26*, 9607−9613.
(284) Pang, Y.; Gordon, R. Optical Trapping of 12 nm Dielectric Spheres Using Double-Nanoholes in a Gold Film. *Nano Lett.* **2011**, *11*, 3763−3767.
(285) Chen, C.; Juan, M. L.; Li, Y.; Maes, G.; Borghs, G.; Van Dorpe, P.; Quidant, R. Enhanced Optical Trapping and Arrangement of Nano-Objects in a Plasmonic Nanocavity. *Nano Lett.* **2012**, *12*, 125−132.
(286) Mestres, P.; Berthelot, J.; Aćimović, S. S.; Quidant, R. Unraveling the Optomechanical Nature of Plasmonic Trapping. *Light Sci. Appl.* **2016**, *5*, No. e16092.
(287) Wheaton, S.; Gordon, R. Molecular Weight Characterization of Single Globular Proteins Using Optical Nanotweezers. *Analyst* **2015**, *140*, 4799−4803.
(288) Trichet, A. A. P.; Dolan, P. R.; James, D.; Hughes, G. M.; Vallance, C.; Smith, J. M. Nanoparticle Trapping and Characterization Using Open Microcavities. *Nano Lett.* **2016**, *16*, 6172−6177.
(289) Cui, L.; Holmes, D.; Morgan, H. The Dielectrophoretic Levitation and Separation of Latex Beads in Microchips. *Electrophoresis* **2001**, *22*, 3893−3901.
(290) Kauffmann, P.; Pham, P.; Masse, A.; Kustov, M.; Honegger, T.; Peyrade, D.; Haguet, V.; Reyne, G. Contactless Dielectrophoretic Handling of Diamagnetic Levitating Water Droplets in Air. *IEEE Trans. Magn.* **2010**, *46*, 3293−3296.
(291) Brown, C. V.; Edwards, A. M. J.; Roberts, A.; Newton, M. I.; Sage, I. C.; Ledesma-Aguilar, R.; McHale, G. Bubble Control, Levitation, and Manipulation Using Dielectrophoresis. *Adv. Mater. Interfaces* **2021**, *8*, 2001204.
(292) Ashkin, A.; Dziedzic, J. M. Optical Levitation by Radiation Pressure. *Appl. Phys. Lett.* **1971**, *19*, 283−285.
(293) Jauffred, L.; Taheri, S. M.-R.; Schmitt, R.; Linke, H.; Oddershede, L. B. Optical Trapping of Gold Nanoparticles in Air. *Nano Lett.* **2015**, *15*, 4713−4719.

https://doi.org/10.1021/acs.chemrev.2c00576
Chem. Rev. 2023, 123, 1680−1711

(294) Thalhammer, G.; Steiger, R.; Bernet, S.; Ritsch-Marte, M. Optical Macro-Tweezers: Trapping of Highly Motile Micro-Organisms. *J. Opt.* **2011**, *13*, 044024.
(295) Chang, D. E.; Regal, C. A.; Papp, S. B.; Wilson, D. J.; Ye, J.; Painter, O.; Kimble, H. J.; Zoller, P. Cavity Opto-Mechanics Using an Optically Levitated Nanosphere. *Proc. Natl. Acad. Sci. U. S. A.* **2010**, *107*, 1005−1010.
(296) Neukirch, L. P.; von Haartman, E.; Rosenholm, J. M.; Nick Vamivakas, A. Multi-Dimensional Single-Spin Nano-Optomechanics with a Levitated Nanodiamond. *Nat. Photonics* **2015**, *9*, 653−657.
(297) Minowa, Y.; Kawai, R.; Ashida, M. Optical Levitation of a Microdroplet Containing a Single Quantum Dot. *Opt. Lett.* **2015**, *40*, 906−909.
(298) Michimura, Y.; Kuwahara, Y.; Ushiba, T.; Matsumoto, N.; Ando, M. Optical Levitation of a Mirror for Reaching the Standard Quantum Limit. *Opt. Express* **2017**, *25*, 13799−13806.
(299) Monteiro, F.; Ghosh, S.; Fine, A. G.; Moore, D. C. Optical Levitation of 10-ng Spheres with Nano-g Acceleration Sensitivity. *Phys. Rev. A* **2017**, *96*, 063841.
(300) Diehl, R.; Hebestreit, E.; Reimann, R.; Tebbenjohanns, F.; Frimmer, M.; Novotny, L. Optical Levitation and Feedback Cooling of a Nanoparticle at Subwavelength Distances from a Membrane. *Phys. Rev. A* **2018**, *98*, 013851.
(301) Zheng, Y.; Zhou, L.-M.; Dong, Y.; Qiu, C.-W.; Chen, X.-D.; Guo, G.-C.; Sun, F.-W. Robust Optical-Levitation-Based Metrology of Nanoparticle's Position and Mass. *Phys. Rev. Lett.* **2020**, *124*, 223603.
(302) Dholakia, K.; Zemánek, P. Colloquium: Gripped by Light: Optical Binding. *Rev. Mod. Phys.* **2010**, *82*, 1767−1791.
(303) Khlebtsov, B.; Melnikov, A.; Zharov, V.; Khlebtsov, N. Absorption and Scattering of Light by a Dimer of Metal Nanospheres: Comparison of Dipole and Multipole Approaches. *Nanotechnology* **2006**, *17*, 1437−1445.
(304) Tang, S.-Y.; Zhu, J.; Sivan, V.; Gol, B.; Soffe, R.; Zhang, W.; Mitchell, A.; Khoshmanesh, K. Creation of Liquid Metal 3D Microstructures Using Dielectrophoresis. *Adv. Funct. Mater.* **2015**, *25*, 4445−4452.
(305) Huang, N.; Martínez, L. J.; Jaquay, E.; Nakano, A.; Povinelli, M. L. Optical Epitaxial Growth of Gold Nanoparticle Arrays. *Nano Lett.* **2015**, *15*, 5841−5845.
(306) Dereux, A.; Girard, C.; Martin, O. J. F.; Devel, M. Optical Binding in Scanning Probe Microscopy. *Europhys. Lett.* **1994**, *26*, 37−42.
(307) Gierhart, B. C.; Howitt, D. G.; Chen, S. J.; Smith, R. L.; Collins, S. D. Frequency Dependence of Gold Nanoparticle Superassembly by Dielectrophoresis. *Langmuir* **2007**, *23*, 12450−12456.
(308) Cheon, D.; Kumar, S.; Kim, G.-H. Assembly of Gold Nanoparticles of Different Diameters between Nanogap Electrodes. *Appl. Phys. Lett.* **2010**, *96*, 013101.
(309) Liu, W.; Wang, C.; Ding, H.; Shao, J.; Ding, Y. AC Electric Field Induced Dielectrophoretic Assembly Behavior of Gold Nanoparticles in a Wide Frequency Range. *Appl. Surf. Sci.* **2016**, *370*, 184−192.
(310) Rozynek, Z.; Han, M.; Dutka, F.; Garstecki, P.; Józefczak, A.; Luijten, E. Formation of Printable Granular and Colloidal Chains through Capillary Effects and Dielectrophoresis. *Nat. Commun.* **2017**, *8*, 15255.
(311) Freer, E. M.; Grachev, O.; Duan, X.; Martin, S.; Stumbo, D. P. High-Yield Self-Limiting Single-Nanowire Assembly with Dielectrophoresis. *Nat. Nanotechnol.* **2010**, *5*, 525−530.
(312) Shekhar, S.; Stokes, P.; Khondaker, S. I. Ultrahigh Density Alignment of Carbon Nanotube Arrays by Dielectrophoresis. *ACS Nano* **2011**, *5*, 1739−1746.
(313) Chai, Z.; Yilmaz, C.; Busnaina, A. A.; Lissandrello, C. A.; Carter, D. J. D. Directed Assembly-Based Printing of Homogeneous and Hybrid Nanorods Using Dielectrophoresis. *Nanotechnology* **2017**, *28*, 475303.
(314) Cha, S.-H.; Kang, S.-H.; Lee, Y. J.; Kim, J.-H.; Ahn, E.-Y.; Park, Y.; Cho, S. Fabrication of Nanoribbons by Dielectrophoresis Assisted Cold Welding of Gold Nanoparticles on Mica Substrate. *Sci. Rep.* **2019**, *9*, 3629.
(315) Burns, M. M.; Fournier, J.-M.; Golovchenko, J. A. Optical Binding. *Phys. Rev. Lett.* **1989**, *63*, 1233−1236.
(316) Yan, Z.; Shah, R. A.; Chado, G.; Gray, S. K.; Pelton, M.; Scherer, N. F. Guiding Spatial Arrangements of Silver Nanoparticles by Optical Binding Interactions in Shaped Light Fields. *ACS Nano* **2013**, *7*, 1790−1802.
(317) Kudo, T.; Yang, S.-J.; Masuhara, H. A Single Large Assembly with Dynamically Fluctuating Swarms of Gold Nanoparticles Formed by Trapping Laser. *Nano Lett.* **2018**, *18*, 5846−5853.
(318) Nan, F.; Han, F.; Scherer, N. F.; Yan, Z. Dissipative Self-Assembly of Anisotropic Nanoparticle Chains with Combined Electrodynamic and Electrostatic Interactions. *Adv. Mater.* **2018**, *30*, 1803238.
(319) Bao, Y.; Yan, Z.; Scherer, N. F. Optical Printing of Electrodynamically Coupled Metallic Nanoparticle Arrays. *J. Phys. Chem. C* **2014**, *118*, 19315−19321.
(320) Yan, Z.; Gray, S. K.; Scherer, N. F. Potential Energy Surfaces and Reaction Pathways for Light-Mediated Self-Organization of Metal Nanoparticle Clusters. *Nat. Commun.* **2014**, *5*, 3751.
(321) Kostina, N.; Petrov, M.; Ivinskaya, A.; Sukhov, S.; Bogdanov, A.; Toftul, I.; Nieto-Vesperinas, M.; Ginzburg, P.; Shalin, A. Optical Binding via Surface Plasmon Polariton Interference. *Phys. Rev. B* **2019**, *99*, 125416.
(322) Zhang, Q.; Xiao, J. J. Multiple Reversals of Optical Binding Force in Plasmonic Disk-Ring Nanostructures with Dipole-Multipole Fano Resonances. *Opt. Lett.* **2013**, *38*, 4240−4143.
(323) Rivy, H. M.; Mahdy, M.; Jony, Z. R.; Masud, N.; Satter, S. S.; Jani, R. Plasmonic or Dielectric Dimers: A Generic Way to Control the Reversal of Near Field Optical Binding Force. *Opt. Commun.* **2019**, *430*, 51−62.
(324) Yan, Z.; Sajjan, M.; Scherer, N. F. Fabrication of a Material Assembly of Silver Nanoparticles Using the Phase Gradients of Optical Tweezers. *Phys. Rev. Lett.* **2015**, *114*, 143901.
(325) Coursault, D.; Sule, N.; Parker, J.; Bao, Y.; Scherer, N. F. Dynamics of the Optically Directed Assembly and Disassembly of Gold Nanoplatelet Arrays. *Nano Lett.* **2018**, *18*, 3391−3399.
(326) Peterson, C. W.; Parker, J.; Rice, S. A.; Scherer, N. F. Controlling the Dynamics and Optical Binding of Nanoparticle Homodimers with Transverse Phase Gradients. *Nano Lett.* **2019**, *19*, 897−903.
(327) Zemánek, P.; Volpe, G.; Jonáš, A.; Brzobohatý, O. Perspective on Light-Induced Transport of Particles: From Optical Forces to Phoretic Motion. *Adv. Opt. Photonics* **2019**, *11*, 577−678.
(328) Graham, D. M.; Messerli, M. A.; Pethig, R. Spatial Manipulation of Cells and Organelles Using Single Electrode Dielectrophoresis. *Biotechniques* **2012**, *52*, 39−43.
(329) Natu, R.; Islam, M.; Keck, D.; Martinez-Duarte, R. Automated "Pick and Transfer" of Targeted Cells Using Dielectrophoresis. *Lab Chip* **2019**, *19*, 2512−2525.
(330) Curtis, J. E.; Koss, B. A.; Grier, D. G. Dynamic Holographic Optical Tweezers. *Opt. Commun.* **2002**, *207*, 169−175.
(331) Won, J.; Inaba, T.; Masuhara, H.; Fujiwara, H.; Sasaki, K.; Miyawaki, S.; Sato, S. Photothermal Fixation of Laser-Trapped Polymer Microparticles on Polymer Substrates. *Appl. Phys. Lett.* **1999**, *75*, 1506−1508.
(332) Čižmár, T.; Garcés-Chávez, V.; Dholakia, K.; Zemánek, P. Optical Conveyor Belt for Delivery of Submicron Objects. *Appl. Phys. Lett.* **2005**, *86*, 174101.
(333) Wang, K.; Schonbrun, E.; Steinvurzel, P.; Crozier, K. B. Scannable Plasmonic Trapping Using a Gold Stripe. *Nano Lett.* **2010**, *10*, 3506−3511.
(334) Zheng, Y.; Ryan, J.; Hansen, P.; Cheng, Y.-T.; Lu, T.-J.; Hesselink, L. Nano-Optical Conveyor Belt, Part II: Demonstration of Handoff Between Near-Field Optical Traps. *Nano Lett.* **2014**, *14*, 2971−2976.
(335) Jiang, M.; Wang, G.; Jiao, W.; Ying, Z.; Zou, N.; Ho, H.-p.; Sun, T.; Zhang, X. Plasmonic Non-Concentric Nanorings Array as an

https://doi.org/10.1021/acs.chemrev.2c00576
Chem. Rev. 2023, 123, 1680−1711

Unidirectional Nano-Optical Conveyor Belt Actuated by Polarization Rotation. *Opt. Lett.* **2017**, *42*, 259−262.
(336) Hansen, P.; Zheng, Y.; Ryan, J.; Hesselink, L. Nano-Optical Conveyor Belt, Part I: Theory. *Nano Lett.* **2014**, *14*, 2965−2970.
(337) Wu, S.-H.; Huang, N.; Jaquay, E.; Povinelli, M. L. Near-Field, On-Chip Optical Brownian Ratchets. *Nano Lett.* **2016**, *16*, 5261−5266.
(338) Bader, J. S.; Hammond, R. W.; Henck, S. A.; Deem, M. W.; McDermott, G. A.; Bustillo, J. M.; Simpson, J. W.; Mulhern, G. T.; Rothberg, J. M. DNA Transport by a Micromachined Brownian Ratchet Device. *Proc. Natl. Acad. Sci. U. S. A.* **1999**, *96*, 13165−13169.
(339) Hänggi, P.; Marchesoni, F. Artificial Brownian Motors: Controlling Transport on the Nanoscale. *Rev. Mod. Phys.* **2009**, *81*, 387−442.
(340) Huidobro, P. A.; Ota, S.; Yang, X.; Yin, X.; Garcia-Vidal, F. J.; Zhang, X. Plasmonic Brownian Ratchet. *Phys. Rev. B* **2013**, *88*, 201401.
(341) Gorre-Talini, L.; Spatz, J. P.; Silberzan, P. Dielectrophoretic Ratchets. *Chaos An Interdiscip. J. Nonlinear Sci.* **1998**, *8*, 650−656.
(342) Huang, Y.; Wang, X. B.; Tame, J. A.; Pethig, R. Electrokinetic Behaviour of Colloidal Particles in Travelling Electric Fields: Studies Using Yeast Cells. *J. Phys. D. Appl. Phys.* **1993**, *26*, 1528−1535.
(343) Mizrahi, A.; Fainman, Y. Negative Radiation Pressure on Gain Medium Structures. *Opt. Lett.* **2010**, *35*, 3405−3407.
(344) Petrov, M. I.; Sukhov, S. V.; Bogdanov, A. A.; Shalin, A. S.; Dogariu, A. Surface Plasmon Polariton Assisted Optical Pulling Force. *Laser Photon. Rev.* **2016**, *10*, 116−122.
(345) Yin, S.; He, F.; Green, N.; Fang, X. Nanoparticle Trapping and Routing on Plasmonic Nanorails in a Microfluidic Channel. *Opt. Express* **2020**, *28*, 1357−1368.
(346) Cuche, A.; Canaguier-Durand, A.; Devaux, E.; Hutchison, J. A.; Genet, C.; Ebbesen, T. W. Sorting Nanoparticles with Intertwined Plasmonic and Thermo-Hydrodynamical Forces. *Nano Lett.* **2013**, *13*, 4230−4235.
(347) Zhou, Q.; Xia, T.; Liao, W.; Liu, Y.; Lin, D.; Yang, J.; Tao, S. Microparticle Sorting with a Virtual Optical Chip. *Rev. Sci. Instrum.* **2021**, *92*, 053201.
(348) Shanblatt, E. R.; Grier, D. G. Extended and Knotted Optical Traps in Three Dimensions. *Opt. Express* **2011**, *19*, 5833−5838.
(349) Rodrigo, J. A.; Angulo, M.; Alieva, T. Dynamic Morphing of 3D Curved Laser Traps for All-Optical Manipulation of Particles. *Opt. Express* **2018**, *26*, 18608−18620.
(350) Pohl, H. A. The Motion and Precipitation of Suspensoids in Divergent Electric Fields. *J. Appl. Phys.* **1951**, *22*, 869−871.
(351) Ashkin, A.; Dziedzic, J. M. Optical Levitation of Liquid Drops by Radiation Pressure. *Science (80-.)* **1975**, *187*, 1073−1075.

https://doi.org/10.1021/acs.chemrev.2c00576
Chem. Rev. 2023, 123, 1680−1711